ACOUSTO-OPTICAL TIME-AND-SPACE INTEGRATING PROCESSORS FOR REAL-TIME SYNTHETIC APERTURE RADAR IMAGING

Thesis by

Michael William Haney

In Partial Fulfillment of the Requirements

for the Degree of

Doctor of Philosophy

California Institute of Technology

Pasadena, California

1986

(submitted February 3, 1986)

ACKNOWLEDGMENT

The technical contributions and constant encouragement of my advisor, Professor Demetri Psaltis, are gratefully acknowledged. The eagerness and tenacity with which he tackles new problems are a constant source of inspiration for me. It has been a privilege and pleasure to be a member of his multi-talented research group.

Among my fellow students, I am especially indebted to Mr. Kelvin Wagner for many fruitful discussions and much collaboration in the laboratory. I would also like to express my thanks to Mr. Jeffrey Yu, Dr. Eung Gi Paek, Mr. John Hong, Mr. Santosh Venkatesh, Dr. Gabriel Sirat, Mr. ChihChieh Hu, Mr. Fai Mok, and Dr. Hyuk Lee, who also made contributions to my studies.

I am very grateful to General Dynamics, for the sponsorship of my studies and support of the research. Mr. T. Gordon Hame displayed great foresight in fostering collaborative research efforts with universities. Dr. Scott Higgins and Ms. Ava Schumacher administered the fellowship with much thoughtfulness and efficiency. Dr. H. Peter Schmid gave his constant support and useful advise throughout my studies. I am also thankful to NASA, who joined in the support of this work through Mr. Tom Bicknell of the Jet Propulsion Laboratory.

This thesis is dedicated to my wife, Janice, whose unwavering devotion and understanding has made the most challenging period in my life also the most rewarding.

ABSTRACT

Acousto-optical processors for Synthetic Aperture Radar (SAR) imaging are presented. The new processors produce images at real-time rates by combining the operations of data collection, storage, and processing into a compact time-and-space integrating (TSI) architecture. In the TSI approach the 2-D SAR imaging problem is decomposed into a cascade of 2 distinct operations: a 1-D spatial integration of light for range compression, and a 1-D temporal integration of light for azimuth compression. These two operations are coupled via a common path interferometric scheme that is insensitive to mechanical vibrations.

The results of an experimental characterization of the TSI approach, with simulated point scatterer radar echoes, are reported. The performance issues of interferometric bias removal, dynamic range, and resolution are addressed. The architecture is generalized to correct for range migration and the results of a range walk compensation experiment are presented. A programmable version of the TSI architecture, in which the fixed azimuth reference mask is replaced by an acousto-optic light modulator, is described. The application of the programmable architecture to both strip-map and spot-light mode SAR is analyzed and experimentally verified.

Portions of the work discussed in this thesis are also presented in the following publications:

1. D. Psaltis and M. Haney, Book Chapter: "Real-Time Synthetic Aperture Radar Processors," to be published in: Optical Signal Processing, J. Horner ed., Academic Press, 1986.

2. M. Haney and D. Psaltis, "Measurement of the Temporal Coherence Properties of Pulsed Laser Diodes," Appl. Opt., Vol. 24, No.13, July 1985.

3. M. Haney and D. Psaltis, "Acousto-Optic Techniques for Real-time SAR Processing," SPIE Proceedings, Vol. 545, April 1985.

4. M. Haney, K. Wagner, and D. Psaltis, "Programmable Real-time Acousto-Optic/CCD SAR Processor," SPIE Proceedings, Vol. 495, August 1984.

5. D. Psaltis, M. Haney, and K. Wagner, "Real-Time Synthetic Aperture Radar Processing," Proceedings of the NASA Optical Information Processing Conference, August 1983.

6. M. Haney and D. Psaltis, "Coherence Properties of Pulsed Laser Diodes," Proceedings of the 10th International Optical Computing Conference, April 1983.

7. D. Psaltis, K. Wagner, and M. Haney, "Synthetic Aperture Radar Imaging Using Acousto-Optic and Charge Coupled Devices," SPIE Proceedings, Vol. 352, August 1982.

TABLE OF CONTENTS

CHAPTER I. INTRODUCTION

1.1 Background

1.1.1 Synthetic Aperture Radar

More than thirty years have passed since the first demonstration of the imaging microwave radar technique known as Synthetic Aperture Radar (SAR)[1,2]. Since its inception, utilization of the SAR concept has continually expanded and SAR data processing techniques have, by necessity, gained in sophistication. In addition to terrestrial, lunar, and planetary mapping applications, SARs are now used for geological surveying, ocean state studies, and military surveillance, among others[3].

The importance of SAR as an imaging technique stems from the high angular resolution it achieves. SAR systems typically obtain resolution comparable to that formerly available only with shorter wavelength, real aperture sensors. In addition, since active radars carry their own source of illumination, SARs are not limited to only daylight operation, as are passive visible wavelength imaging systems; nor are they as limited in range as radiometric imaging systems, which depend on infrared radiation emitted from the target. Furthermore, unlike optical remote sensors, microwave radars have the ability to penetrate clouds, rain, snow, and foliage with relatively

low losses. The combination of these advantages and high angular resolution has made SAR a formidable imaging tool.

1.1.2 Optical Signal Processing

It is widely known that certain classes of 2-D linear operations can be implemented with optics by representing the input function as a 2-D distribution of light. The filtering is accomplished by modulating the lightwave as it propagates in the general direction of the optical axis. The general 2-D linear processing operation on the (complex) input function f(x,y) is determined by the superposition integral:

$$g(u,v) = \iint f(x,y)\ h(x,u,y,v)\ dx\ dy. \qquad (1.1)$$

In some important 2-D problems, such as SAR, the kernel, which is 4-D in general, can be represented as, or separated into two 2-D functions. In these cases optics provides the means to perform the multiplication operation in the integrand of Eq. 3.1, over all x and y simultaneously, and at speeds limited only by the propagation delay of light over short distances. The overall speed of the processor is therefore determined by the speed at which data is placed at the input plane and removed from the output plane. A feature which is just as important as this inherent parallelism is the high interconnectivity between the parallel channels due to

diffraction, refraction, and reflection of the light wave by the SLMs (e.g., holograms, lenses, mirrors) in an optical system.

The availabilty of practical, high quality coherent light sources (lasers) expanded the applicability of optical techniques to the processing of complex valued functions. Among the most useful 2-D operations possible with coherent optical processing techniques are shift-invariant operations, such as convolution and correlation, and separable kernel operations, such as the Fourier transform. Indeed, almost all practical optical signal processors, including those for SAR, consist of various combinations of imaging and the operations mentioned above.

1.1.3 Optical Processing and SAR

Optical signal processing (OSP) techniques have been applied to the collection and processing of SAR data since the introduction of the technique. Today, coherent optical signal processors routinely form images from SAR data collected by spacecraft or aircraft and recorded on photographic film. In fact, OSP technology is so well matched to the SAR data processing requirements, that optical processors still account for a major portion of the SAR images produced, despite the tremendous advances made in digital signal processing technology over the last thirty years.

The reasons OSP techniques apply so well to SAR lie in the analogy between the coherently detected radar echoes received from the object field in a SAR scenario, and the interferometrically detected Fresnel diffraction pattern of a diffusive object illuminated with a coherent light source. Synthesizing an image of a single scatterer in the target scene from SAR return signals is, with reasonable approximations, mathematically equivalent to the reconstruction of an image of a point source from an optical Fresnel hologram. The rastered (1-D) format of the radar return signals and the availability of photographic film permit this analogy to be implemented directly in the data processing. The use of film as a high-density, high-speed storage medium has provided an elegant solution to the collection and storage problems posed by the high data rates of the SAR returns. Indeed, film provides the means to fully exploit the two dimensional (2-D) parallelism and high interconnectivity afforded by optics, making SAR possibly the most successful application of OSP technology to date.

1.2 Motivation

There has been great interest lately in the development of SAR systems which have the ability to form images on board the radar platform and at real-time rates. Some existing SAR applications would benefit greatly from this capability; some proposed applications require it. These

applications include both airborne and spaceborne SARs, carried on both manned and unmanned platforms.

The benefits of real-time and on-board SAR imaging for manned missions are obvious. The astronaut/pilot would have the ability to view the focused scene on a video monitor as if it were from a conventional optical camera. The reasons for doing this might include: to help in steering the antenna to cover the desired ground swath; to preview imagery for selective direct relay to ground stations or selective recording for later detailed analysis; to use the SAR as a guidance and surveillance instrument to view ground features that are otherwise obscured by darkness, clouds, or foliage. For both manned and unmanned applications, on board imaging would reduce the complexity in the data collection, storage, and retrieval caused by the high instantaneous bandwidths of unfocused SAR data. If the data is to be telemetered directly to a ground station, the focused imagery, in the form of electronic video signals, can be transmitted without the need for reformatting to reduce bandwidth.

The use of the conventional film-based OSP approach to SAR, for on-board, real-time image generation, is precluded by the need for chemical processing of the film. Furthermore, speed and resolution requirements, as well as platform driven constraints on cost, size, weight, and power consumption, may eliminate, at least in the near term,

digital SAR signal processing techniques as well. A completely new approach to this problem is needed.

Recent advances in the technology of light sources, modulators, and detectors have made possible fast optical signal processors which do not require film, yet can handle large computational loads at real-time rates and are relatively compact and have low power requirements. In the area of light sources, laser diodes are now available which are small, efficient, and possess a large degree of coherence. They can be modulated directly at very high bandwidths. Charge coupled device (CCD) detector arrays are available to provide high-resolution outputs which can be read out at video rates. A variety of dynamic spatial light modulators, both 1-D and 2-D, with large space-bandwith products (SBWPs), now exist to allow rapid input of data. Acousto-optic devices (AODs) are an example of one of the most mature SLM technologies. The sources, modulators, and detectors provide the critical links between the optical domain and the outside world; and thus determine the effectiveness of the optical signal processing (OSP) architecture in which they are employed.

1.3 Thesis Overview

In this thesis we describe a new real-time OSP approach to SAR imaging. In the processors we've developed, the operations of data collection/storage and image synthesis

are combined, using AODs and CCDs, in a compact optical time-and-space integrating (TSI) architecture. The 2-D input and output data in the TSI approach are handled in a rastered (1-D) format that is convenient for interfacing to the radar (at the input) and display electronics (at the output). The input radar returns are applied to an acousto-optic device that, along with a pulsed laser diode (LD) light source, makes up the input electronic-to-light transducer. The range and azimuth focusing operations are coupled via a common path interferometric scheme that is insensitive to mechanical vibrations. A time integrating CCD array, which is used as the output light-to-electronic converter, is also used to store partial results during the required filtering in the azimuth dimension. Furthermore, when used in the time-delay-and-integrate (TDI) mode, the CCD array provides the shift and sum mechanism for the azimuth correlations. The focused image at the output of these AOD/CCD SAR processors is in the form of a rastered electronic signal suitable for interfacing to conventional video display equipment.

We begin, in Chapter 2, with a review of the SAR concept, signal processing requirements, and film-based optical approach. In addition to providing general background information, this discussion serves to illuminate how the features of the SAR signal processing problem are exploited in the optical TSI approach.

Chapter 3 begins with an outline of the TSI approach, followed by a functional description of the basic AOD/CCD SAR processing architecture. In describing the architecture, the range and azimuth processing techniques are first presented individually. The complete architecture, in which the range and azimuth processors are coupled to form the 2-D image, is then described. In section 3.4 the results of a characterization of the impulse response of the processor are presented. In this experiment electronic signals were generated to simulate the radar echoes that would be received from a point scatterer in the target field. Chapter 3 concludes with the results of the first focusing of an image of a real point scatterer from tape recorded aircraft SAR data.

The performance characteristics of the processor are addressed in Chapter 4. One of the most critical performance issues is the dynamic range of the output image. The effects of the interferometric detection technique on the dynamic range are examined. Included in this analysis are the various contributions of the device parameters, such as the coherence function of the pulsed laser diode and the modulation transfer function (MTF) of the CCD detector array. The effects of interference between different point scatterers on the dynamic range are also included. Another critical performance issue concerns the removal of the bias artifacts which corrupt the image in the processor. Several

bias removal techniques are discussed and the results of an experimental demonstration of one of them are presented.

In some SAR geometries the effects of range migration are not negligible and will degrade the quality of the focused image if not compensated for in the processor. In Chapter 5 we describe modifications to the basic architecture which correct for the effects of range migration. Range curvature occurs to some degree in all SAR scenarios, but is most pronounced for SARs with long azimuth windows. A technique for range curvature compensation in the processor is described. The more significant type of range migration is range walk which occurs in forward-looking and spot-light mode SARs. The results of an experiment to evaluate the range walk compensation ability of the processor are presented and compared with the results of the side-looking SAR simulation.

The parameters of the radar/target geometry change dynamically in some applications. The real-time SAR imager must have the ability to adapt to such changes in order to continuously provide a well focused image. In Chapter 6 we describe a generalization of the AOD/CCD architecture which has the flexibility to program and change its impulse response at real-time rates. In this architecture, instead of a fixed mask, a second AOD, oriented perpendicular to the first, is used to enter the reference azimuth phase history of the target scene. With this approach, the appropriate

azimuth filter can be calculated and stored electronically and entered rapidly into the processor. A multiplicative single arm interferometric approach is used to detect the azimuth reference signal and effect the correlation with the radar signals. The results of a demonstration of this architecture are presented. Two modes of operation are established. In one mode the output is in a scrolled format that is useful for strip-map SAR. In the other mode the output data is in a framed format that is more useful spot-light mode SAR.

In Chapter 7 we conclude this thesis by summarizing and highlighting the important results. A list of key performance capabilities and limitations are given. The future direction of this work, with emphasis on Inverse SAR (ISAR) applications, is briefly discussed.

CHAPTER II. REVIEW OF SYNTHETIC APERTURE RADAR

2.1 Radar/Target Geometry

The objective of a SAR system is the formation of a high-resolution two dimensional (2-D) image of the ground based on the variations in the magnitude of the backscattered radiation across the scene. Optical systems typically rely on variations in reflectivity that arise from differences in the dielectric constant at the surface being imaged. However, for the aspect angles used in a typical imaging radar system, the amount of backscatter is predominantly determined by small-scale surface roughness, although such things as slope, moisture content, dielectric constant, and shadowing also play a role. Typical radars operate at wavelengths of .3 to 30 cm. (100 to 1 GHz). Targets whose surfaces vary by the order of a wavelength or more within a resolution element will, when illuminated, scatter radiation isotropically (into a large solid angle), so that some of the incident radiation is returned to the radar. Surfaces which are smoother than a wavelength tend to act as mirrors, reflecting the radiation at an angle equal to the incident angle. In this case, very little radiation is scatterered in the direction of the receiving antenna unless it is incident perpendicular to the surface or if the target is shaped like a corner which acts as a

retro-reflector.

The basic SAR geometry is depicted in Fig. 2.1. In conventional SAR the radar is carried by a moving platform, such as an aircraft or satellite. Typically the transmitting and receiving antennae are both located on the same vehicle (although there is some work now in bi-static SAR), and very often one antenna is used for both transmitting and receiving. The synthetic aperture is formed by transmitting a periodic pulse train as the platform moves with respect to the ground being mapped. A sequence of radar echoes from the target scene is therefore received by the radar antenna at different locations along

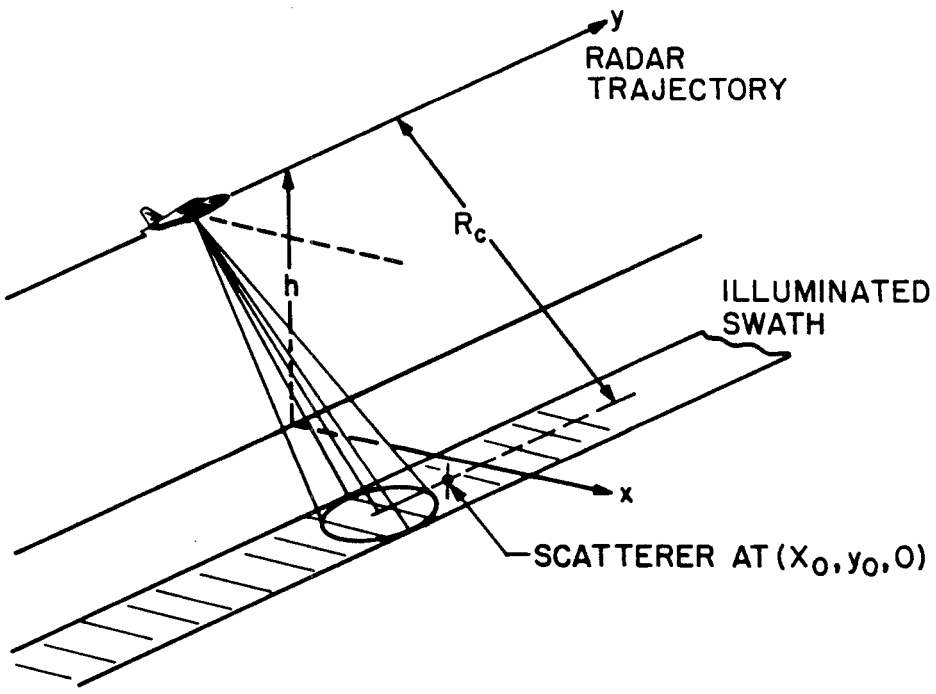

Figure 2.1. Typical SAR Geometry

the platform's trajectory. Each received signal must be stored in some way by the radar processor until all of the returns have been collected. The sequence of radar echoes are processed together to generate an image.

The angular resolution is determined by the size of the synthesized aperture and not the aperture of the real antenna itself, hence the motivation for this technique. The sampling process effected by the relative motion has led some to coin the term **Synthetic Array Radar** for this technique, which, coincidentally, has the same acronym. Whichever term is used, it is important to realize that the data is collected sequentially rather than simultaneously as in phased array radars.

The SAR processor uses the range and cross-range (azimuth) positions (relative to the location of the radar at a reference point in time) of the scattering sites as its two coordinates. The SAR technique is limited, therefore, to data gathering geometries in which a one-to-one mapping can be made between the range and azimuth histories of scatterers and the location of those scattering sites on the target.

High range resolution is achieved by coding the transmitted pulses with signals that have large bandwidths and then performing a pulse compression operation on each return with matched filter techniques. The range migration effects are determined by the geometry and can be

compensated for if neccessary. Using pulse compression, the range resolution achievable is $c/2B$[4], where c is the speed of light and B is the bandwidth of the chirp code. High resolution in the azimuth dimension is also accomplished with a matched filter approach. The azimuth data collection geometry imposes a relatively slow phase modulation on the sequence of radar returns due to the doppler shifts associated with the non-zero radial velocity component between the radar and the target. This phase history is not measurable within any single pulse, but is significant over the entire sequence. The phase history expected for each point scatterer in the target field is known a priori. The synchronously demodulated radar returns are correlated with the known phase functions to achieve azimuth pulse compression. If B_a is the doppler bandwidth of the azimuth phase history during the integration period of the SAR, then the azimuth resolution achievable is v/B_a[5], where v is the velocity of the radar. To accomplish azimuth focusing the local oscillator of the radar, which is used to generate and detect the radar signals, must have a coherence time greater than the azimuth integration time window being processed.

Depicted in Figure 1.1 is the so-called **Side-looking** SAR in which the patch of ground being imaged is located directly abeam of the moving platform. **Forward-looking** or **Squint-mode** SAR, in which the ground being imaged is ahead of (but not directly in front of) the moving radar, is also

used. In **Strip-map** SAR the antenna is fixed to the carry vehicle and the scatterers that make up the target pass through the beam as the radar moves. **Spot-light Mode** SAR is a variation of strip-map SAR in which the antenna pattern is steered (mechanically or electronically) to illuminate the same ground patch throughout the data collection period.

Unlike other high angular resolution radar techniques, which are real aperture limited and therefore use the largest antennae available, in SAR a small antenna is employed so that a large area of the ground is illuminated. The placement of the beam's footprint on the target and the PRF (pulse repetition frequency) of the radar are such that any portion of the target scene being imaged is illuminated by a long sequence of pulses. The PRF must be large enough to effectively sample the azimuth phase function of the echoes in order to avoid aliasing which would result in an ambiguity in the cross-range dimension. However, to avoid ambiguities in range, the PRF must also be small enough to insure that only the return signals from a single transmitted pulse exist at the receiver at any one time. Thus we see that to achieve the required one-to-one mapping operation in the imager there are system bounds as well as the geometrical limitations mentioned previosly.

In conventional strip-map SAR the size of the synthesized aperture is fundamentally limited by the beam's

footprint. This limit is realized if the integration time is assumed to be the time it takes the radar to travel a distance equal to the beam's footprint width on the ground. For side-looking SAR, the footprint width is given approximately by the product of the range to the scatterer, R, and the divergence angle of the antenna, λ/d, where λ is the radar wavelength and d is the width of the radar antenna. In general, the footprint width is given by:

$$W \sim R\lambda/(\sin\theta)d, \tag{2.1}$$

where θ is the grazing or squint angle (between the platform's velocity vector and antenna pointing vector). The achievable azimuth resolution (where the azimuth coordinate is taken to be perpendicular to the antenna's pointing vector) is thus given by:

$$\eta_{az} = R\lambda/2W(\sin\theta) = d/2, \tag{2.2}$$

where the factor of 2 is due to the two-way propagation path between each element of the synthesized array and the target. Thus we see that the absolute azimuth resolution limit in strip-map SAR, is equal to one half the size of the antenna and is independent of the range to the target and the velocity of the radar. It should be pointed out that, for spot-light mode SAR, where the radar beam is made to stay on the target for an arbitrary time period, the azimuth resolution limit can be smaller than that given by Eq. 2.2.

2.2 SAR Signals

The most commonly used coding signals used for SAR imaging are linear frequency modulated (LFM) signals, also known as chirps. The technology for generating high quality chirp signals, with large TBWPs, and performing pulse compression on the resultant returns is well developed. In optical SAR processing, the use of chirp coding is even more compelling due to the equivalence between them and a slice through the 2-D phase function of a Fresnel zone plate or lens in a coherent optical processor. To our knowledge, in optical SAR processing, LFM codes are used exclusively, and we assume that to be the case throughout this thesis.

We consider a radar that is carried on a platform moving with a constant velocity v, on a trajectory that is parallel to the ground at an altitude h. A swath of ground to the side of the flight path is illuminated as depicted in Fig. 1.1. As the radar moves, a sequence of N radar pulses are transmitted and received from the target area. The total azimuth integration time is NT, where 1/T is the PRF of the radar. The size of the synthetic aperture is thus vNT. For simplicity we assume that the far-field pattern of the antenna is uniform throughout the integration period for all scatterers located within the target area. The transmitted waveform is a periodic pulse train given by:

$$s(t) = \sum_{N} \text{rect}[(t-nT)/\tau] \exp(j\pi b(t-nT)^2) \exp(j\omega_0 t), \quad (2.3)$$

where τ is the pulse duration, b is the chirp rate, and $\omega_0/2\pi$ is the carrier frequency of the radar.

In the following analysis we consider the received signals for the side-looking SAR geometry in which the radar images an area directly abeam of the flight path. The modifications to this analysis for forward-looking geometries are discussed in Chapter 5. The ground reflectivity function, $\sigma(x,y)$, is considered to be a distribution of weighted delta functions. The SAR imaging operation is linear and is therefore completely described by its impulse response. We consider, therefore, the single scattering resolution element at coordinates (x_0,y_0), where the origin of the ground coordinates is at the center of the swath along a line from the radar which is perpendicular to the flight path at the start of data collection. The perpendicular distance from the center of the swath to a point on the ground directly beneath the flight path is X_C, where $X_C >> x_0$. $R_C = (h^2+X_C^2)^{1/2}$ is the minimum distance from the flight path to the center of the swath. The received signal due to the single scatterer is:

$$f(t) = \sigma_0 \, s(t - 2R(t)/c), \qquad (2.4)$$

where R(t) is the range to the point scatterer. R(t) changes with time due to the non-zero radial velocity component between the radar and target. The constant σ_0 is the complex amplitude of the signal received from the

scatterer at (x_o, y_o) and is proportional to the effective radar cross-section of the scatterer at that location. From the SAR geometry, R(t) is given by:

$$R(t) = [\ (y_o - vt)^2 + R_o^2\ ]^{1/2}, \qquad (2.5)$$

where $R_o = (h^2 + (X_C + x_o)^2)^{1/2}$ is the range to this scatterer when the vehicle crosses $vt = y_o$. The variation of the range R(t) within the pulse period is negligible. Furthermore, we assume $vt - y_o << R_o$. With these approximations the square root in Eq. 2.5 can be expanded as follows:

$$R(t) \simeq R(nT) \simeq R_o + (1 - x_o X_C / R_C^2)\ (y_o - vnT)^2 \ /\ 2R_C. \qquad (2.6)$$

To find the final expression for the radar return signals from a single scatterer we substitute Eq. 2.6 into Eq. 2.4. Lumping inconsequential constant phase terms together and assuming the delay terms due to range migration are negligible, the return signal is:

$$f(t) = \sigma_o \exp(j\omega_o t) \sum_N \mathrm{rect}[(t - 2R_C/c - X_C x_o/cR_C - nT)/\tau]$$

$$x \quad \exp(j\pi b(\ t - 2R_C/c - X_C x_o/cR_C - nT\ )^2$$

$$x \quad \exp(j(\omega_o/cR_C)\ (y_o - vnT)^2\ (1 - x_o X_C/R_C^2) + \mu_o). \qquad (2.7)$$

This signal must be processed to form an image of the point scatterer. Portions of the sequences of transmitted and received signals from a single point scatterer are shown

pictorially in Fig. 2.2. The radar return signal in an actual SAR scenario, with N_0 resolution elements within the scene, consists of the coherent sum of N_0 signals like Eq. 2.7.

2.3 SAR Processing Requirements

Eq. 2.7 represents the unfocused image of a 2-D scattering element. For this reason it is useful to express the rastered 1-D return signal of Eq. 2.7 in a 2-D format. This amounts to stacking the N individual returns one after the other, resulting in a 2-D function that is sampled along one of its coordinates. For simplicity we assume that the signal is at baseband, i.e., Eq. 2.7 is first mixed with $\exp(-j\omega_0 t)$. We choose the range, x, and the cross-range, y, ground coordinates as our 2 variables. To do this we define: $x = (t - nT - 2R_C/c)c$ and $x_0' = x_0 X_C/R_C$. With these variable substitutions Eq. 2.7 becomes:

$$f(x,nvT) = \sigma_0 \ \mathrm{rect}[(x-x_0')/X'] \ \mathrm{rect}[(nvT-y_0-Y'/2)/Y'] \times \exp(jb_1(x-x_0')^2) \exp(jb_2(nvT-y_0)^2(1-\alpha x_0)+\mu_0), \quad (2.8)$$

where: $X' = c\tau$, $Y' = vNT$, $b_1 = \pi b(X_C/cR_C)^2$, $b_2 = \omega_0/cR_C$, and $\alpha = X_C/R_C^2$. The function f(x,nvT) is a sampled version of the 2-D function f(x,y), with the sampling along the y (azimuth) coordinate. The function f(x,y) is approximately bandlimited in y, with a bandwidth of $b_2(1-\alpha x_0)Y'/\pi$. We assume the spatial sampling frequency, 1/vT, to be greater

than twice the bandwidth. With this assumption, the continuous (unsampled) representation of the radar return is valid if the processor is assumed to low-pass filter the actual sampled returns in the y dimension.

Eq. 2.8 is a windowed, asymmetrical quadratic phase function whose center is located at coordinates (x_0,y_0). The chirp rate in the x direction is proportional to the temporal chirp rate of the transmitted pulses, as expected. In the azimuth dimension, the chirp rate is determined by the radar carrier frequency and the range coordinate of the target.

A matched filter operation must be performed to focus the return signal into a high resolution image of the scatterer. For each point scatterer, the required operation is a correlation with a reference function r(x,y), equal to f(x,y), but shifted to the origin. The image of the point scatterer is thus given by:

$$g(x,y) = \iint f(u,v)r^*(u+x,y+v)\,du\,dv, \qquad (2.9)$$

where:

$$r(x,y) = \text{rect}[x/X'] \; \text{rect}[(y-(Y'/2))/Y'] \times \exp(jb_1x^2) \exp(jb_2(y^2(1-\alpha x_0)+\mu_0). \qquad (2.10)$$

The processing steps needed to focus the image of a point scatterer in a SAR imager are shown pictorially in Fig. 2.3. The computational load on the SAR imager is

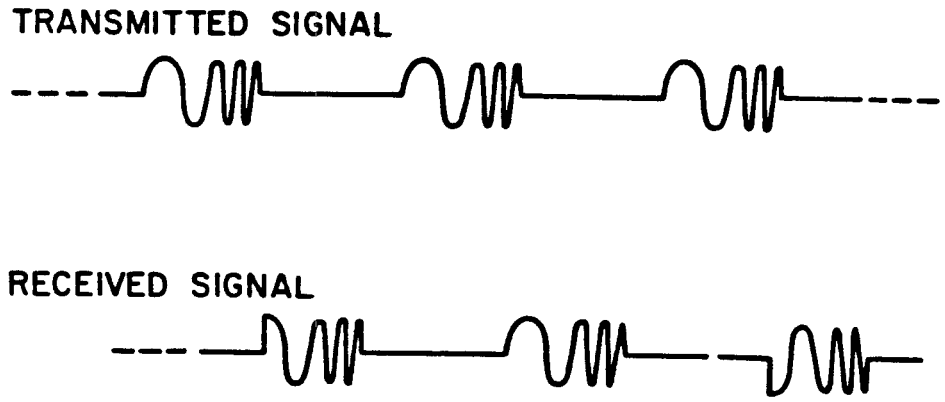

Figure 2.2 Pictoral Representation of SAR Signals for a Single Point Scatterer.

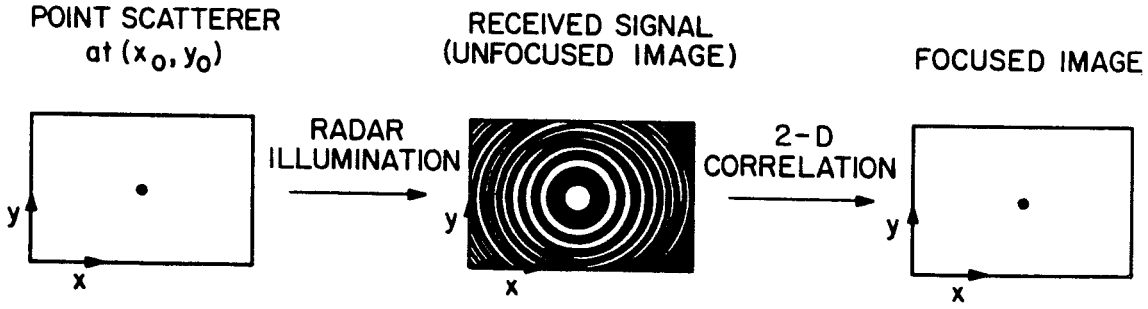

Figure 2.3 SAR Processing

evidenced by Eq. 2.9. In practice the focusing of the image of a single point scatterer may require approximately 10^6 complex multiply/sum operations. To generate a complete 1000 x 1000 pixel image requires, therefore, the order of 10^{12} complex multiply/sum operations. Although digital SAR processors can reduce this number significantly by applying FFT algorithms, the computational load is normally too large for real-time applications in which the size and power constraints are severe.

The general kernel, h, for the side-looking SAR imaging operation is given by r(x+u,y+v), with x_0=u. Thus we have:

$$h(x,u,y,v) = \text{rect}[(x-u)/X'] \; \text{rect}[(y-v-Y'/2)/Y'] \times \exp(jb_1(x+y)^2) \exp(jb_2(y+v)^2(1-\alpha u)+\mu_0). \quad (2.11)$$

The linear operation is shift-variant and not separable due to the range/azimuth coupling effect in the SAR data collection geometry. Despite this fact, this kernel has features which allow OSP techniques to be applied. For example, the required integration in the range dimension is shift-invariant for all point scatterers. Furthermore, for all scatterers located within any single range bin, u', the azimuth filtering operation is shift-invariant also, and the kernel is separable, i.e., it can be expressed in the following way:

$$h(x,u',y,v) = h_1(x+u')\, h_2(y'+v'), \quad (2.12)$$

where $y' = y(1+\alpha u')$ and $v' = v(1+\alpha u')$. The implementation of the SAR imaging operator thus requires a shift-invariant operation (LFM correlation) in the range dimension, while filtering in the azimuth dimension consists of a bank of 1-D LFM correlators, whose reference chirp rates vary approximately linearly with the range coordinate.

2.4 Review of Film-based Optical SAR Processing

In the conventional, non-real-time, optical approach a two step process is employed to produce SAR images. First an optical recorder is used to collect and store the radar returns in the form of a hologram on photographic film. The data on the hologram consist of a coherent sum of weighted Fresnel zone plates, each zone plate representing the unfocused image of an individual scatterer in the target scene. After chemical development, the hologram is used as the input SLM of a coherent optical processor which focuses the collection of zone plates into a high resolution image.

The optical recording technique employed in SAR data collection is depicted schematically in Figure 2.4. The return signal for each transmitted pulse is first coherently detected by electronic means as it is received. The temporal waveform is used to modulate the intensity of a cathode ray tube (CRT). The face of the CRT is imaged onto the film to record one azimuth slice of the unfocused image. The film is moved up in synchronism with the PRF of the

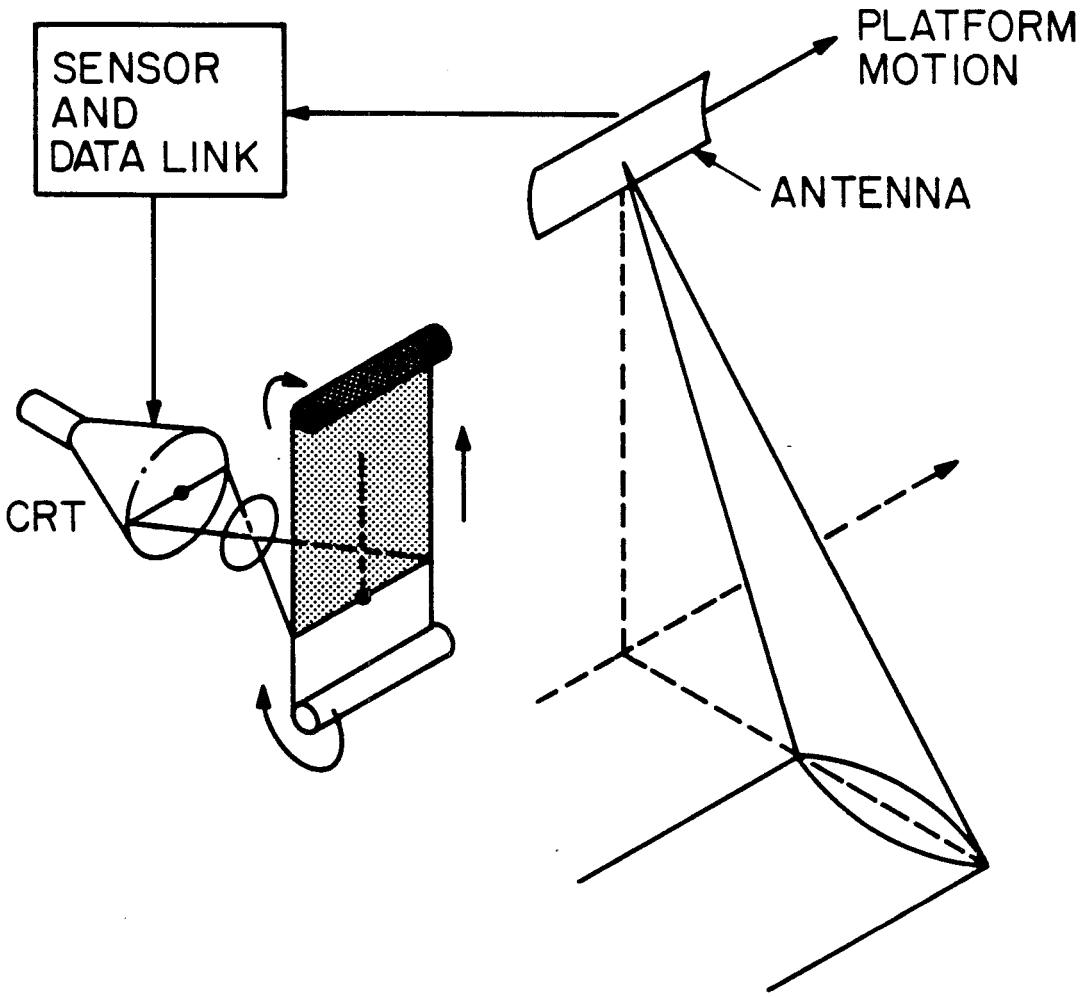

Figure 2.4. SAR Optical Recording (courtesy JPL).

radar such that each succesive return (azimuth slice) is recorded just below the previous one on the film. For a single point scatterer the resultant exposure pattern is an asymmetrical Fresnel zone plate whose range and azimuth focal lengths are determined by the characteristics of the radar, SAR geometry, and optical recorder, as shown in Fig. 2.5. The effects of range curvature on the recorded phase history are shown (exaggerated for the purpose of illustration) in Figure 2.6.

Various designs for the film-based 2-D coherent optical processor needed to focus the holographically stored radar returns have been employed over the years of SAR usage. Despite their variation, certain features are common to all of these architectures. They are all 2-D space integrating correlators which focus the radar signals by auto-correlating chirp signals with LFM kernels that result from free space propagation in the Fresnel diffraction regime. They all possess an input plane, where the hologram is placed and illuminated with coherent light, and they all have an output plane, at which the focused image is read out to a 2-D detector such as photographic film, the human eye, or a video camera. In all of these approaches the input and output planes are connected with an anamorphic system of optical elements which perform the shift-variant operation determined by Eq. 2.11, as well as compensate for range migration effects, if necessary.

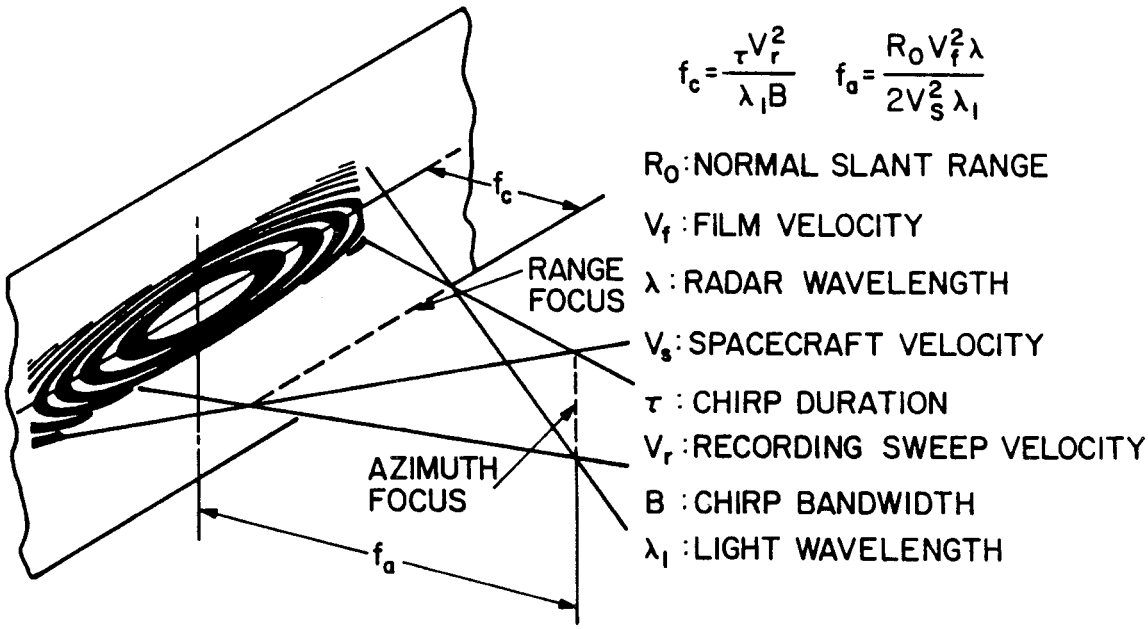

Figure 2.5. Focal Properties of Recorded Point Scatterer Phase History (courtesy JPL).

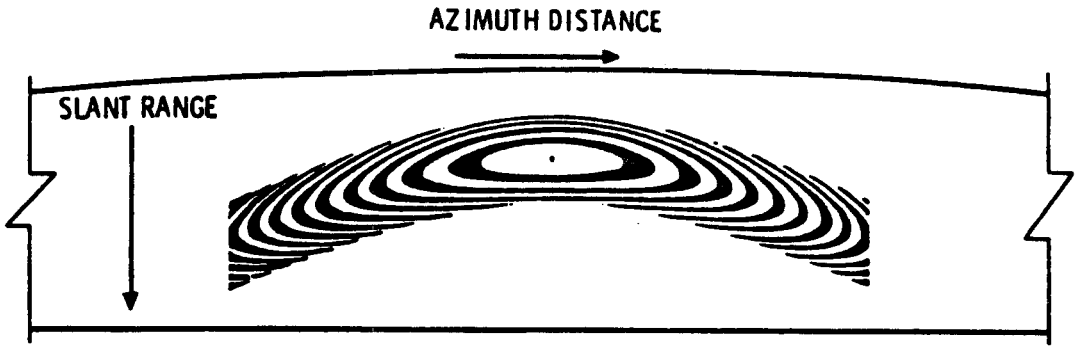

Figure 2.6. Phase History of Point Scatterer showing Range Migration Effects (courtesy JPL).

The focal length of a Fresnel zone plate is inversely proportional to the chirp rate. Since the chirp rate of the SAR zone plate in the azimuth dimension varies approximately linearly with the range coordinate, the azimuth focal length of the zone plate also varies approximately linearly with the range coordinate (because we assume that $\alpha u << 1$ in Eq. 2.11). The straightforward approach, therefore, to achieve coplanar focusing of Fresnel zone plates associated with point scatterers at different ranges, is simply to tilt the input and/or output planes of the correlator with respect to the optical axis by an appropriate angle with respect to the range axis of the hologram and/or output detector. A simplified diagram of a correlator which uses this technique is shown and described in Figure 2.7.

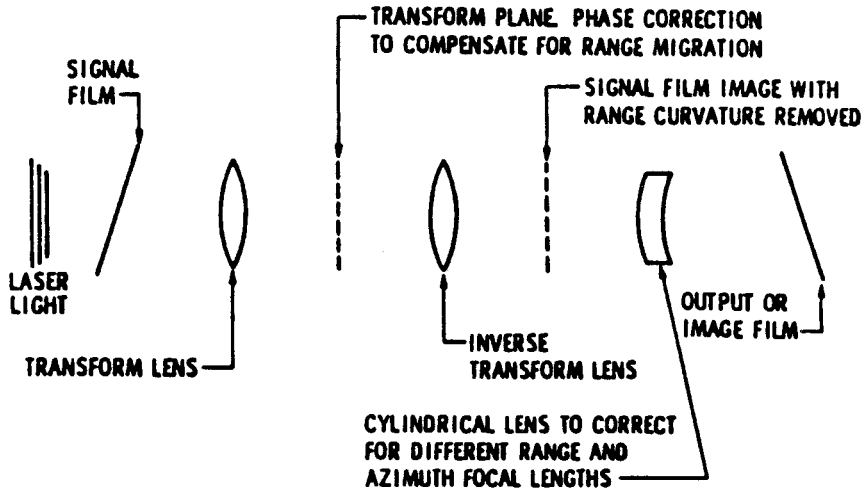

Figure 2.7. Coherent Optical SAR Processor.

CHAPTER III. REAL-TIME OPTICAL SAR PROCESSOR

3.1 Optical Time-and-Space Integrating Processing

The straight-forward approach to real-time 2-D optical processing is to replace the static 2-D SLMs in existing architectures with dynamic 2-D SLMs whose optical transfer characteristics can be updated as needed. In the SAR problem this would involve eliminating the film recorder and using a 2-D real-time holographic SLM at the input plane of the SAR space-integrating correlator. However, the practical realization of such real-time 2-D processors, which would take full advantage of the processing power of optics, has been limited by the lack of availability of high quality dynamic 2-D SLMs.

On the other hand, the relatively higher maturity in the technolgy of 1-D SLMs, specifically acousto-optic (AO) Bragg cells, has led to the emergence of a new generation of architectures which employ 1-D SLMs to implement 2-D linear operations in three spatial coordinates. Although less straightforward, the implementation of 2-D processors with 1-D SLMs usually offers more flexibility in their design[6]. Furthermore, in most problems, the 2-D input and filter functions are available in the form of rastered 1-D electronic signals which, in many cases, can be applied directly to the 1-D SLM. Also, in the case of Bragg cells, the 1-D SLMs act as tapped delay lines and can therefore be

used as part of the filter implementation as well as the input electronic-to-light transducer. Lastly, the applicability of 1-D SLMs to the 2-D processing problems is enhanced by the fact that the output 2-D detector array is typically read-out as a serial electronic signal. The overall computational speed of the optical processor is ultimately limited by this output bottleneck, rather than the intrinsic processing speed of the optics. Therefore, with proper design, the input data rates afforded by 1-D SLMs are high enough to not limit the overall speed of the processor.

In our processors the 2-D SAR imaging operation is implemented in a time-and-space integrating (TSI) architecture using a 1-D AO cell as the input SLM and a 2-D CCD detector array as the output transducer. The TSI approach, which was first proposed for spectrum analysis of 1-D signals[7,8], has now found application in several 2-D problems[9,10,11], and is especially well suited to shift-invariant and separable kernel operations. The general TSI approach employs a relatively fast spatial integration of light (in which many optical rays are summed simultaneously on a detector element) along one of the coordinate axes, and a slower temporal integration of light (in which optical beams from different instants of time are summed on a detector element) along the other dimension. TSI processing is well suited to problems involving rastered electronic

input data such as that of SAR or other video imagery. This is due to the large difference in data rates for input information between the two coordinate axes with rastered inputs. Typical instantaneous bandwidths for SAR are 10^7 - 10^8 Hz along the fast (range) dimension, with TBWPs of the order of 1000, while along the slower (azimuth) coordinate input data rates are of the order of the PRF of the radar, typically 10^3 Hz, with TBWPs of the order of 1000. The bandwidths and TBWPs (or SBWPs) of state-of-the-art AO devices are well matched to the implementation of space integrating techniques to handle the high instantaneous data rates; while the operating bandwidths of time-integrating detector arrays are best suited to the lower azimuth bandwidths. The two implementations in the TSI approach are complementary in that the results of the spatial integration are processed and stored on the time-integrating detector as partial results of the temporal integration. The use of the time-integrating detector in this manner eliminates the need for a high-speed digital array processor to manipulate the intermediate results.

The basic TSI optical processor is shown pictorially in Figure 3.1. The input electronic-to-light transducer consists of an AO cell and pulsed laser diode light source. Light from the source is diffracted by the AO cell and then filtered with various static and/or dynamic 1-D and/or 2-D SLMs arranged to suit the particular filter function. The

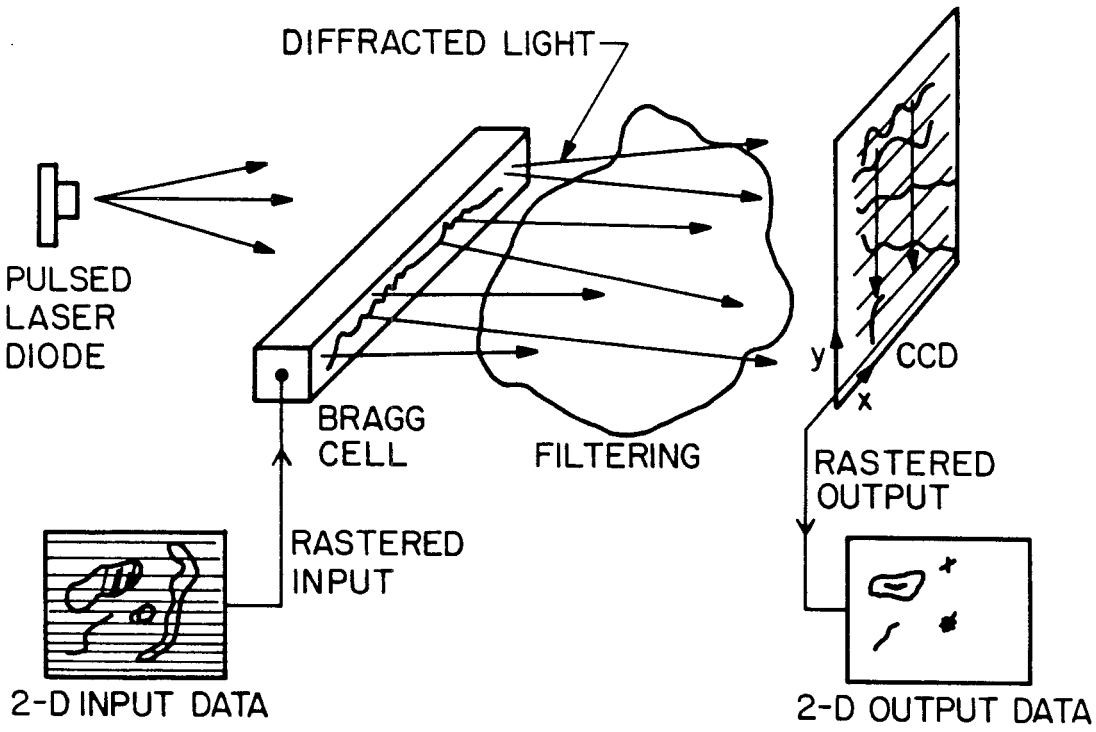

Figure 3.1. Optical Time-and-Space Integrating Processor. At the output plane light has been temporally integrated along the y direction and spatially integrated along the x direction.

output light-to-electronic transducer is a 2-D time-integrating CCD detector array. Before describing the operation of the TSI system we shall first highlight those characteristics of the active components important to the understanding of the operation of SAR architecture.

An AO Bragg cell consists of an AO crystal on which is bonded a piezoelectric transducer as shown in Figure 3.2.

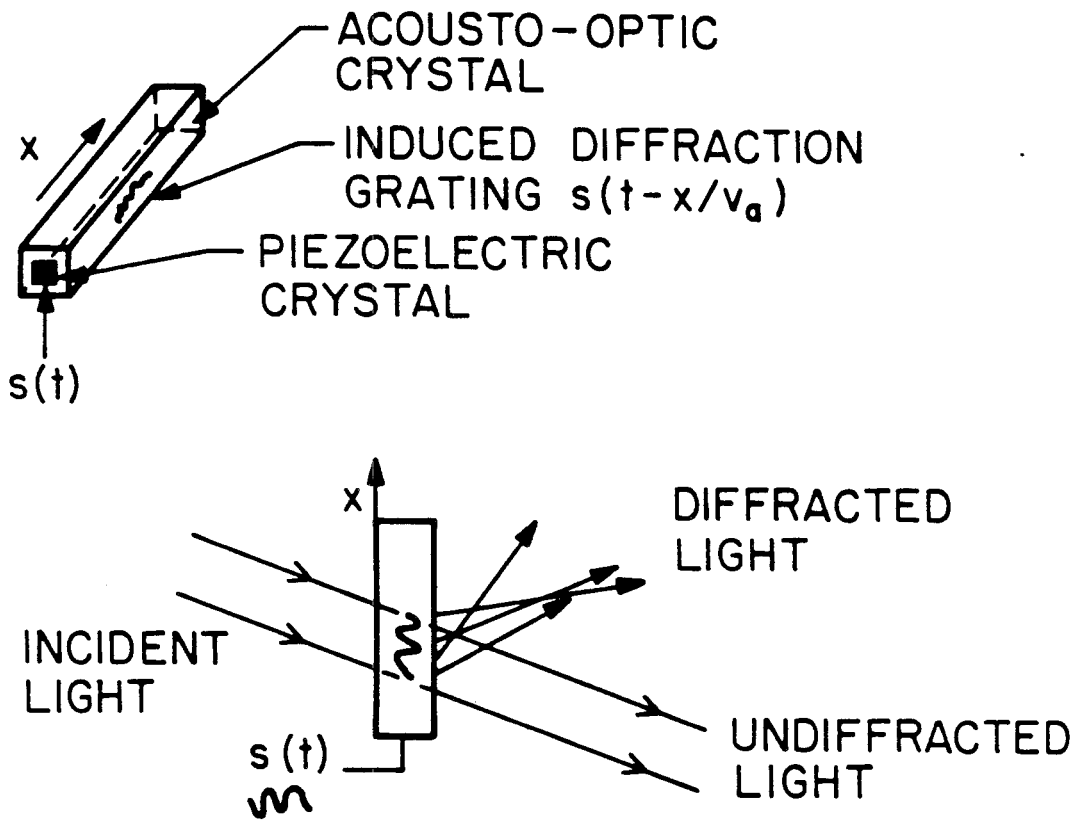

Figure 3.2. Acousto-Optic Bragg Cell.

When an electronic signal is applied to the piezoelectric transducer a bulk acoustic wave is induced in the AO crystal which propagates along the x direction at the velocity of sound. When illuminated with a collimated beam of light, a portion of the incident beam is diffracted due to the acousto-optic interaction[12]. If the angle of incidence of the light is near the Bragg angle then most of the diffracted light will be concentrated into one of the

first diffracted orders[13]. If the electronic signal applied to the cell is g(t), and the diffraction efficiency is assumed to be << 1, then the complex amplitude modulation of the diffracted light is approximately $\text{rect}(x/A)g(t-x/v_a)$[14] where A is the aperture window of the cell and v_a is the velocity of sound in the crystal. The SBWP of an AO cell is $(A/v_a)\beta$, where β is the temporal bandwidth. The SBWP of modern commercially available AO cells can exceed 2000.

The laser diode was selected as the light source in the TSI SAR processor because of its small size, high efficiency, and the fact that it can be modulated directly with high bandwidths. Furthermore, single longitudinal mode laser diodes possess the high degree of coherence needed for effective interferometric detection. A typical heterostructure GaAlAs laser diode is shown schematically, along with its key performance characteristics, in Fig. 3.3. The device is a forward biased hetero-junction formed by 3 layers of variably doped material with different ratios of Gallium to Aluminum. The ends of the device are cleaved or etched into mirrors and the central layer forms a Fabry-Perot cavity. Light is confined laterally in the cavity due to mismatch in indices of refraction between the layers. Forward current produces electron-hole pairs which emit light upon recombination in the depletion (middle) layer. The characteristics of the cavity are such that, above the threshold current, enough electron-hole pairs are generated

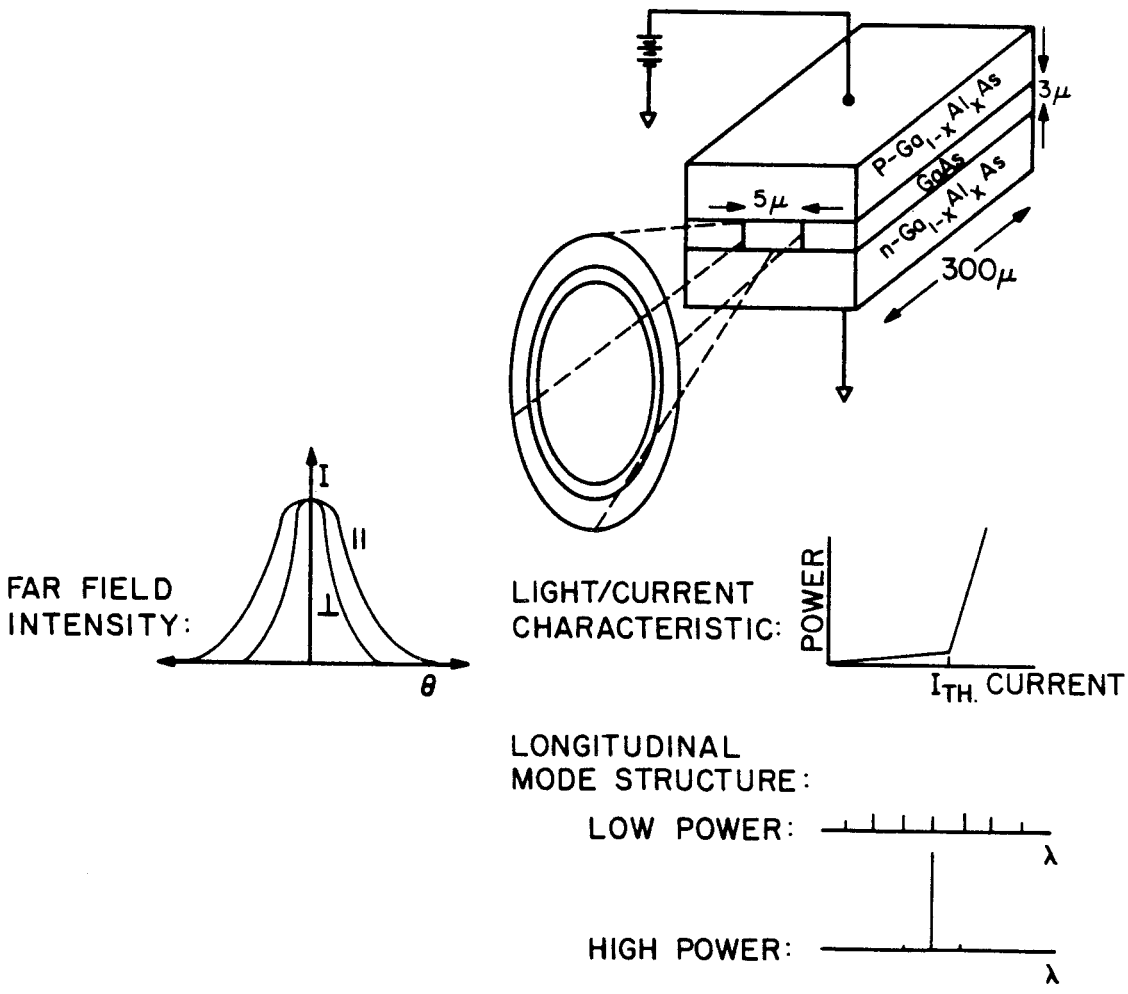

Figure 3.3. Heterostructure Single Mode Laser Diode.

to support laser oscillation. In high-quality laser diodes the intensity of the laser light emitted from the facet increases with a high degree of linearity with current over a wide range above the threshold. Typically, single cavity laser diodes produce laser radiation at several adjacent longitudinal modes. Some high-quality devices are essentially single mode at higher output levels, and as a result have large intrinsic coherence lengths. In many laser diodes the geometry of the cavity is such that only the fundamental transverse mode is supported. This results in an asymmetrical gaussian far field pattern as shown in Fig. 3.3.

The CCD detector consists of a matrix of photosensitive sites (pixels) which is used to convert a 2-D irradiance function into an electronic video signal. Each pixel site is a MOS capacitor (typically built on silicon) capable of storing photogenerated charge in its depletion region. Photons with energy greater than the bandgap (~1.1eV in Si) and incident on a pixel will generate electron-hole pairs. A system of electrodes is used to create potential wells at each pixel to store one or the other photogenerated carrier types (usually the minority carriers) for a specified integration time. The pixels are then interrogated in a raster format by applying synchronous voltage signals to the electrodes in a manner which transfers the photogenerated charge from one pixel site to another along one dimension of

the device. This process is repeated periodically and results in the propagation of charge toward a final CCD stage which moves the charge to the output pin of the device where it is sensed and can be interfaced to display electronics.

CCDs have two basic modes of operation. In the time-integrating mode (TI), after the array has been exposed, the entire charge pattern is read-out before the next exposure. This mode is suitable for framed output applications. In the time-delay-and-integrate (TDI) or shift-and-add mode the charge pattern is shifted by only one pixel between exposures so that the charge reaching the output stage represents a summation of light over many exposures. In this mode the CCD can be used as an optically addressed shift-register in the filter implementation. The output is in a scrolled format in the TDI mode.

The operation of the basic TSI architecture is as follows. The 2-D input data, f(x,y) is raster scanned at a velocity v_a (which we assume, for simplicity, to be equal to the acoustic velocity in the AO cell). The resultant signal is heterodyned to the center frequency, ω_0', of the AO cell and applied to its input. The temporal signal at the input transducer is thus given by:

$$s(t) \sim \left[\sum_N f(v_a t - n v_a T, n\delta y) \right] \exp(j\omega_0'(t-nT)), \quad (3.1)$$

where 1/T is the line scan frequency and δy is the distance

between samples in the y dimension. We assume that the scan frequency and the AO center frequency are synchronized, i.e., $T = 2\pi Q/\omega_o'$, where Q is an integer. Therefore $\exp(j\omega_o nT) = 1$, and for the nth line the resulting diffraction pattern is given by :

$$s_n(t-x/v_a) \sim [f(v_a t - nv_a T - x, n\delta y)] \exp(j(\omega_o'/v_a)(v_a t - x)). \quad (3.2)$$

The laser diode in the TSI architecture acts as a sampling device. After the moving diffraction grating has propagated an appropriate distance in the crystal, the laser diode is pulsed with a period that is less than 1/2 the inverse of the temporal bandwidth of the applied electronic signal. This effectively freezes the moving grating and the resultant filtering of the diffracted light wave in the x dimension can be thought of as a spatial integration on a stationary diffraction pattern. The aperture of the AOD, A', is assumed to be large enough to contain one entire line of data. The laser diode is pulsed in synchronism with the line rate but is delayed from the start of each line by an amount equal to the period of one line. This gives the data time to fill the AO aperture before it is illuminated. In Eq. 3.2 we make the variable substitution: $v_a t - nv_a T - x = A' - x'$. Defining the input transducer of the AO cell to be $x' = 0$, the resulting stationary diffraction pattern, for the nth line, is:

$$g(x',n) = f(A'-x',\ n\delta y)\exp(j\omega_0'(A'-x')/v_a)$$
$$= f(x,n\delta y)\exp(j\omega_0' x/v_a), \qquad (3.3)$$

where we have defined the new variable x=A'-x'.

The optical transducers between the AO cell and the CCD perform a 1-D spatial integration on the input **diffracted** field with the resulting complex amplitude modulation of the optical field at the output plane given by:

$$c(\eta,\xi,n\delta y) = \int g(x,n\delta y)\ h(x,\eta,n\delta y,\xi)\ dx. \qquad (3.4)$$

The total optical field strength present at the output plane after N lines of data have been entered is therefore:

$$C(\eta,\xi) = \sum_N c(\eta,\xi,n\delta y)$$
$$= \sum_N \int g(x,n\delta y)\ h(x,\eta,n\delta y,\xi)\ dx. \qquad (3.5)$$

Eq. 3.5 is essentially identical to Eq. 1.1 with one of the continuous variables replaced by a discrete one.

The optical implementation of Eq. 3.5 in a TSI system is in general difficult for two reasons. First, optical detectors can sense only average intensity. Therefore, a direct implementation of Eq. 3.5 would result in the following charge pattern on the CCD:

$$Q(\eta,\xi) = \sum \left|\int g(x,n\delta y)\ h(x,\eta,n\delta y,\xi)\ dx\right|^2, \qquad (3.6)$$

which is not a linear system implementation. The non-linearity associated with intensity detection can be

overcome through the use of interferometric techniques, as will be shown for the SAR processor in Section 3.3.1. The second major difficulty in the implementation of Eq. 3.5 lies with the optical representation of the kernel, h. In typical optical systems the kernel is represented in 2 spatial coordinates and changed in time, if neccesary, to achieve a third dimension. The kernel function is in general a function of 4 variables which can not be implemented optically. However, optical processors can be configured for certain important forms of the kernel function, for example, shift-invariant and separable linear operations. Though not shift-invariant or separable, the SAR operation, as determined by the kernel in Eq. 2.11, has features, as described in Section 2.4, which permit an optical TSI implementation.

In the film-based optical processing approach the correlator generates the image by performing a spatial integration of light in both the range and azimuth dimensions simultaneously. However, since the data is not received simultaneously, the required integrations in the two dimensions do not necessarily have to be performed at the same time. This is shown by rewriting Eq. 2.9 in the following manner:

$$g(x,y) = \sum_{N}\Big[\int f(u,nvT)\, \exp(-j(b_1(u+x)^2)du \Big]$$

$$x \qquad \exp(-j(b_2(nvT+y)^2(1+\alpha x_0))+\mu_0), \qquad (3.7)$$

where we have reverted to the actual sampled representation of the input 2-D data. Eq. 3.7 reveals that the two integrations can be performed as a cascade of two one dimensional integrations (one discrete, one continuous). Furthermore, since the SAR operation is shift-invariant along the range coordinate and separable for all targets within any range bin, we can implement the filter with the TSI approach. These features permit the SAR processor to use a 1-D SLM as an input device and process the reflection of each radar pulse one at a time. Real-time operation can be achieved by performing the required integration in the range dimension on each of the radar returns as they are received, and another integration in the azimuth dimension as the range focused radar returns accumulate in the processor. The range and azimuth implementations are discussed separately in the following sections, followed by a presentation of the complete processor in which the range and azimuth operations are combined.

3.2 Range Compression

3.2.1 Space-integrating Processor

The spatial integration technique used to perform the range compression in the SAR processor is shown schematically in Fig. 3.4. The rastered return signal (Eq. 2.7) is heterodyned to the center frequency of an AO cell and applied to its input. The laser diode is pulsed in

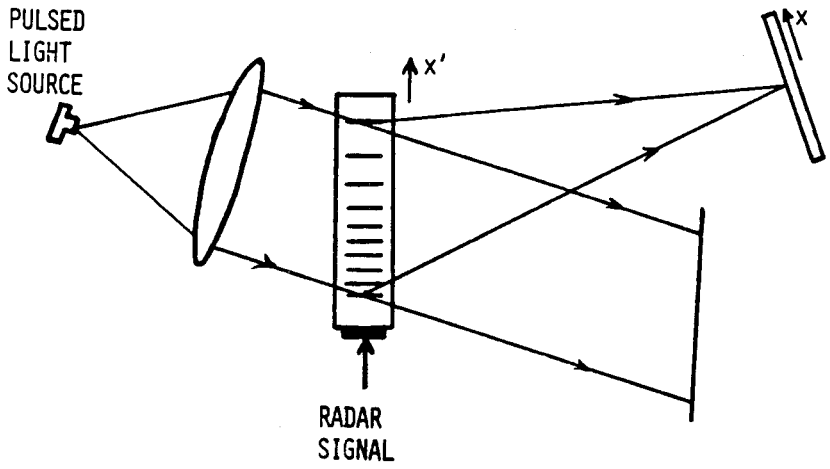

Figure 3.4. Optical Space Integrating Technique used for Range Compression

synchronism with the radar at a rate equal to the PRF. The light pulse is timed to coincide with the instant that the moving diffraction grating is in the AO cell. As described earlier, the pulse width of the laser illumination is short enough to effectively snap-shot the moving diffraction grating induced by the radar signals in the AO cell. We can therefore consider the diffraction pattern to be stationary.

We consider one azimuth slice of the return signal from a single point scatterer (Eq. 2.8) to be contained in the AO cell. To transform the radar signal from the ground range (measured from the center of the swath) coordinate (x) into the spatial coordinate of the AO cell we define $\bar{x}' = x(v_a/c)$.

With this variable substitution, the resulting diffraction grating in the AO cell due to a point scatterer located at ground coordinates (x_o,y_o), for the nth radar return of the integration period (by our previous definitions, the radar is located at position y = vnT), is given by:

$$f'(\bar{x}',vnT) = \sigma_o \, \mathrm{rect}[(\bar{x}'-\bar{x}_o')/\bar{X}'] \quad \exp(j(\omega_o'/v_a)\bar{x}')$$
$$\times \quad \exp(jb_1'(\bar{x}'-\bar{x}_o')^2 \exp((jb_2(vnT-y_o)^2(1-\alpha'\bar{x}_o))+\mu_o), \qquad (3.8)$$

where: $\bar{X}' = X'(v_a/c)$, $b_1' = b_1(c/v_a)^2$, and $\alpha' = \alpha(c/v_a)$. The signal in Eq. 3.8 forms a 1-D Fresnel zone plate or holographic lens on a carrier as depicted in Fig. 3.4. The light diffracted by this pattern comes to a focus at a distance from the AO cell given by:

$$f_{ch} = v_a^2/\lambda b \qquad (3.9)$$

If the AO cell were illuminated at the lower Bragg angle, the diffracted beam would be a diverging beam, instead of converging as shown in Fig. 3.4. In this case a lens could be used to bring the virtual focal plane into real focus on the detector. In either case, it is this self focusing action of the radar return that accomplishes the pulse compression in the range dimension. The optical field at the focal plane of the induced Fresnel zone plate is given by the following spatial integration:

$$f_i'(x',vnT) = \int f'(u,vnT)\ \exp[-j(\pi/\lambda f_{ch})(u+x')^2]\ du$$
$$\simeq \sigma_o\ \mathrm{sinc}[(x'-x_o')\bar{X}'b_i']\ \exp((jb_2(vnT-y_o)^2(1-a'x_o'))+\mu_o). \quad (3.10)$$

Thus we see that the amplitude of the range focused field is a sinc function centered at a position along the x' coordinate of the detector plane which is proportional to the range difference coordinate of the actual point scatterer. The width of the sinc function is approximately $1/\bar{X}'b_i'$. The pulse compression ratio is therefore $(\bar{X}')^2 b_i'$, which is equal to the TBWP of the transmitted chirp code as desired.

3.3.2 Range Focused Data

The initial validation of the range compression technique was carried out with the apparatus shown in Fig. 3.5. The pulsed laser diode used in the experiment operated at a wavelength of .83 microns, .5 watts peak power, and pulse width of 50 nanoseconds. A spherical lens was used to collimate the light from the laser diode. A quartz AO cell was used which had 40 MHz bandwidth and and 10 μsec aperture. Cylindrical optics were used to match the shape of the light beam to the aperture of the AO cell. The signal applied to the cell is shown in Fig. 3.6a. The pair of consecutive LFM signals was generated by a surface acoustic wave (SAW) device at a 10KHz PRF. The duration of each LFM was 5.8 μsec and the bandwidth 23 MHZ with a center

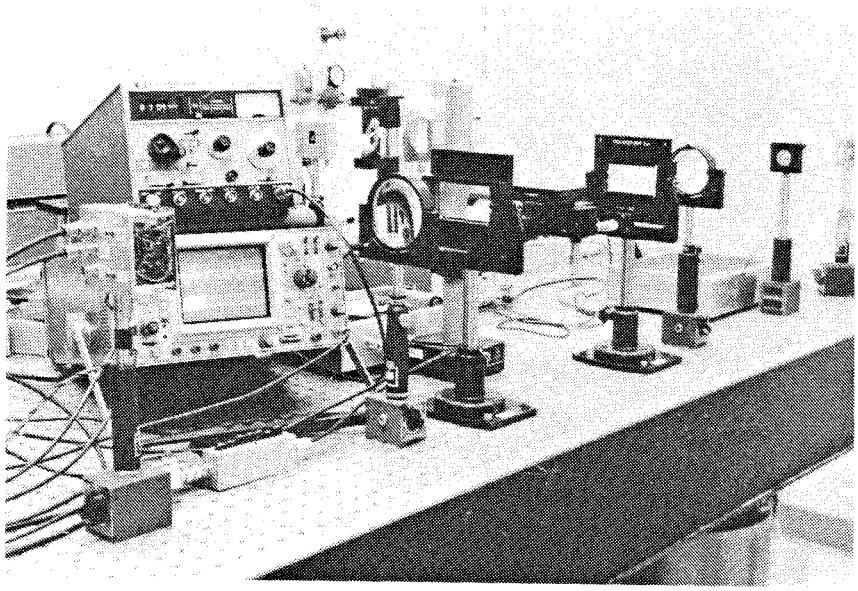

Figure 3.5. Apparatus for validation of range compression technique.

frequency of 60 MHz. The same SAW device was used to generate the simulated radar returns for all the experiments reported in this thesis. The chirp rate of the LFM from this device is 23MHz/5.8μsec or approximately 4 x 10^{12} Hz/sec. This signal was heterodyned down to baseband for display purposes in Fig. 3.6a. The laser diode was pulsed at the same PRF, delayed by approximately 15 μsec, to allow the signal to propagate through through the SAW and the AO cell. The focal length of the induced Fresnel zone plates in the AO cell were of the order of 3 meters. An additional lens was therefore added to the system to bring the diffracted light into focus within a more reasonable distance. A 381 mm focal length spherical lens was used for this purpose. The diffracted beams were converging in this

experiment and the focal plane was found approximately 36 cm after the spherical lens. The collimated undiffracted light was spatially separated from the signal at this point and the signal was detected by a linear detector array. Thirty light pulses were integrated on the array before it was read out. The signal from the detector is displayed in Figure 6b and it shows the two LFM signals compressed, corresponding to bringing the SAR image (of two spatially separated scattering sites) into focus in range. The CCD detects intensity and thus each range focused signal corresponds to the square of the amplitude of the signal represented by Eq. 3.10. The resulting photogenerated charge on the CCD in Fig. 3.6b is thus given by:

$$Q(x') \sim \sigma_1^2 \, \mathrm{sinc}^2[(x'-x_1')\bar{X}'b_i'] + \sigma_2^2 \, \mathrm{sinc}^2[(x'-x_2')\bar{X}'b_i']. \tag{3.11}$$

Azimuth Pulse Compression

3.3.1 Interferometric Approach

The information needed to focus the SAR image in azimuth is encoded in the phase of the range compressed optical signals as shown in Eq. 3.10. A coherent process must be employed to detect this phase history. This can be accomplished only by using a coherent light source and by introducing a reference beam, derived from that source, which interferes with the range focused beam at the detector to yield a modulation of the intensity proportional to the

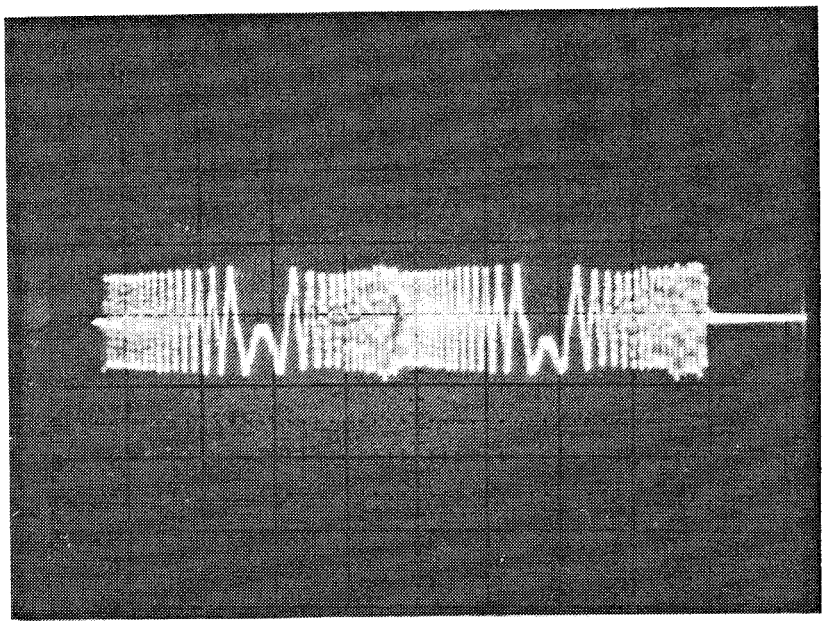

(a) Uncompressed range chirp signals

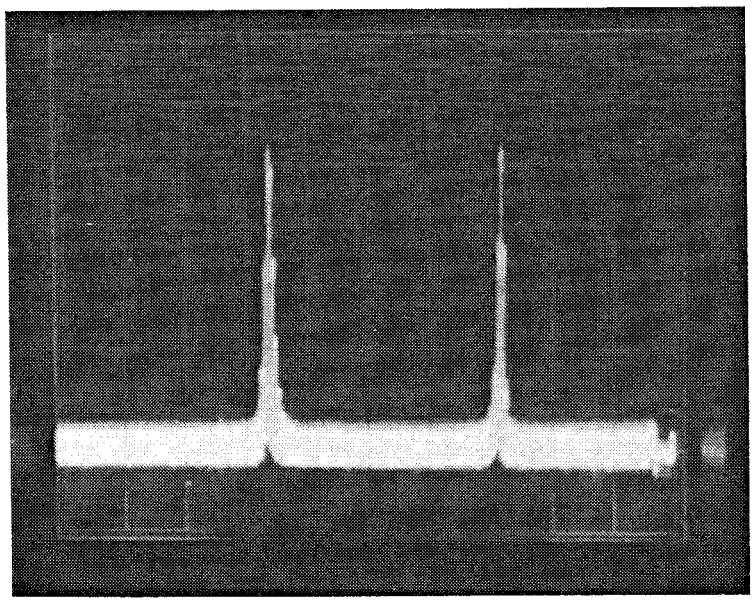

(b) Output of range processor showing results of optical pulse compression

Figure 3.6. Range Compression Test Results.

cosine of the phase difference between the two beams. Interferometric detection will, in general, decrease the dynamic range due to the residual bias terms that result. Furthermore, it imposes stricter requirements on the mechanical stability of the optical system and the coherence of the source. Additionally, since the range focused optical field is doppler shifted by the center frequency of the AO cell, the reference beam must also be shifted by the center frequency to achieve stationary fringes at the output. In this section we describe an interferometric detection scheme that minimizes the effects of these problems.

The interferometric detection approach is shown schematically in Fig. 3.7. A sinusoidal reference signal,

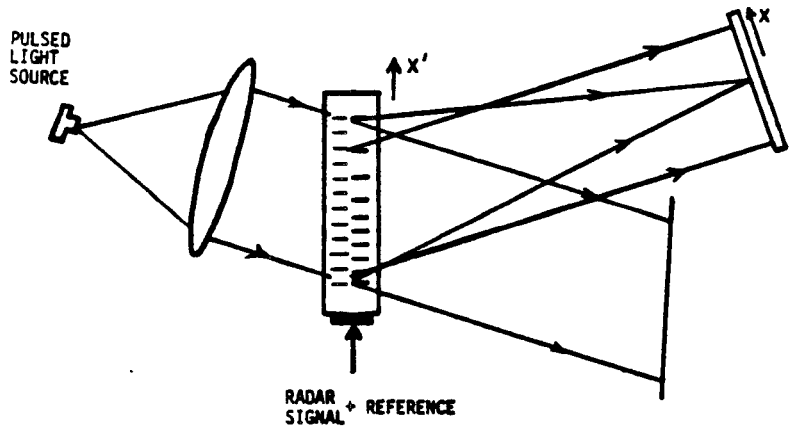

Figure 3.7. Interferometric Detection Scheme.

at the center frequency of the AO cell and phase coherent with the radar is summed to the radar signal, which has been heterodyned to the same frequency, and applied to the input transducer of the AO cell. The light diffracted by the cell consists of two separate waves: a converging wave due to the LFM radar signal and a collimated beam due to the reference signal. The resulting intensity distribution detected at the output plane in the x direction, for the nth pulse, is given by:

$$I(x',n) \sim | A + f_i'(x',vnT) |^2, \qquad (3.12)$$

where $f_i'(x',vnT)$ is given by Eq. 3.10. Assuming the source is perfectly coherent, Eq. 3.12 can be expanded as follows (The coherence requirements, and the effects of low coherence are addressed in Chap. 4.):

$$I(x',n) \sim A^2 + \sigma_0^2 \, \mathrm{sinc}^2[(x'-x_0')\bar{X}'b_i'] + 2A\sigma_0 \mathrm{sinc}[(x'-x_0')\bar{X}'b_i']\cos(b_2(vnT-y_0)^2(1-\alpha'x_0')+\mu_0). \qquad (3.13)$$

Eq. 3.13 consists of: a constant positive bias term determined by the strength of the reference signal, a positive radar signal dependent term, and a bipolar term that is modulated in n by the cosine of the phase history of the point scatterer. The last term carries the information needed to perform the azimuth compression.

This technique has a significant advantage over other interferometric approaches in that it is insensitive to

mechanical vibrations, since the interfering beams pass through the same optical elements. Furthermore, the OPDs between the interfering beams in this approach are small and thus minimize the temporal coherence requirements placed on the source, as we will see in Chap. 4. Additionally, since both interferometric beams are diffracted from the same AO cell, they are doppler shifted identically and therefore the fringes on the detector are stationary in time.

The results of a demonstration of the interferometric detection scheme are shown in Fig. 3.8. For these, and all subsequent experiments, a TeO_2 AO cell was used. This device was selected because of its large aperture (65 μsec) and diffraction efficiency (~ 100%/watt at λ=.83 μm). The bandwidth of this device is 30 Mhz (at the 2dB points). The SBWP of the AO cell is therefore approximately 2000, which is sufficient for most SAR applications. Furthermore, the acoustic velocity in the TeO_2 cell ($.62 \times 10^5$ cm/sec) is significantly lower than that of the quartz cell used earlier. The focal length of a 1-D Fresnel zone plate in the cell is therefore much shorter. The simulated radar signals used in this demonstration (with a chirp rate of 4×10^{12} Hz/sec) give a focal length (see Eq. 3.9) of approximately 11.5 cm. This focal length is sufficiently short to allow the spatially generated chirp to focus and be spatially separated from the undiffracted light as shown in Fig. 3.7, without the use of auxiliary lenses. The data

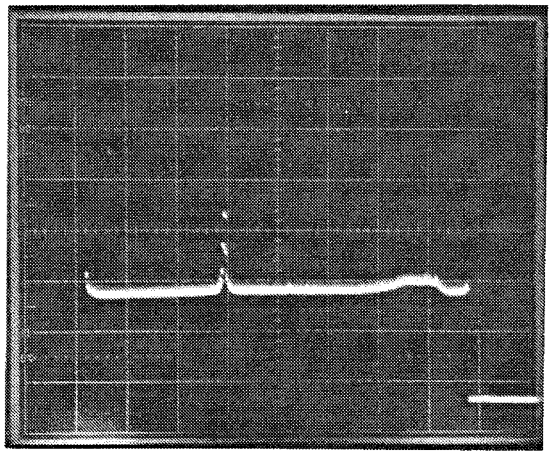

(a) range focused radar signal only.

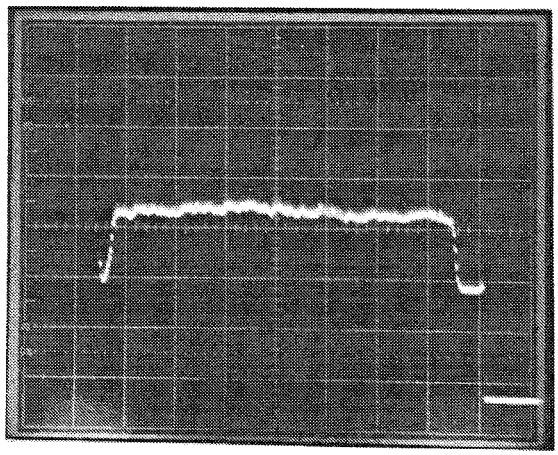

(b) reference signal only.

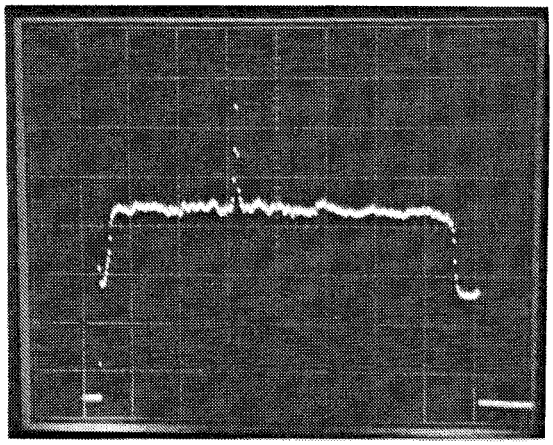

(c) range focused signal and reference signal: constructive interference.

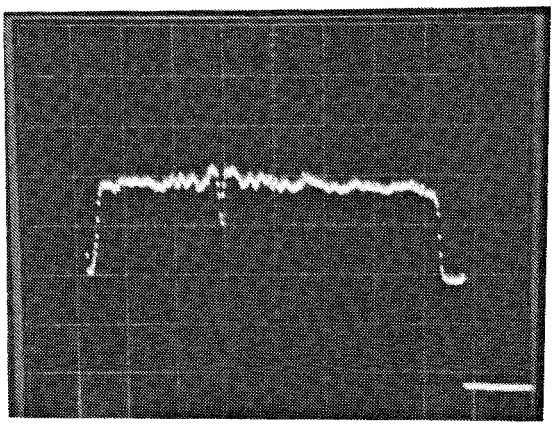

(d) range focused signal and reference signal: destructive interference.

Figure 3.8. Interferometrically detected phase history.

shown in Fig. 3.8 were collected on a 2-D time integrating CCD array whose operation will be discussed in the next section. For the purposes of this discussion the CCD can be considered to be a 1-D detector along the range coordinate axis. The prf for the data of Fig. 3.8 was 10 KHz and the integration time was approximately 1 sec. The data thus represents the summation of approximately 10^4 laser pulses. The laser diodes pulse width was 50 nanoseconds. Fig. 3.8a shows the CCD response when only the simulated radar return signal is present in the AO cell at the time of illumination. The nonzero baseline (present in all 4 traces of Fig. 3.8) is due to the integrated dark cell current. The range focused signal is contained in a range bin that is approximately 3 pixels wide (at 1/2 maximum). This signal corresponds to the second term in Eq. 3.12. The trace in Fig. 3.8b depicts the CCD response when only the sinusoidal reference signal is present in the AO cell during illumination and thus corresponds to the first term in Eq. 3.12. The level of the reference signal was adjusted to equal the range focused peak response. Figures 3.8c and 3.8d show the CCD's response to the sum of the reference and radar signals, and corresponds to Eq. 3.12 for different relative phases. In Fig. 3.8c the radar and reference signals are approximately in phase. This results in constructive interference as shown. In Fig. 3.8d the phase difference between the two signals was changed by

approximately π, which resulted in destructive optical interference at that range bin.

3.3.2 Time Integrating Azimuth Processor

The azimuth compression is performed with the temporal integration technique depicted schematically in Fig. 3.9. We will explain this technique by considering a single target in the range bin centered at $x'=x_0'$. The phase of the range focused signals is interferometrically detected, as described in the previous section, resulting in a sampled temporal intensity modulation over the sequence of radar returns as shown in Fig. 3.9. A 2-D CCD detector array is oriented at the range focus plane such that a 1-D array of pixels is located perpendicular to each range bin as shown in Fig. 3.9. The light from the AO cell is collimated in the y' direction to uniformly illuminate the CCD. To transform the ground azimuth coordinates into the vertical coordinate at the output plane of the processor we define $y_0'=y_0(\delta y/vT)$, where δy is the CCD pixel size in the azimuth dimension. Eq. 3.13 can then be rewritten:

$$I(x',n\delta y) \sim A^2 + \sigma_0^2\,\mathrm{sinc}^2[(x'-x_0')\bar{X}'b_1'] + 2A\sigma_0\,\mathrm{sinc}[(x'-x_0')\bar{X}'b_1']\cos(b_2'(n\delta y-y_0')^2(1-\alpha' x_0')+\mu_0), \quad (3.14)$$

where $b_2'=b_2(vT/\delta y)^2$. The azimuth pulse compression is performed by correlating the quadratic phase history of the radar returns with a spatial intensity modulation which

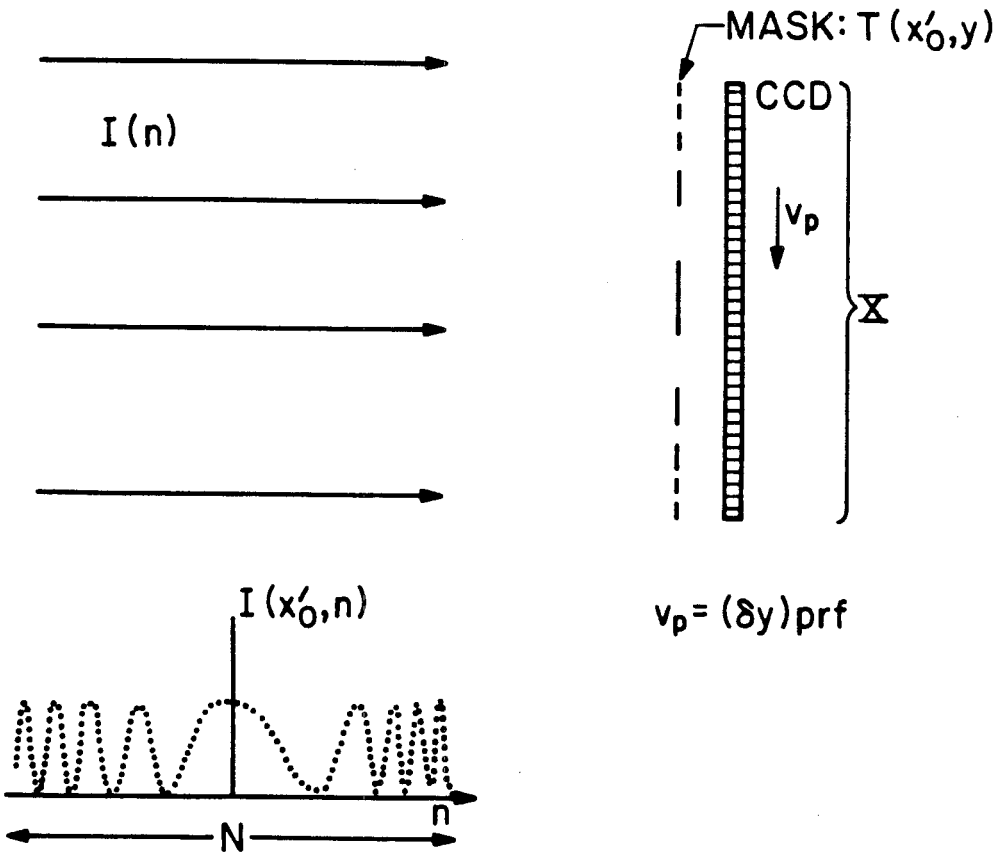

Figure 3.9. Time Integrating Processor that performs the azimuth compression.

matches the phase history for that particular range bin. The spatial modulation can be performed by a fixed intensity mask as shown in Fig. 3.9. The intensity transmittance of the mask at the range bin x_0' is made to be:

$$T(x_0',y') \sim (1 + \cos(b_1'(1-a'x_0')(y')^2), \qquad (3.15)$$

where y'=0 is at the center of the mask (or CCD). We assume there are N pixels (equal to the number of radar returns from a single point scatterer) for simplicity. The mask is

placed directly in front of, or imaged onto, the CCD. The CCD is operated in the shift-and-add mode, in the azimuth dimension, at a shift rate equal to the prf of the radar, thus giving the effect of a moving integrating linear detector array behind the stationary mask. The effective velocity, v_p, of the detector array is thus 1 pixel per radar return or (δy)prf. As the photogenerated charge on the detector moves across the mask, the charge that builds up on the detector array is given by:

$$Q(x',y') \sim \sum_{\bar{N}} I(x',n\delta y)T(x',n\delta y-y')$$

$$\sim NA^2 + N\sigma_0^2 \mathrm{sinc}^2[(x'-x_0')\bar{X}'b_1'] +$$

$$NA\sigma_0 \mathrm{sinc}[(x'-x_0')\bar{X}'b_1']\mathrm{sinc}[b_2'N\delta y(1-\alpha' x_0')(y'-y_0')]\cos\mu_0. \quad (3.16)$$

The third term in Eq. 3.16 is the range focused signal multiplied by the real part of the autocorrelation of the azimuth history phase function and thus represents the image of the scatterer focused in both the range and azimuth dimensions. The width of the focused signal along each axis is inversely proportional to the TBWP of the unfocused radar return along the respective axes, as desired. The other two terms in Eq. 3.16 represent interferometric artifacts which must be removed to obtain a high-quality image.

3.4 Combined Range and Azimuth Processors

The complete SAR Processor, shown in Fig. 3.10, is configured by cascading the space integrating range

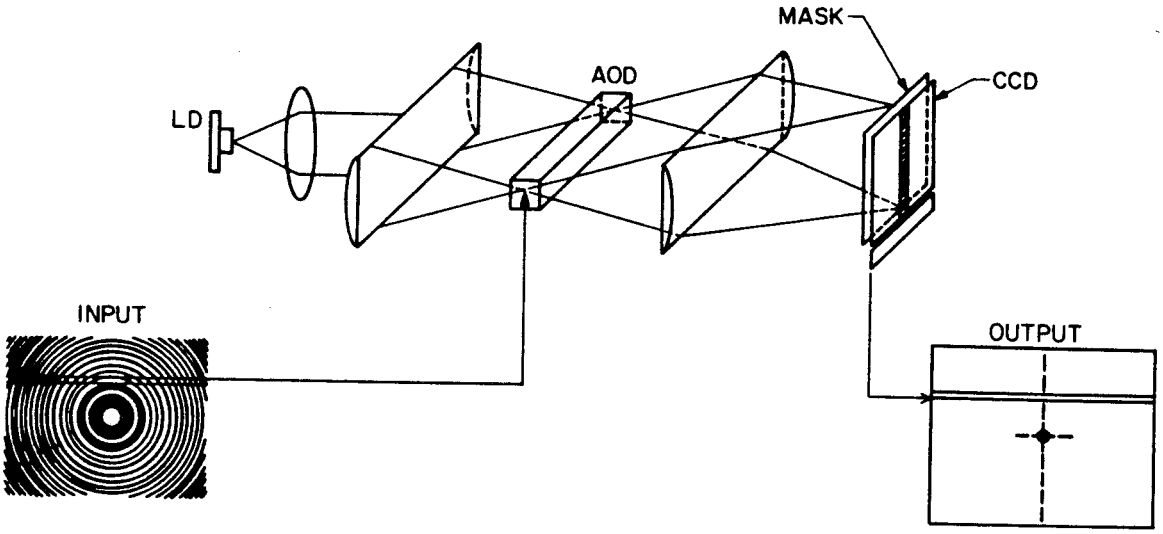

TOP VIEW (RANGE COMPRESSION)

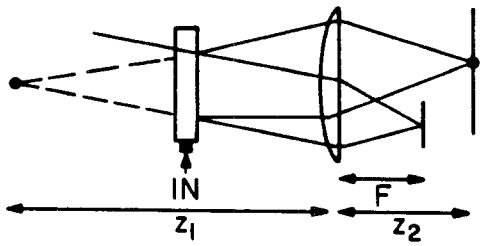

$$\frac{1}{z_1} + \frac{1}{z_2} = \frac{1}{F}$$

SIDE VIEW (AZIMUTH COMPRESSION)

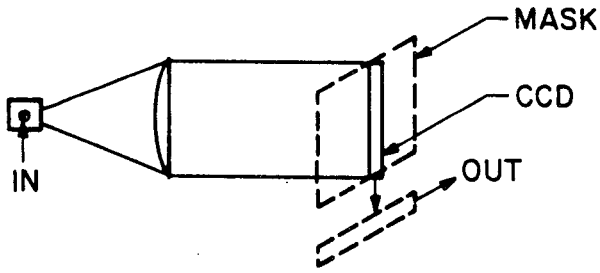

Figure 3.10. Acousto-Optic/CCD SAR Processor.

processor of Fig. 3.7 and the time integrating processor of Fig. 3.9. An example of the azimuth reference mask is shown in Fig. 3.11. The masks are generated with a computer controlled film recorder. The parameters of the mask shown in Fig. 3.9 were chosen to match the characteristics of the JPL airborne L-band SAR for the range bins between 12 and 15 kilometers, azimuth integration time of 1.6 seconds, and for an aircraft velocity of approximately .2 km/hr. Figure 3.12 is a sketch of the expected CCD output for a single point scatterer as given by Eq. 3.16.

A photograph of one implementation of the SAR processor is shown in Fig. 3.13. All of the optical elements and transducers were mounted on stages which allowed various translational and rotational degrees of freedom to facilitate alignment. We describe the optical components of the processor beginning at the left in Fig. 3.13. The laser diode was a Hitachi HLP-1600 single longitudinal mode device capable of 30 milliwatts output (pulsed) power. The laser drive electronics consisted of a DC biasing supply combined with a current pulser capable of 1 nsec risetimes, up to 200 nsec pulsewidths, and 20 KHz PRF. A spherical achromat was used as the collimating lens. The collimated beam was focused into the AO cell and recollimated after the AO cell with a pair of cylindrical lenses. The azimuth reference mask was placed at the focal plane of the induced 1-D Fresnel zone plate in the TeO_2 cell located

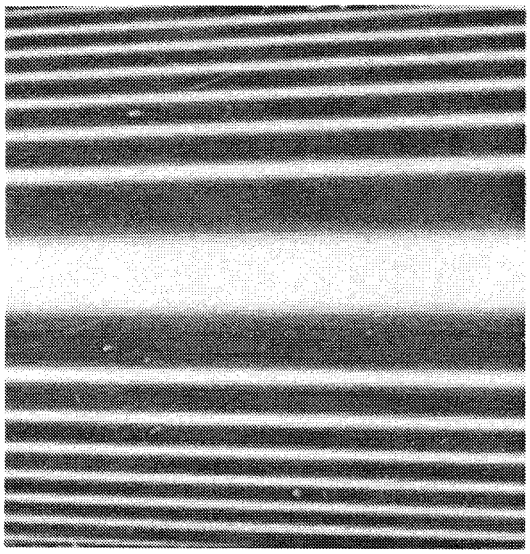

Figure 3.11. Azimuth reference mask.

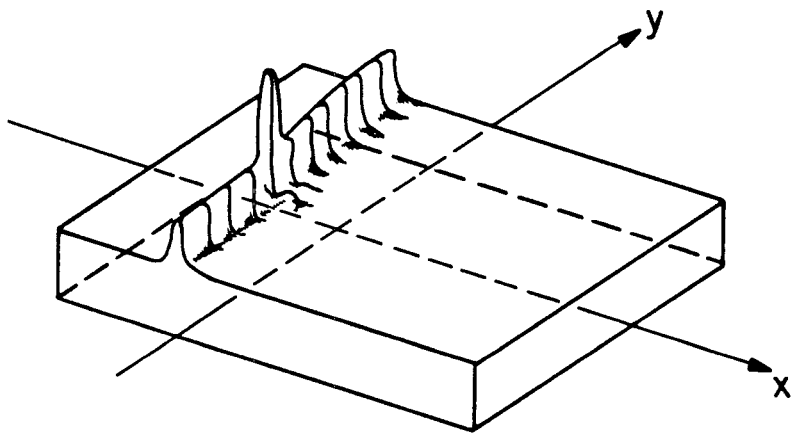

Figure 3.12. Expected Processor output for single point scatterer.

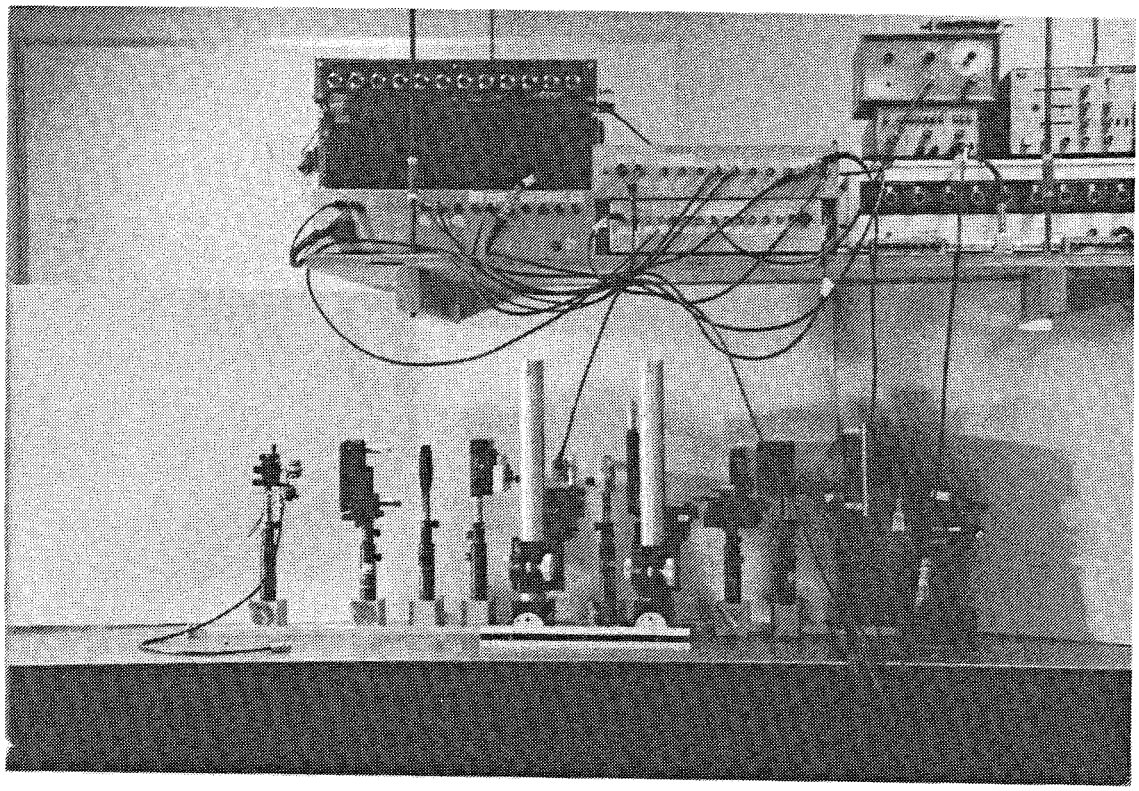

Figure 3.13. Experimental apparatus for AO/CCD SAR Processor.

approximately 11.5 cm away from the AO cell. A spherical lens was used to image the mask, with a magnification of 1, onto the CCD at the output plane. An iris aperture was used at the back focal plane of this imaging lens to block the undiffracted light. A cylindrical light shield was used to cut down on the scattered and ambient light which would add to the bias level and reduce the dynamic range. The CCD we used had 512 pixels in the vertical (azimuth) direction and 320 in the horizontal (range) direction, and a pixel size of approximately 30 micrometers on a side.

3.5 Characterization of the Processor

3.5.1 Radar Signal Simulator

The signal of Eq. 2.8 is referred to as the Impulse Response Signal since it is the expected signal from a point source scatterer. A radar signal simulator which generates the Impulse Response Signal has been built and is referred to as the Impulse Response Generator. A schematic diagram of the Impulse Response Generator is shown in Fig. 3.14. A 10 MHz master oscillator is devided by a factor of 2×10^4 to produce a phase locked PRF clock at 500 Hz. The same 10 Mhz frequency is used to derive a 60 MHz signal which is applied to the input of a digitally controlled phase shifter. The phase shifter is addressed by a read-only memory circuit in which a quadratic function is stored. An oscillograph of a typical quadratic function stored in the memory is shown in Fig. 3.15. The oscillograph in Fig. 3.15 was obtained through a D/A converter. The memory chip is read-out at the PRF of the radar and consequently the signal at the output of the phase shifter has a slow linear frequency modulation (typical bandwidths were ~20-80 cycles/frame in the experiments described later) which simulates the y variation of the signal in Eq. 2.8. The PRF clock triggers a circuit that produces a very short pulse (16.6 nanoseconds) which is in turn mixed with the phase shifted 60 Mhz carrier and applied to a surface acoustic wave (SAW) device. The dispersive properties of the SAW

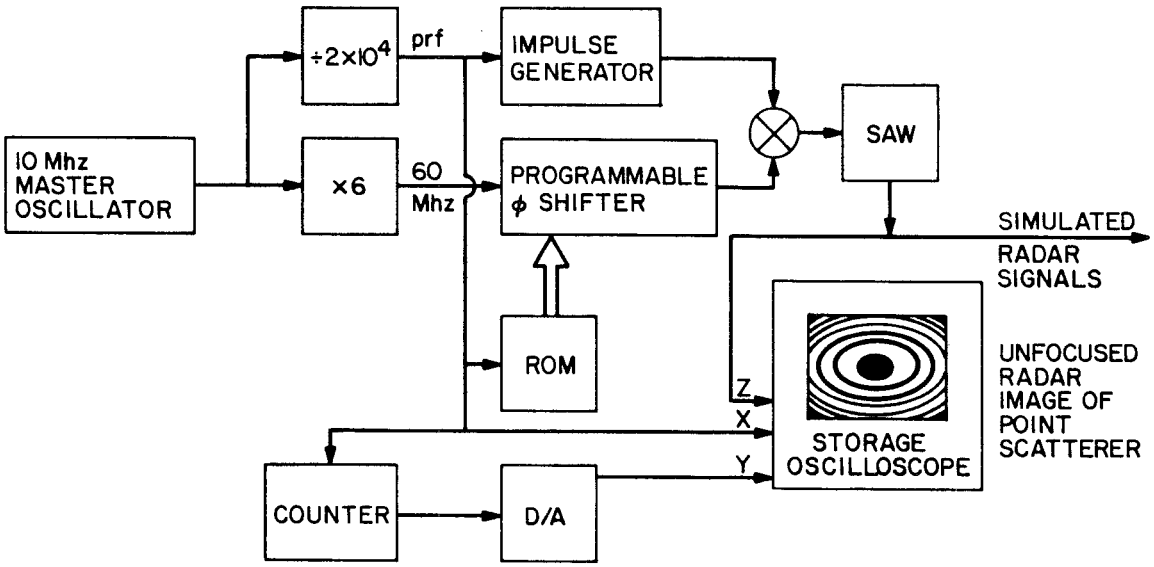

Figure 3.14. SAR Impulse Response Simulator.

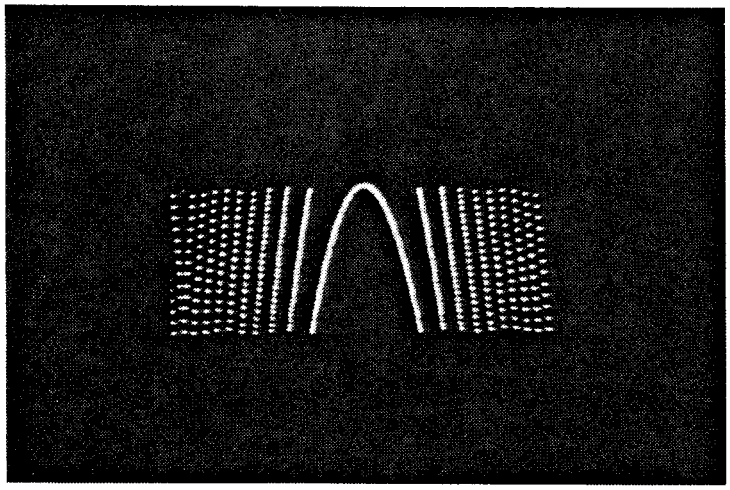

Figure 3.15. Quadratic phase modulation simulating the azimuth phase history.

device cause the impulses to be spread in time to approximately 6 μsec. and in frequency to the range 50 to 70 MHz. The SAW introduces the x modulation of the signal in Eq. 2.8. The output of the SAW is a replica of the signal that is received by a SAR illuminating only one point reflector. This signal is displayed by mixing it to baseband and modulating the intensity (z axis) of an oscilloscope. The horizontal (x) amplifier of the oscilloscope is triggered by the PRF clock and the vertical axis is deflected by a slow ramp. Fig 3.16 shows examples of the 2-D zone plates produced by the system described above for 3 different relative phase shifts. Each zone plate is a representation of the unfocused image of a point scatterer.

3.5.2 Impulse Response Experiment

To evaluate the real-time imaging ability of the SAR processor the Impulse Response Generator was interfaced to it as shown in Fig. 3.17. Timing circuitry was used to synchronize the laser pulser and the CCD clocking signals to the SAR Simulator. An isometric display was used to collect and store a frame of the CCD output and displays the focused image of the point scatterer in either a 2-D or 3-D perspective format for analysis.

An example of the raw output of the processor, when displayed in 3-D perspective, is shown in Fig. 3.18. Two views of the same data are shown. The focused image of a

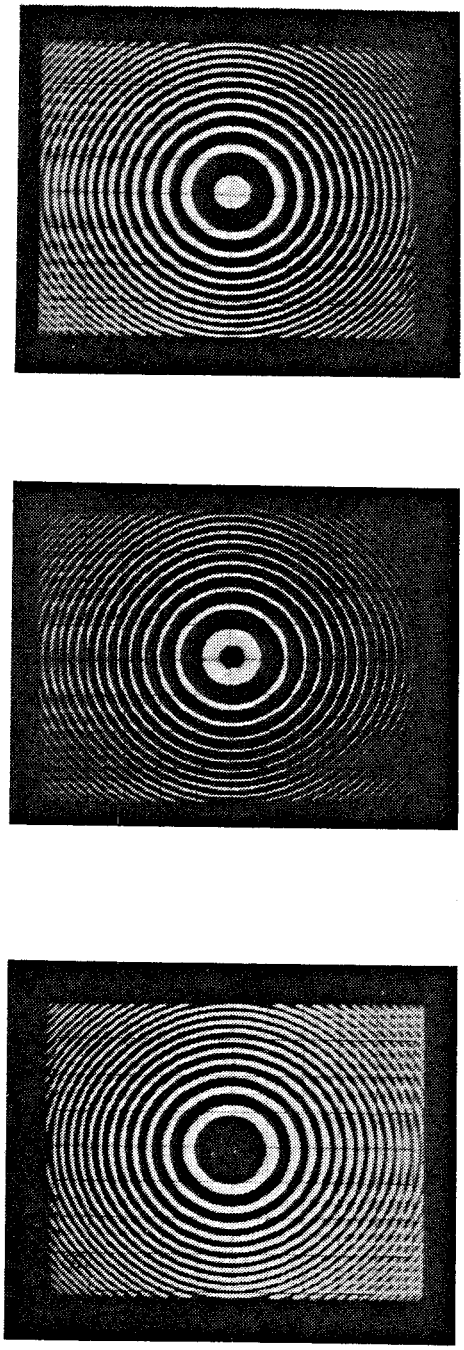

Figure 3.16. Unfocused images of point scatterer generated by radar simulator.

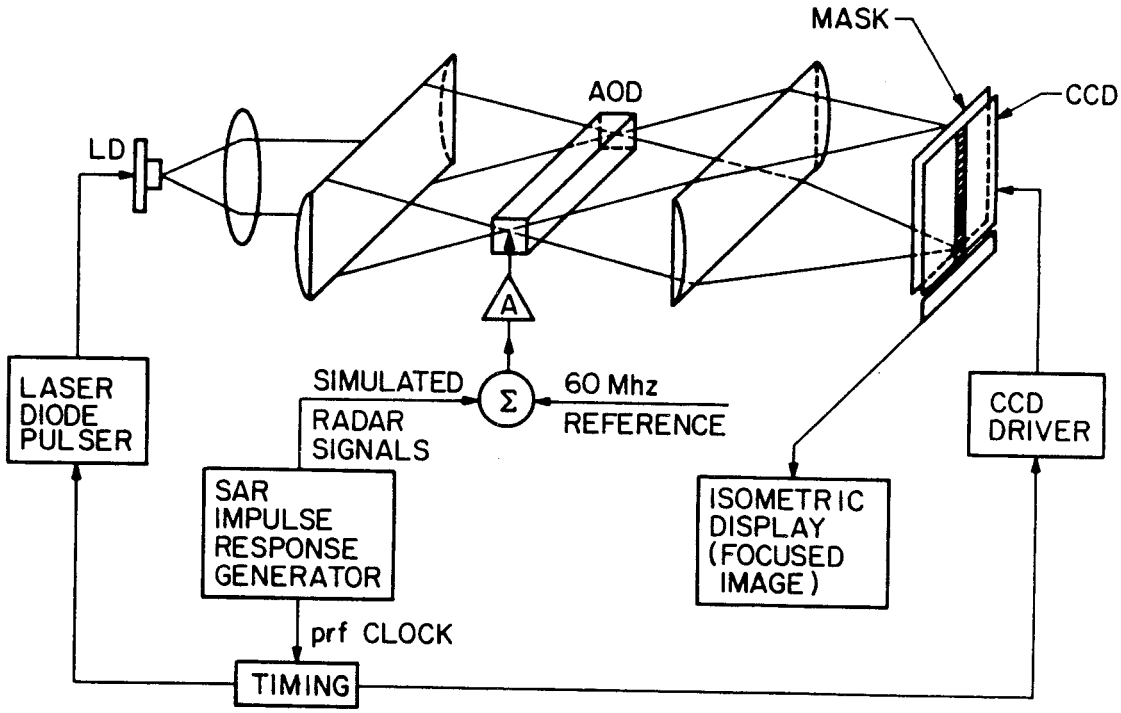

Figure 3.17 Impulse Response Experiment.

simulated point scatterer is visible as a narrow spike which sits upon the unwanted bias ridge located in the target's range bin. The SBWPs for the simulated unfocused image were ~ 130 and 320 for the range and azimuth dimensions respectively, and represent the highest resolution imagery evaluated with the experimental processor. The individual pixel structure is evident in the focused image. For demonstration purposes, the simulated target used in Fig. 3.18 had no quadrature component, i.e.,

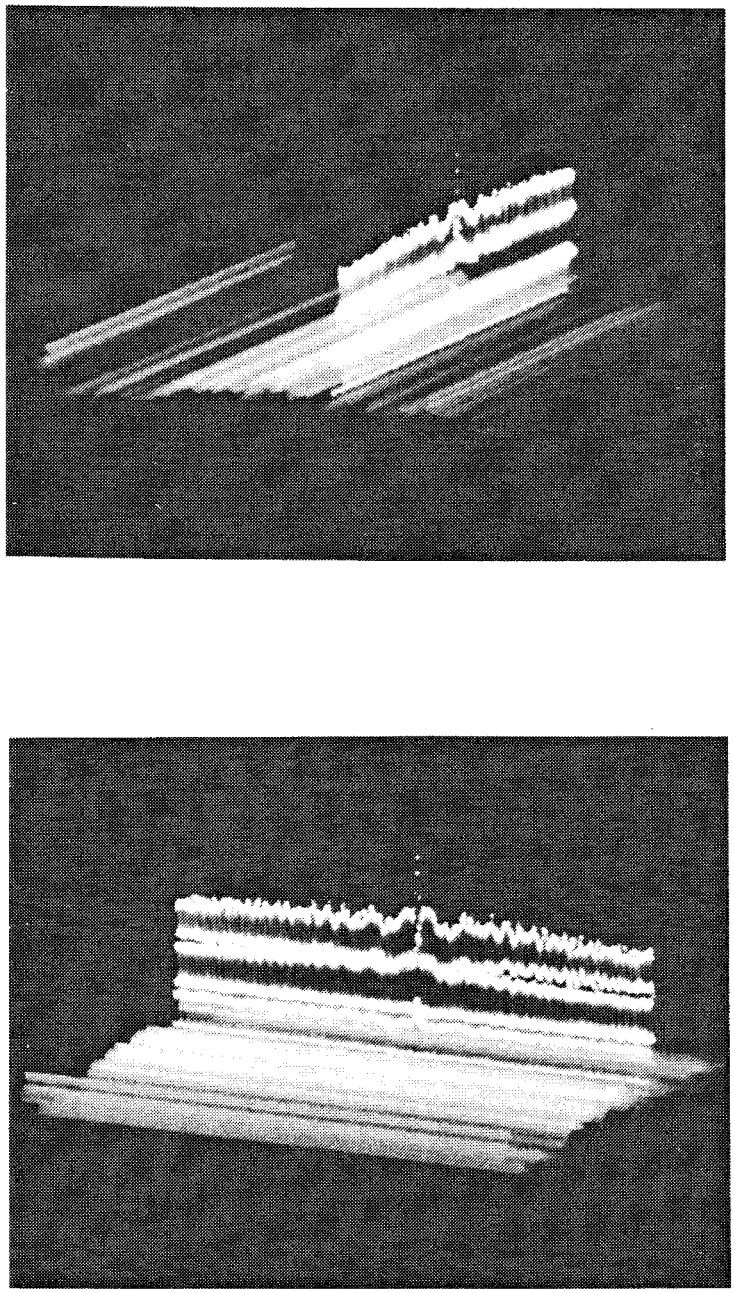

Figure 3.18. Isometrically displayed CCD output (from 2 aspects) for impulse response experiment.

$\mu_o = 0$. This insured that the peak was positive and had the largest amplitude possible. The usual side-lobe structure of a focused SAR scatterer, in the azimuth dimension, is evident along the bias ridge. The CCD's fixed pattern noise as well as the nonuniformity in the illumination of the reference beam are also visible on the floor beneath the ridge. These anomalies are integrated in each range bin due to the TDI action of the CCD.

3.5.3 First Experiments with Real Data

The results of the first demonstration of the SAR Processor with actual SAR data are shown in Fig. 3.19. This data was obtained from digitally recorded L-band data of the Pisgah, California area. The radar's azimuth window is approximately 15 seconds. Because the CCD in our processor operated at room temperature, we limited the integration time to approximately 1.6 seconds to keep the dark cell level at about 1/2 the CCD's well size. We therefore processed only about 1/10 of the available azimuth information in the recorded data. Because of this mismatch in processing windows, the dynamic range of the processor was limited and it was determined that, with this particular data, only very strong scatterers could be imaged with the existing processor. (The room temperature implementation of the processor is more well matched to higher frequency SARs, such as X-band, which can have shorter azimuth recording

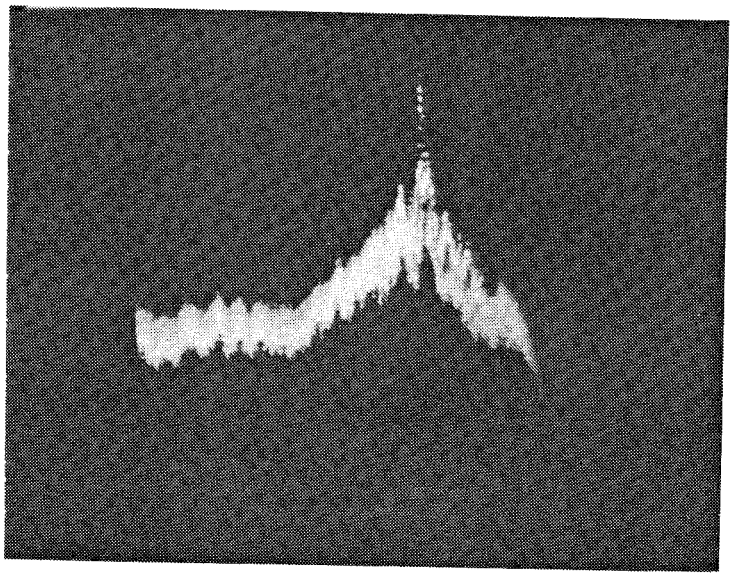

(a) $\mu_0 = 0.$

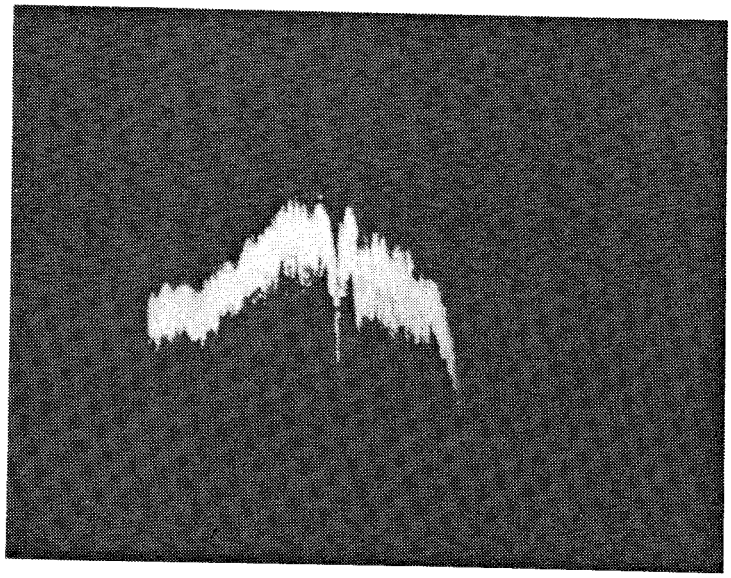

(b) $\mu_0 = \pi.$

Figure 3.19. Isometrically displayed iamge of strong scatterer (transmission tower) from recorded L-band airborne SAR data.

windows.) The figure shows two separate data runs of a range slice of a focused image of a single strong scatterer believed to be an electrical transmission tower. The range focusing (perpendicular to the data shown in the figure) was similiar to that achieved with the simulated data. In Fig. 3.19a the phase of the reference signal was adjusted to give the largest posible positive peak, i.e., $\mu_o = 0$. In Fig. 3.19b μ_o was set to π, resulting in a large negative going peak. The traces in Fig. 3.19 represent approximately 3 seconds of azimuth integration time. The triangularly shaped bias ridge results from the time integration of the approximately 1.5 seconds of azimuth information from the scatterer in the CCDs 1.6 second processing window. The doppler bandwidth of the azimuth information from this target was approximately 20 Hz, resulting in a resolution of about 10 meters. The actual data used to focus the point scatterer was found to be offset from 0 doppler by about 30 Hz, indicating that the scatterer had some directionality in its scattering characteristics.

CHAPTER IV. PEFORMANCE ISSUES

4.1 Bias Removal Techniques

As described in the previous chapter, the interferometric bias terms in Eq. 3.16 consist of a reference dependent pedestal term, which is ideally uniform over the entire CCD, and various signal dependent terms present in the range bins of every scatterer in the target field. Since the reference dependent bias is constant over the CCD, it will not degrade the overall image fidelity, and can be removed easily by direct subtraction from the CCD's electronic output. The signal dependent bias terms, however, are not, in general, constant, and cannot be removed by simple electronic means. If not removed, the signal dependent bias components can severely degrade the image quality by putting streaks in the range bins of each scatterer.

Several techniques are available for removing the bias components. In the most direct approach a second, identical, CCD detector array is incorporated into the architecture, on which only the bias terms are computed. The two CCDs are operated in synchronism and the video signal output from the second CCD is electronically subtracted from the video output of the original CCD to produce the bias free image. This technique is implemented using a beam splitter positioned in the beam before the mask as shown in

Fig. 4.1. The light that is split away from the main beam is range focused onto the second CCD, without azimuth processing (because there is no mask), resulting in a charge distribution that is proportional to the bias components of Eq. 3.16. In practice, the gain of the video signals is adjusted to compensate for gross differences in the illumination of the two CCDs due to the mask and the beam splitter. An isometric sketch of the output of the two CCDs for a scene with a single scatterer and the expected result of the subtraction is shown in Fig. 4.2.

Another approach to bias removal employs a specially designed CCD detector array which electronically subtracts the bias on the CCD chip itself.[15] In this technique auxiliary detectors on the array are used to detect the bias components. Circuitry, which is fabricated directly on the CCD substrate, is used to incrementally bleed off the bias charge as it builds up in the pixels. This approach maximizes the usable dynamic range of the CCD.

In a third bias removal technique the focused SAR image is generated on a spatial carrier frequency. The bias components are not modulated by the spatial carrier and are removed by electronic post-processing of the CCD video output. The carrier is generated either in the range or azimuth dimension by introducing the appropriate frequency shifts in the electronic signals and mask. Demodulation consists of electronic filtering to detect only those

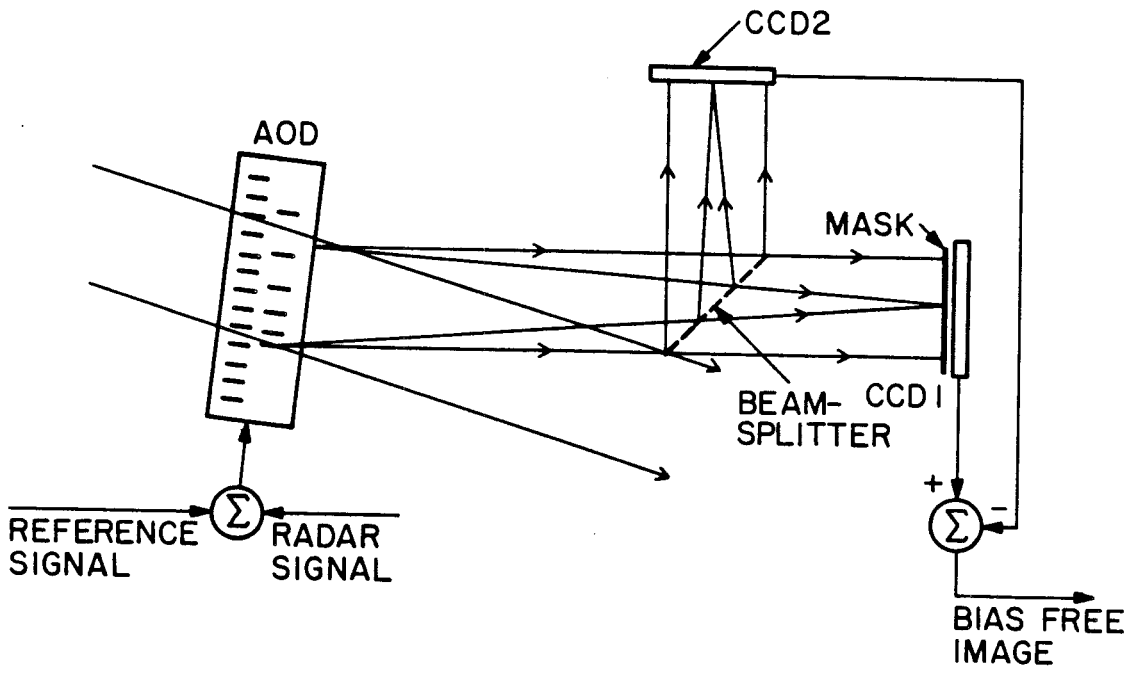

Figure 4.1. Bias removal by direct subtraction.

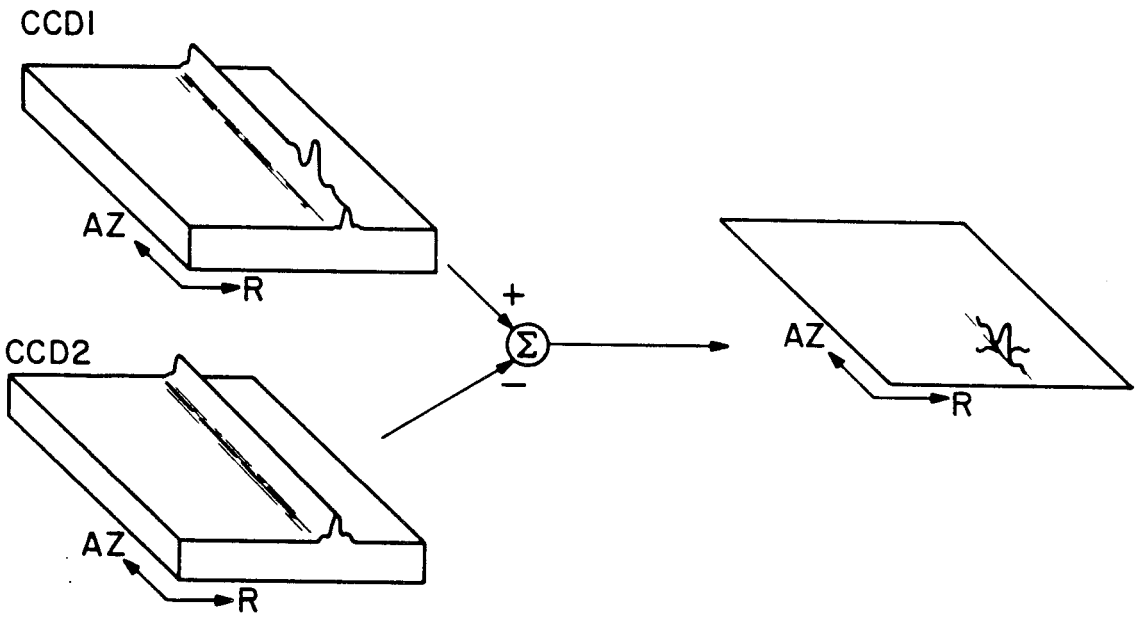

Figure 4.2. Pictoral representation of CCD outputs and resultant image for direct subtraction approach.

components which are on the carrier, followed by rectification to clip negative components and envelope detection to remove the carrier frequency from the image. The processing steps for this technique are shown pictorially in Fig. 4.3 for the case of a carrier in the azimuth dimension.

Each of the described bias removal techniques has advantages and disadvantages associated with them. The direct subtraction technique uses the full resolution capability of the CCD because no carrier is employed which would require several pixels per cycle. However, this approach has the disadvantages of the cost of the additional CCD and the difficulties associated with the alignment of the two CCDs. Furthermore, only the real (or imaginary) part of the image can be determined with a single processor employing this technique. To fully determine the amplitude of every scatterer in the field, two complete processors must be used, one to detect the in-phase (I) components and one to detect the quadrature (Q) components. The bias subtraction CCD maximizes the usable dynamic range of the CCD, however, at present, such devices do not exist. The carrier encoding bias removal schemes cannot use the full resolution of the CCD and are limited by the MTF of the CCD at the selected carrier frequency. However, CCDs are now available with very large arrays (up to 2048 x 2048), thus minimizing the need for single pixel resolution.

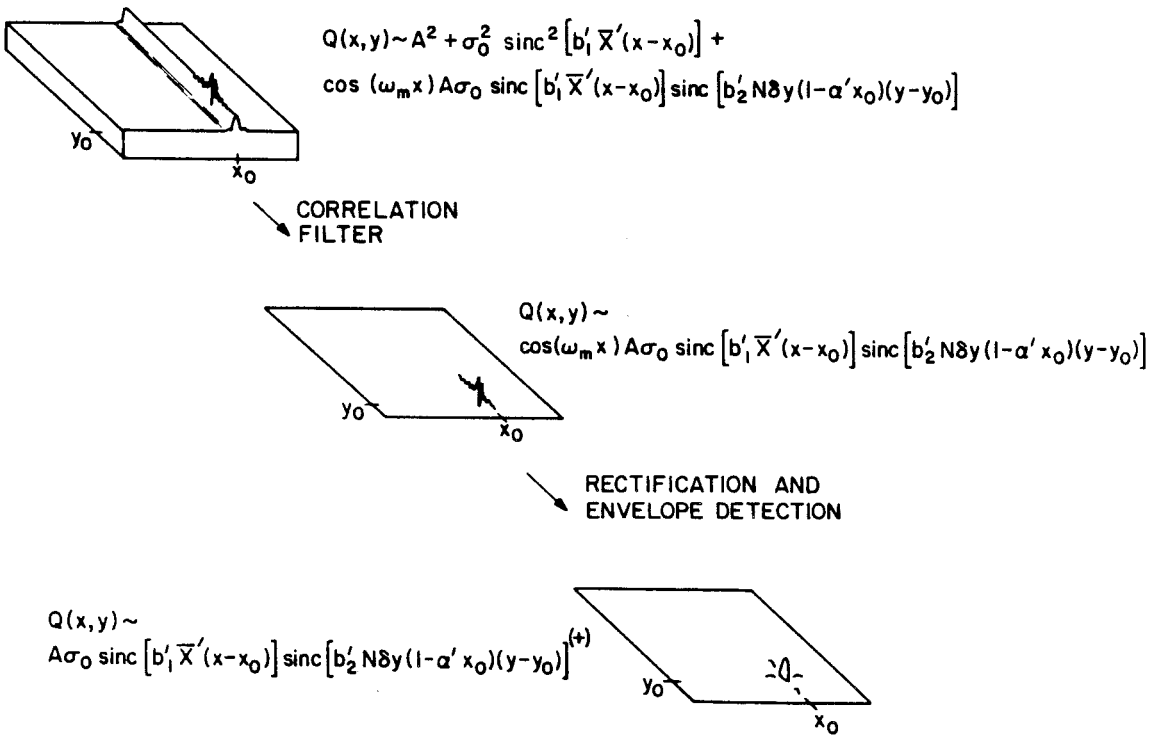

Figure 4.3. Bias removal by azimuth carrier encoding and demodulation.

Additionally, CCD MTFs are typically sufficient to use carrier frequencies with periods as low as several pixels/cycle. Furthermore, since envelope detection is used, this approach requires only one CCD to detect the amplitude distribution of the target field. For these reasons we elected to demonstrate bias removal using the carrier demodulation technique. In the following section we describe the implementation and results of this demonstration.

4.2 Demonstration of Bias Removal

4.2.1 Generation of the Azimuth Carrier Frequency

In choosing the optical carrier frequency there is a trade-off between resolution and signal level. The overall signal level is limited by the frequency response of the system, which, in turn, is principally determined by the MTF of the CCD. We arbitrarily selected .5 as an acceptable lower bound on the MTF and found (see section 4.3.7) that this corresponds to a spatial frequency of about ω_m=1/6 cycle/pixel with our system. To insure that the carrier modulated image is well separated in the frequency domain from the DC and low frequency components of the bias, we required that the azimuth focused target be wide enough to contain about 2 cycles, or 12 pixels, of the optical carrier. If we assume that the narrowest (in azimuth) focused image of a scatterer is 12 pixels across at the zero

crossings, then, since our CCD has 512 pixels along the azimuth dimension, we are limited to processing signals with azimuth TBWPs which are less than or equal 2x512/12~85. Figure 4.4 is the predicted CCD response, without carrier encoding, to a target whose TBWP in the azimuth direction is 80. Figure 4.5 is the predicted CCD response for the same signal with carrier encoding at 1/6 cycle/pixel. The phase of the carrier with respect to the envelope in Fig. 4.5 is arbitrary. Furthermore, gaussian apodization of the azimuth reference function has been included to simulate the effects of the laser diode's beam profile. The apodization window used in the simulation of Fig. 4.5 has a value of 1/e at the edges of the processing window and has the effect of reducing the sidelobe response at the expense of some broadening of the central lobe. (The effects of apodization are discussed in more detail in section 4.3.8.)

To produce the desired azimuth carrier modulation the reference function recorded on the mask must be modulated by ω_m, and the temporal azimuth phase history of the target must be modulated up to $\omega_m v_p$, where v_p is the effective pixel velocity due to the TDI action of the CCD, as defined in section 3.3.2. The required intensity transmittance of the reference mask is (by modifying Eq. 3.15):

$$T(x_0',y') \sim (1 + \cos(\omega_m y' + b_2'(1-\alpha' x_0')(y')^2). \qquad (4.1)$$

After upshifting the azimuth phase history by $\omega_m v_p$, the

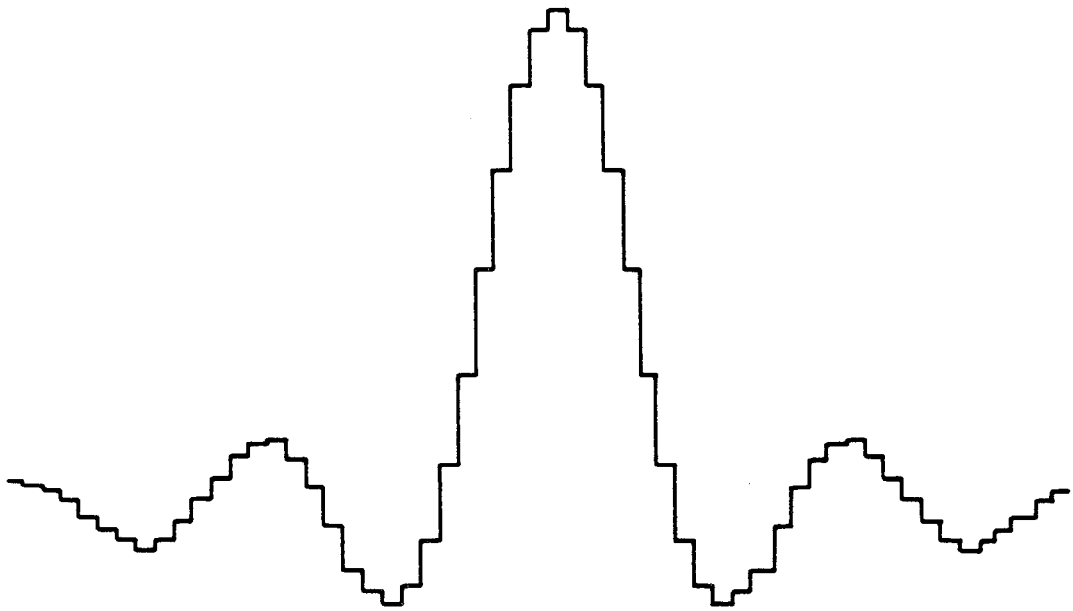

Figure 4.4. Digital simulation of CCD response in azimuth direction (without carrier encoding) for signal with TBWP=80.

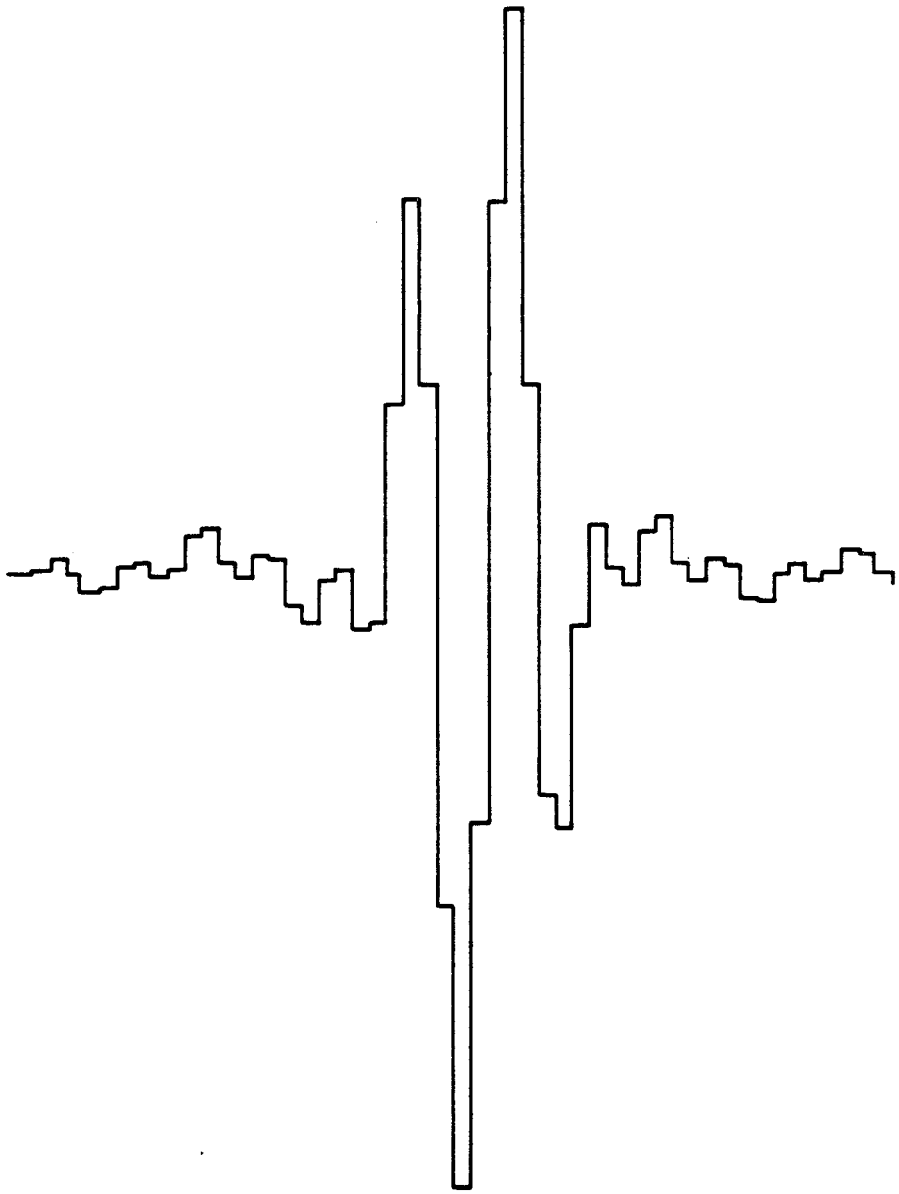

Figure 4.5. Predicted CCD response to signal with TBWP =80 and carrier encoding at 1/6 cycle/pixel.

temporal modulation of the intensity of the nth range focused radar return for a single scatterer is (by modifying Eq. 3.14):

$$I(x',n\delta y) \sim A^2 + \sigma_o^2\,\mathrm{sinc}^2[(x'-x_o')\bar{X}'b_i'] + 2A\sigma_o\mathrm{sinc}[(x'-x_o')\bar{X}'b_i']\cos(\omega_m n\delta y + b_2'(n\delta y-y_o')^2(1-\alpha' x_o')+\mu_o). \tag{4.2}$$

The resulting charge distribution on the CCD due to the temporal integration of N sequential radar returns is (similiarly to Eq. 3.16):

$$\begin{aligned} Q(x',y') &\sim \sum_{\bar{N}} I(x',n\delta y)T(x',n\delta y) \\ &= NA^2 + N\sigma_o^2\mathrm{sinc}^2[(x'-x_o')\bar{X}'b_i'] + \\ &\quad NA\sigma_o\mathrm{sinc}[(x'-x_o')\bar{X}'b_i'] \quad x \\ &\sum_{\bar{N}}\cos(\omega_m n\delta y+b_2'(n\delta y-y_o')^2(1-\alpha' x_o')+\mu_o)\cos(\omega_m n\delta y+b_2'(1-\alpha' x_o')(n\delta y)^2). \end{aligned} \tag{4.3}$$

With the previously mentioned assumption that the period of ω_m is 1/2 the width of the azimuth focused peak, then Eq. 4.3 reduces to:

$$Q(x',y') \sim NA^2 + N\sigma_o^2\mathrm{sinc}^2[(x'-x_o')\bar{X}'b_i'] + NA\sigma_o\mathrm{sinc}[(x'-x_o')\bar{X}'b_i']\mathrm{sinc}[b_2'N\delta y(1-\alpha' x_o')(y'-y_o')]\cos(\omega_m y+\mu_o), \tag{4.4}$$

which is identical to Eq. 3.16 with the signal component

modulated with the spatial carrier ω_m in the azimuth direction as shown in Fig. 4.3.

4.2.2 Azimuth Demodulation

The spatial frequency domain representation of the azimuth focused signal, with and without carrier encoding, is shown in Fig. 4.6. The obvious result of carrier encoding is the separation of the image signal from the DC and lower frequency components of the bias. The removal of bias components, therefore, requires a high-pass filter which blocks the undesired components, but passes the modulated components without significant distortion. We have implemented an electronic correlation filter whose characteristics approximate the desired high-pass filter. This filter is shown schematically in Fig. 4.7. Digital delay lines with weighted taps are used to form a 12 tap azimuth filter for the image. The delay in each stage is equal to the period of 1 video line from the CCD. The number of taps was selected at 12 in the filter so that its impulse response would contain up to 2 full cycles of the selected carrier frequency, ω_m, as shown in the example weighting function in Fig. 4.7. The output of the filter consists of an approximation of the image on a carrier. The final image is obtained by rectifying and envelope detecting the filter output. Fig. 4.8 shows the results of digital simulations of the output of the filter, for the carrier modulated input shown in Fig. 4.5, for various weighting

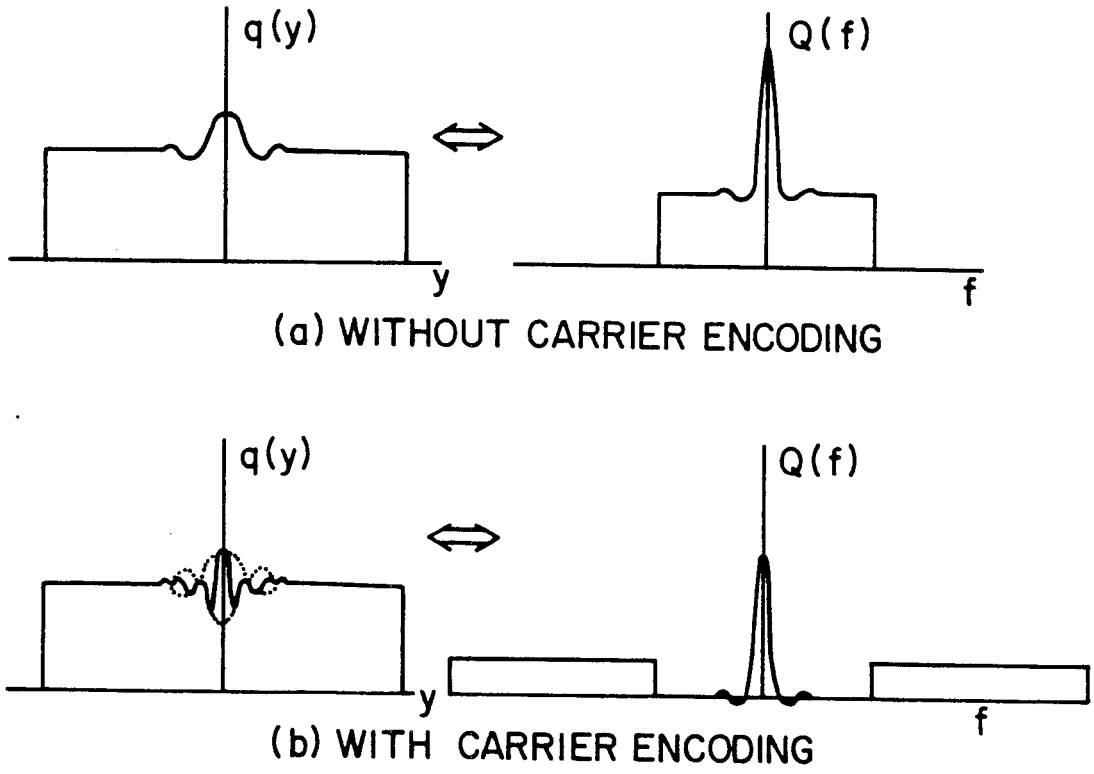

Figure 4.6. Separation of signal from bias terms with carrier encoding

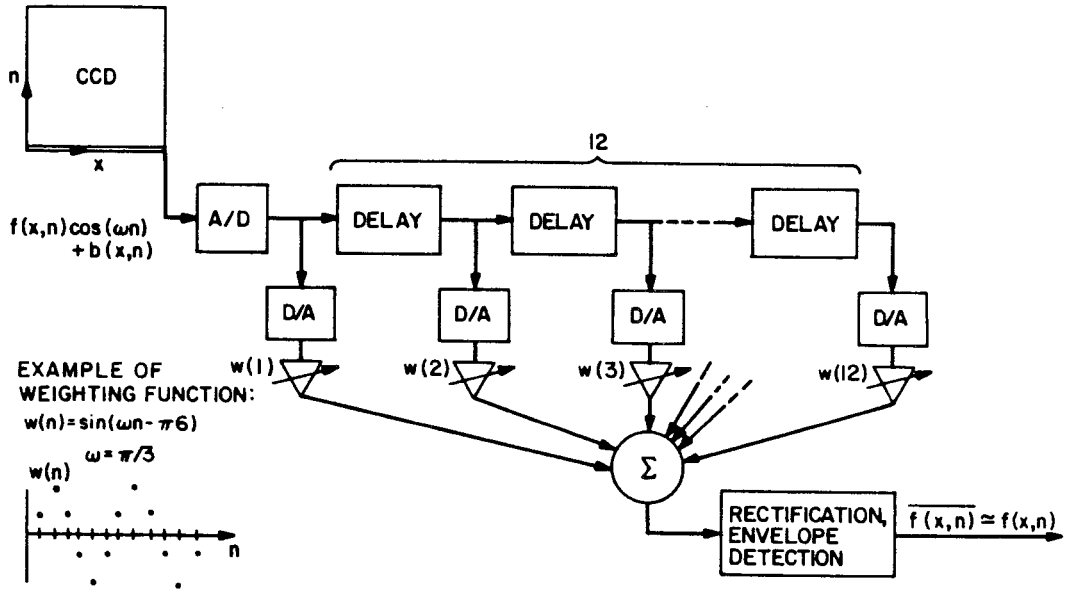

Figure 4.7. Real-time SAR Processor Output Demodulator for Image on Azimuth Carrier.

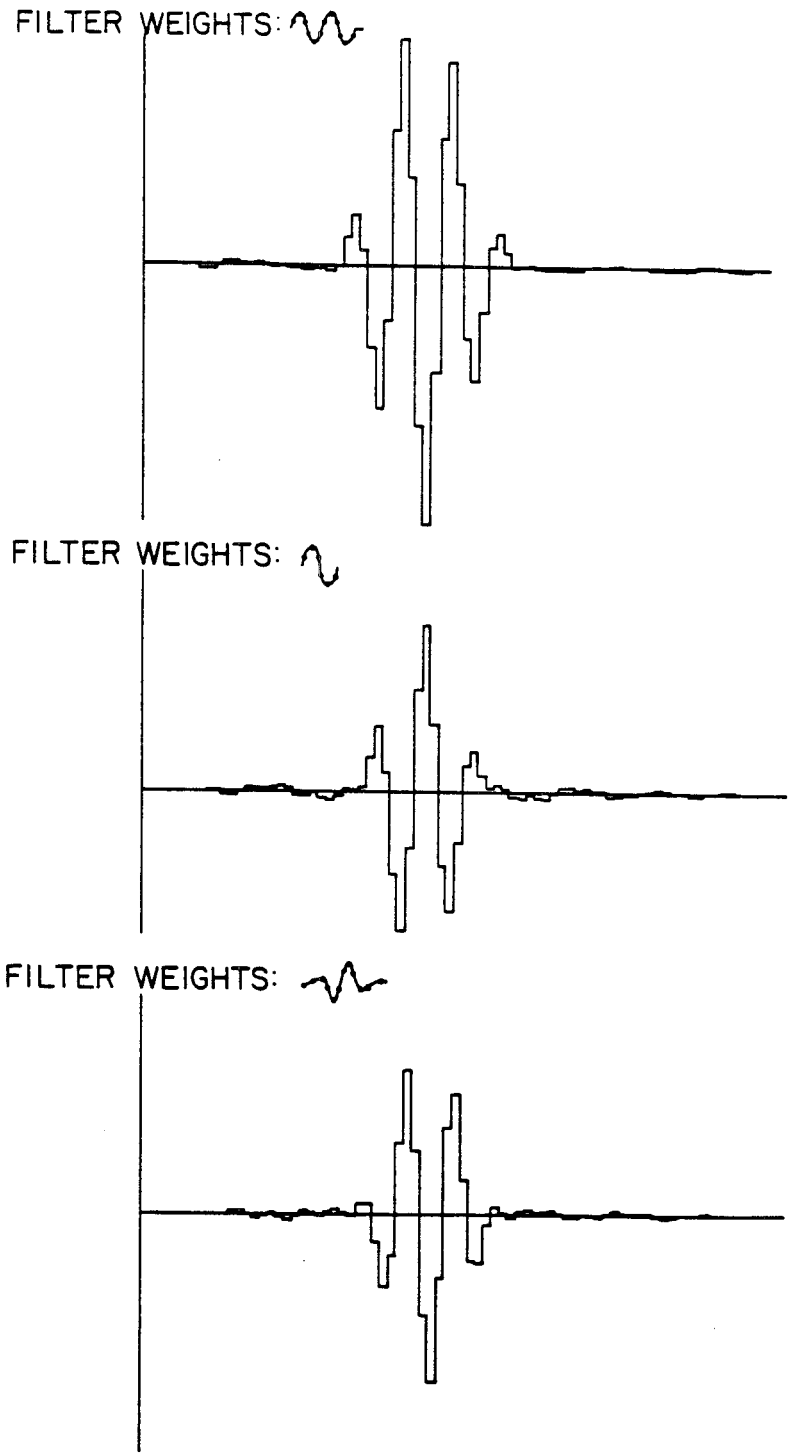

Figure 4.8. Simulated Response of Azimuth Correlation Filters

functions. Each of the example filters reduces the sidelobes of the azimuth compressed signal, with some widening of central lobe. Note that the response to the unapodized, 2 cycle filter has the lowest side lobe response, but the broadest central lobe.

4.2.3 Bias Removal Results

The filter described above was interfaced to the SAR processor and simulated radar targets, with azimuth TBWPs of 80, were processed. Examples of the imagery produced by the filter are shown in Fig. 4.9. For this data the weighting function used corresponded to that shown in Fig. 4.8a. In Fig. 4.9a the image of a single point scatterer is displayed isometrically. A 2-D display of a sequence of simulated point scatterers is shown in Fig. 4.9b. In Fig. 4.9 the display device performs the functions of rectification and envelope detection. The data clearly show that, not only have the bias terms been removed successfully, but also the fixed pattern noise, due to the combination of the irregularities in the laser beam, AOD, and CCD, has been removed to provide a more uniform noise floor.

The action of the azimuth correlation filter on individual lines of the video signal of the CCD is shown in the oscillographs of Fig. 4.10. The top traces in the two oscillographs are of different lines of the ouput of the CCD which is the input to the correlation filter. Each video line out of the CCD corresponds to a different azimuth slice

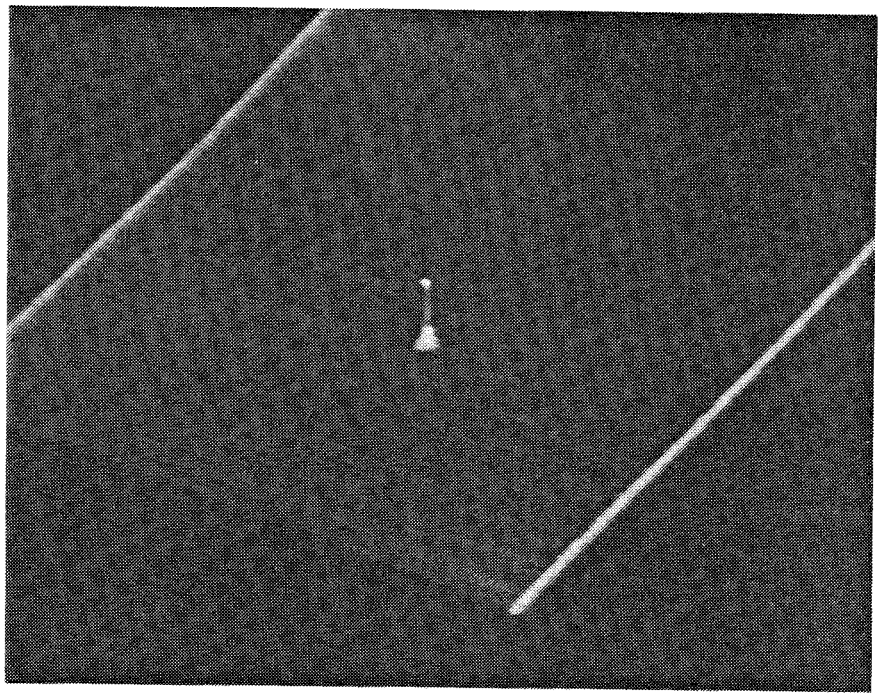

(a) Isometrically displayed image of single scatterer.

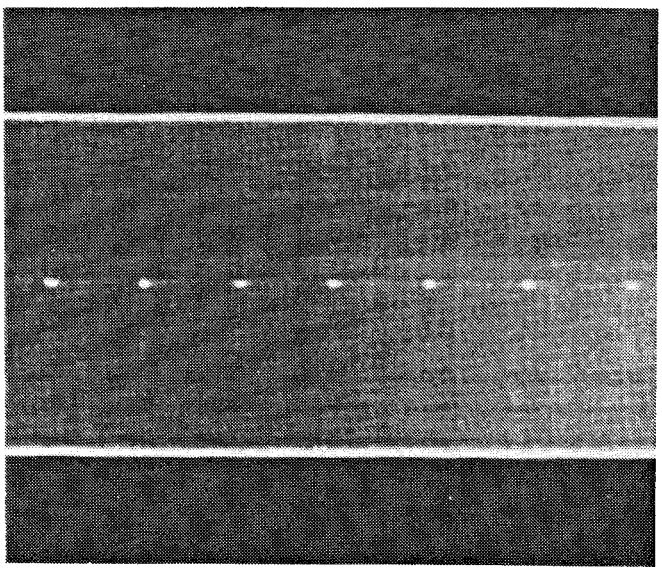

(b) 2-D display of string of simualated scatterers.

Figure 4.9. Demodulated images of simulated point scatterers showing removal of bias signals and fixed pattern noise.

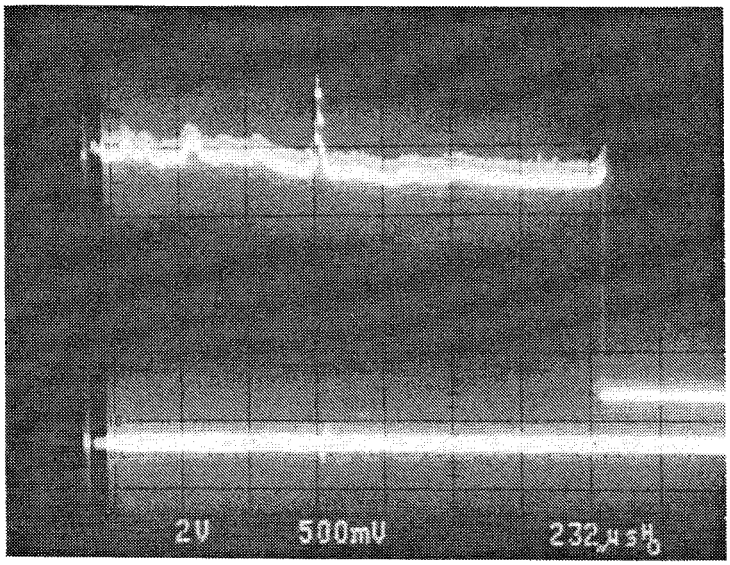

(a)

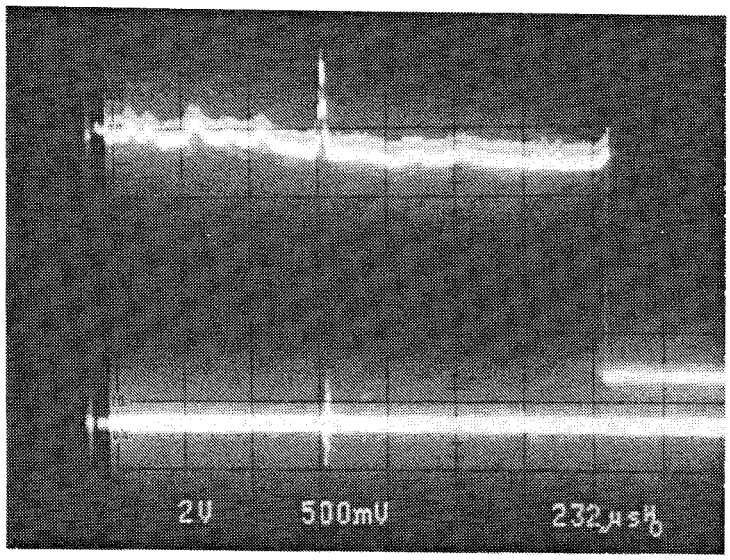

(b)

Figure 4.10. Azimuth correlation filter input and output video signals.

of the target scene. The bottom traces are the corresponding output lines of the correlation filter. In Fig. 4.10a the CCD output was not sampled in the vicinity of the azimuth peak, leading to negligible response from the filter. Note, however, that the filter has removed the bias ridge component and the fixed pattern noise which varies as a function of range along the CCD video line. The response of the filter to the CCD output at an instant when the carrier modulated azimuth peak is being output is shown in Fig. 4.10b. The azimuth compression on the CCD signal is evident as a blurring on top of the bias ridge component (compare with Fig. 4.10a), and the corresponding bias-free image slice is shown below it.

Fig. 4.11 shows isometric views of the focused simulated radar signals with the same azimuth TBWPs, with and without carrier encoding. In Fig. 4.11b the carrier is visible under the azimuth compressed and rectified image. The outputs of the processor, with and without bias removal, are very similar to the predicted outputs shown in Figs. 4.4 and 4.8.

4.3 Dynamic Range

4.3.1 Theoretical Limits to Dynamic Range

One of the most critical parameters of the A-O SAR Processor is the dynamic range of the output data. The dynamic range is determined by the characteristics of the active components of the processor. The basic limitation

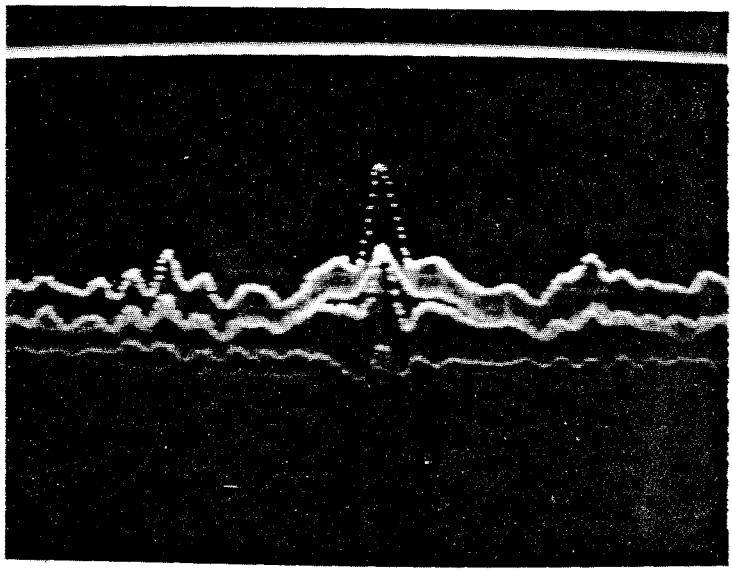

(a)

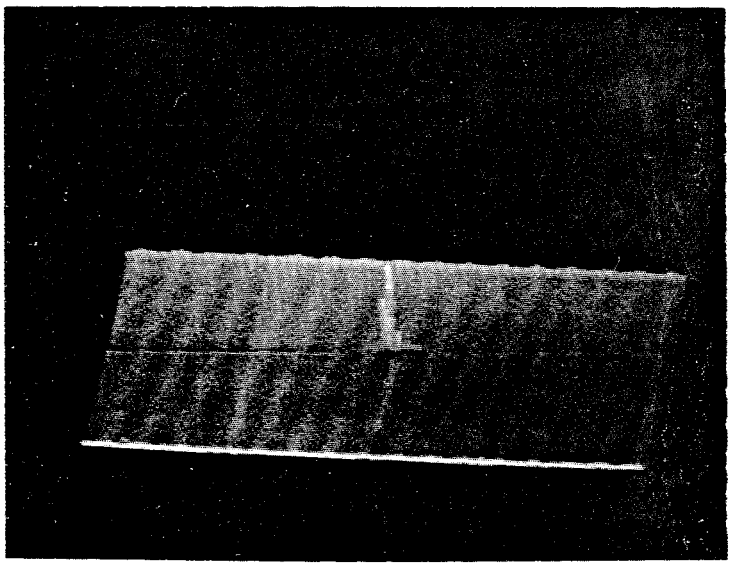

(b)

Figure 4.11. Comparison of processor output with and without carrier encoding.

arises from the CCD detector array. The CCD's dynamic range, in terms of the charge located at each pixel, is given by:

$$D_o = \frac{N_m - N_d}{N_n}, \qquad (4.5)$$

where N_m, N_d, and N_n are, respectively: the maximum number of electrons that can be stored, the average number of electrons resulting from the dark current, and the standard deviation of the number of electrons arising from the various noise processes. N_m is approximately 250,000 for the RCA CCD array used in the experiments. N_d is a linear function of time and an exponential function of device temperature. At room temperature, CCD detectors have typical storage times, i.e., the time it takes the dark current to completely fill the well, of between .1 and 10 seconds. The storage time for the device we used is approximately 3 seconds. Therefore, we can rewrite Eq. 4.5 in the following manner:

$$D_o = \frac{N_m - \Omega T}{N_n}, \qquad (4.6)$$

where T is equal to the data collection time and Ω, for the device we use, is approximately $N_m/3$ (electrons/sec.). In the SAR simulator experiments that have been reported previously, a data collection period of 1 second was used; therefore approximately 1/3 of the available dynamic range was used up by the dark current. For applications requiring

longer integration time, the device must be cooled to reduce the dark current. The dark current is a strong function of temperature; cooling the device by $10^{o}C$ near room temperature results in approximately a factor of 2 reduction in dark current. The various noise processes that contribute to N_n include: signal shot noise, dark current shot noise, CCD transfer noise, fixed pattern noise, on-chip MOSFET noise, and off-chip amplifier noise. For the CCD devices we use the theoretical limit on D_o is approximately 1000:1.

Fundamentally, for a single scatterer, the use of interferometry to detect the azimuth phase history of the target limits the dynamic range to $D_o/3$. This limit is due to the interferometric bias needed to process the bipolar information on a unipolar detector, and the fact that the radar return signals have zero mean. The dynamic range of the output, for a focused point scatterer that is part of an image, is reduced from this limit by contributions to the bias from other point scatterers located in the same range bin and within the same azimuth processing window. Also, the amplitude of the CCD signal for each focused scatterer is proportional to the fringe visibility of the processor. The fringe visibility is determined principally by the temporal coherence function of the pulsed laser diode and the combined optical path differences induced by the Bragg diffraction in the AOD. The MTF of the CCD also affects the

dynamic range. The MTF describes the roll-off in the response of the CCD with increasing spatial frequency. With the bias removal scheme that employs a spatial carrier and synchronous demodulation, the signal level on the CCD will be reduced by the MTF of the CCD at the spatial carrier frequency used.

4.3.2 Optimum Bias

For a focused image with a resultant signal height, s, on the CCD, and bias level, b, the dynamic range is given by:

$$D = D_o \frac{s}{s + b} = D_o \frac{s/b}{1 + s/b}. \qquad (4.7)$$

Thus we see that it is the signal-to-bias ratio which must be maximized to achieve the highest dynamic range.

To derive an analytical expression for the signal-to-bias ratio and hence the dynamic range we need consider only one typical range bin. This is because the interferometric processing which leads to inter-target bias contributions occurs only along the time-integrating (azimuth) dimension. Once an expression for the CCD output, s + b, is determined, then the signal and bias components can be identified and the signal-to-bias ratio maximized. In the following analysis we assume that the signal term is placed on a spatial carrier, ω_m, in the azimuth direction, and that the previously described demodulation scheme to remove the bias

by electronic post processing is employed. In this case the smallest feature on the CCD will be a cycle of the carrier frequency.

A total of N samples are integrated in the azimuth compression operation. The resolvable scatterers in this range bin are assumed to have an average **amplitude** equal to σ_{av}. The interferometric reference signal is defined to have an amplitude of A. The average amplitude of the radar return signal, which is due to all the individual scatterers in the azimuth processing window, is equal to S. $M = (S/\sigma_{av})^2$ is an upper bound on the number of resolved scatterers contributing to the bias at any point of interest. The strongest scatterer that we wish to focus without saturating the CCD is defined to have an amplitude of $\sigma_{max} = R(\sigma_{av})$. Since we assume envelope detection is used to remove the carrier frequency from the demodulated image, we ignore the arbitrary constant phase factor between the two signals being correlated in the azimuth dimension.

With the above assumptions, the total charge that builds up on the CCD at the location of a scatterer with amplitude σ_{max} is given by:

$$s+b \simeq \sum_{N} [\, A^2 + S^2 + 2A\sigma_{max} G\, H_m \cos(b(n\delta y)^2 + \omega_m n\delta y) \,] \; [\, 1 + \cos(b(n\delta y)^2 + \omega_m n\delta y) \,]. \quad (4.8)$$

G is the amplitude of the coherence function between the

range focused and reference optical beams. H_m is the MTF at the carrier frequency, ω_m, and b is the chirp rate of the reference chirp at that particular range bin. The first term in brackets represents the optical intensity, while the second term in brackets represents the intensity modulation of the azimuth reference mask. Carrying out the summation in the above equation, we find:

$$s + b \sim N[\ \sigma_{max}AGH_m + A^2 + S^2\ ]. \qquad (4.9)$$

The first term contained in the brackets in Eq. 4.9 is the desired signal term, while the others are the bias terms. Hence the signal-to-bias ratio can be written:

$$s/b = \sigma_{max}AGH_m \ /\ A^2 + S^2. \qquad (4.10)$$

This expression is a maximum with respect A when A = S. Therefore, at the input to the processor, the reference signal power should be made equal to the average power of the preprocessed radar return signal. The optimum signal-to-bias ratio is therefore given by:

$$(s/b)_{opt} = \sigma_{max}GH_m \ /\ 2S = RGH_m \ /\ 2(M)^{1/2}. \qquad (4.11)$$

From Eq. 4.7 we can now write an expression for the dynamic range achievable:

$$D = D_o \ /\ (\ 1 + 2(M)^{1/2}/RGH_m). \qquad (4.12)$$

The dynamic range given by Eq. 4.12 is fully used only

if at least one scattering location has an amplitude of σ_{max} ($= \sigma_{av}R$). This fact suggests that the gains of the input signals should be controlled to meet this condition, in addition to the optimum s/b condition mentioned earlier. To do this, an AGC circuit, which uses a priori knowledge about the target's scattering statistics and measurements of average radar return power, should be employed at the input to the processor to maximize the dynamic range. If insufficient a priori knowledge about the target is available, then the CCD output can be automatically monitored to count those targets which are saturating the CCD. This information can then be used to automatically adjust the input gains on a frame-by-frame basis.

As shown in Eq. 4.12 the dynamic range of the processor is a strong function of the system fringe visibility and MTF, as well as the target characteristics M and R. In fact, in the limit of large M, the dynamic range becomes directly proportional to both the fringe visibility and MTF.

4.3.3 Optical Power Requirements

The dynamic range given by Eq. 4.12 is achievable only if the light source has sufficient power to just saturate the CCD (fill the potential well) at the location of the strongest scatterer. In the worst case we require that the source provide enough light during the imaging operation to saturate all pixels on the CCD array. The number of

photons/pixel needed from the source to fill the potential wells is:

$$N_{ph} = (N_m - N_d)/\eta_q\eta_d\eta_o\eta_m, \qquad (4.13)$$

where: η_q is the quantum efficiency of photogeneration for the CCD at the wavelength of the source; η_d is the average diffraction efficiency of the AO cell for the input electronic levels used; η_o is the overall optical efficiency of the processor and includes losses due to reflection, scattering from the lenses, as well as the losses due to those optical rays which fall outside the lens, mask, and CCD apertures; η_m is the average intensity transmittance of the mask. The peak power required from the source to fill the well at each pixel is thus:

$$P = (p/N)(N_{ph}hc/\lambda\tau_p), \qquad (4.14)$$

where: p is the total number of pixels in the array, hc/λ is energy per photon, and τ_p is the period of the laser diode pulse. The following is a list of parameters typical of our experimental processor:

$N_m - N_d$	150,000 electrons
η_q	.48
η_d	.1
η_o	.5
η_m	.5
τ_p	30 nsec.
λ	.83 μm
p	512 x 320
N	512

With these parameters the required peak power of the laser diode is ~ 32 milliwatts. This power output is achievable with the single mode Hitachi laser diode we used.

4.3.4 Measurement of the Coherence Properties of Pulsed Laser Diodes

When laser diodes are pulsed or modulated the spectral purity of the radiation is reduced from that achievable under cw operation and the temporal coherence decreases accordingly. Understanding the coherence properties of the laser diode source is the first step in determining the fringe visibility of the processor. In this section we report the results of a study to characterize the phenomena which degrade the coherence of single mode LDs under pulsed operation.

A primary factor affecting the coherence of pulsed LDs is the rise in temperature of the junction area during the pulse due to Ohmic heating [16]. This effect causes a change in the lasing wavelength and therefore degrades the temporal coherence. Analytical models for this behavior, based on the thermodynamic properties of the LD structure [17,18], are in good agreement with measured results [19,20]. Other phenomena which affect the temporal coherence of pulsed LDs include the coherence time of the LD and mode-hopping.

We define the coherence time of the LD as the time after the onset of laser oscillation in which the LD changes from its initial multimode operation to a single lasing

mode. The coherence time sets a lower bound on the pulse width, since the coherence time must be a negligible portion of the pulse width to obtain coherence. After single mode operation has been established, the stability of the laser mode is affected by junction heating, which leads to a continuous change in the lasing wavelength throughout the duration of the pulse and intra-pulse mode hopping which leads to a discontinuous change in wavelength. When used in a time integrating interferometric system, such as the SAR processor, where many pulses are integrated, the pulse-to-pulse, or inter-pulse mode stability is also important. If the laser does not consistently select the same mode in which to oscillate for every pulse, then the coherence will be degraded.

Most of the measurements were made on the Hitachi HLP-1600 laser. Measurements were also made on the Mitsubishi ML-3001 and RCA C86030E LDs for comparison. Unless otherwise stated, the data presented herein are for the Hitachi device.

The pulsed LD coherence measurement set-up is shown schematically in Fig. 4.12. The set-up is a Michelson interferometer consisting of mirrors M1 and M2 and the beam splitter B1. Mirror M1 is mounted on a micrometer stage to allow variations in optical path length (OPD) from 0 to 5 cm. Mirror M2 is mounted on a piezoelectric translator to allow convenient monitoring of the fringe depth at the

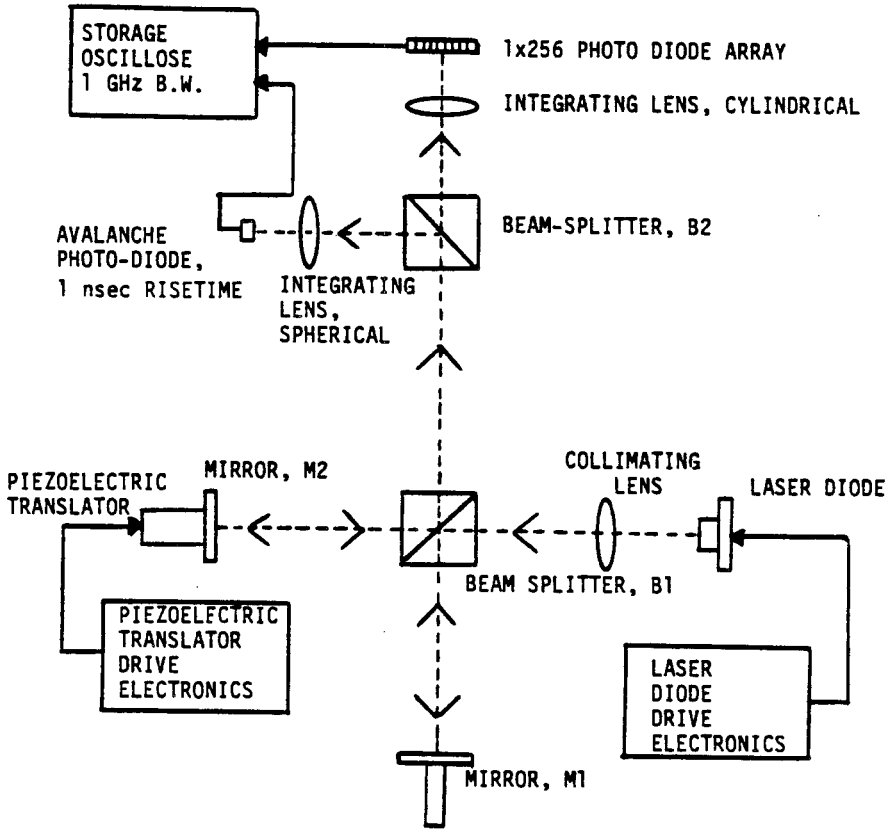

Figure 4.12. Laser diode temporal coherence measurement experimental set-up.

output of the interferometer. The laser drive electronics consists of a current pulser with variable rise time and DC biasing capability.

The light at the output of the interferometer is detected by a high-speed avalanche photodiode (APD) and, independently, by an integrating linear photodiode array (PDA). Beam splitter B2 permits simultaneous data collection with the two types of detectors. The APD that

was used is capable of measuring rise times of 1 nanosecond. The PDA temporally integrates the interferometrically detected light of many sequential pulses in order to characterize the pulse-to-pulse coherence of the LD. When data is being taken with the PDA the two output beams of the interferometer are slightly misaligned along the dimension of the PDA by tilting mirror M1. This produces a linear fringe pattern on the array and the fringe visibility of the interference pattern that is observed on the array is a measure of the coherence over many pulses.

The coherence time is estimated by measuring the time from the beginning of detectable light intensity to the time of maximum fringe visibility. This is accomplished by modulating the OPD with mirror M2 by $\pm\lambda/2$ at approximately 1 Khz with the piezoelectric translator. When many individual pulses are simultaneously displayed on the screen of the oscilloscope the persistence of the screen's phosphor causes the trace to smear due to the varying relative phase between the interfering beams. An example of this is shown in Fig. 4.13a for a 50 nanosecond pulse. Fig. 413b is the interferometer's output when either arm of is interferometer is covered. The overall fringe visibility is directly measurable with this method. For large enough OPDs this smearing occurs only when the laser is oscillating in a single longitudinal mode. During the start up period of the pulse, the light is incoherent, and thus the trace of many

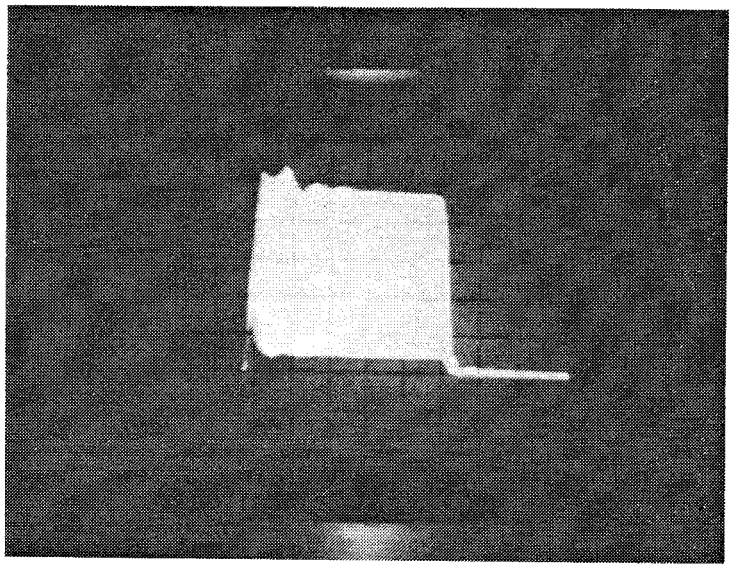

(a) both mirrors uncovered

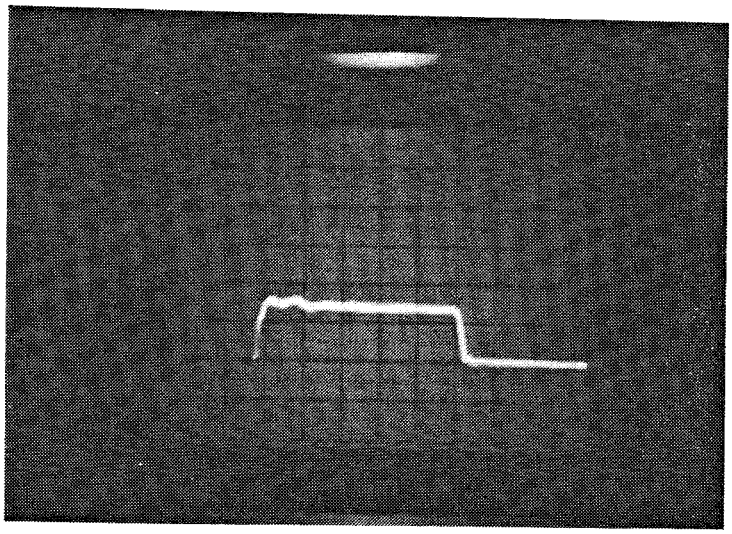

(b) Mirror M1 or M2 covered

Figure 4.13. Interferometer outputs for 50 nanosecond pulse, OPD~1 cm +/- λ/2 at 1 KHz.

pulses appears as a single line. The coherence time is approximately the difference between the time light is first detected as a single trace and the time of maximum smearing due to interference.

Fig. 4.14 shows the interferometric activity at the leading edge of the laser pulse. The first 8 nanoseconds of a 50 nanosecond pulse with 15 mW peak power are shown. The OPD for the data of Figure 4.14 was 1 cm and the time scale of the displayed data is 1 ns/div. Since the envelope of the trace in Fig. 4.14 is a measure of the modulation depth of the interference, it provides an estimate of the coherence time. The coherence time in Fig. 4.14 is measured to be approximately equal to 1.5 nanoseconds. Pre-biasing the laser to a DC level just below the threshold current of the laser reduces the coherence time slightly but not sufficiently to allow accurate measurements of the effect at the short (sub-nanosecond) time scale involved.

The coherence time of the Mitsubishi and RCA LDs were also measured. These lasers have comparable coherence times to the Hitachi LD. At large peak power (>35mW), however, the coherence time for the RCA LD became dramatically longer. In this case, the shape of the interferometrically detected light pulse indicated that two or more competing modes continued to oscillate simultaneously for periods of up to 50 nanoseconds before one became dominant.

To summarize the coherence time measurements, it was

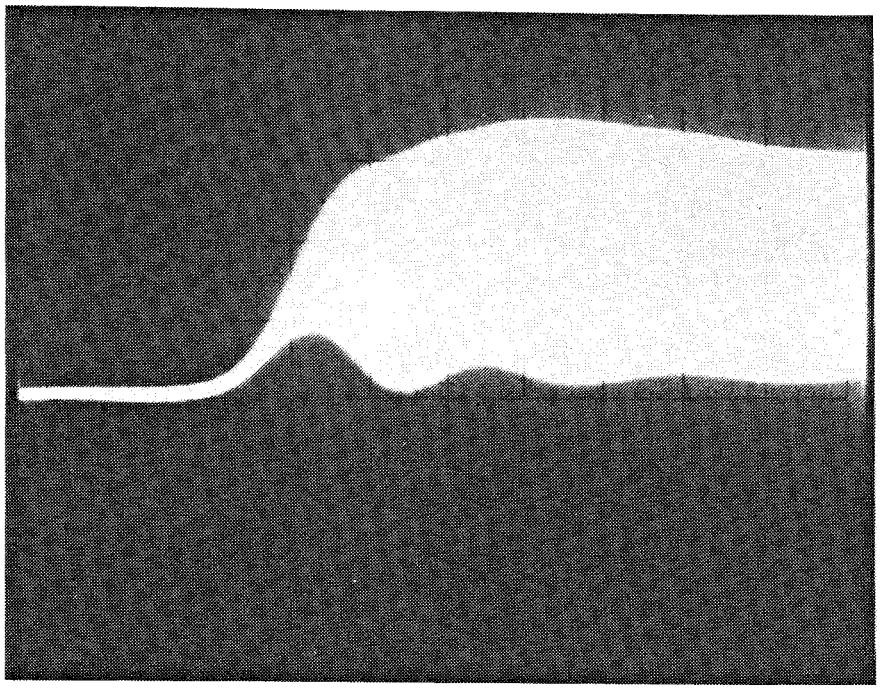

Figure 4.14. Coherence time measurement.

found that the coherence time of the single mode lasers we tested was between 1 and 2 nanoseconds. Therefore, if the laser pulse is much longer than 2 nanoseconds the coherence time will not significantly affect the coherence properties of the laser. For example if 50 nanosecond pulses are used, the laser will be oscillating in a single mode 96 to 98% of the time.

The intra-pulse stability of the lasing mode is measured by studying the trace of the output of the APD for a single pulse of light from the interferometer with mirror M2 kept stationary. Changes in the lasing wavelength during the pulse are monitored as intensity variations of the

interferometrically detected waveform.

Two distinct types of intra-pulse instabilities were observed. The first is attributed to the junction heating during the pulse, causing a continuous shift in the lasing wavelength with time. The second phenomenon affecting the intra-pulse stability is mode hopping in which the laser changes between two adjacent longitudinal modes during the pulse. Both phenomena were observed and characterized.

The effect of a continuous shift in the lasing wavelength on the interferometrically detected signal is shown in Fig. 4.15. In this figure we show oscilloscope traces of the output of the APD for individual laser pulses under 4 different sets of operating conditions. The duration of the pulses in Fig. 4.15 is 2 microseconds. The OPD for these measurements was 4 cm. The pulsewidth and OPD were chosen so that the interferometric effects could be observed over a wide range of operating conditions. It is noted that the frequency of the intensity modulation is highest in the early part of the pulse and seems to asymtotically go to zero.

To explain the observations we must first understand how the laser wavelength changes with junction temperature. The wavelength of a single longitudinal mode laser is given by the following:

$$\lambda=2n_cL/q, \qquad (4.12)$$

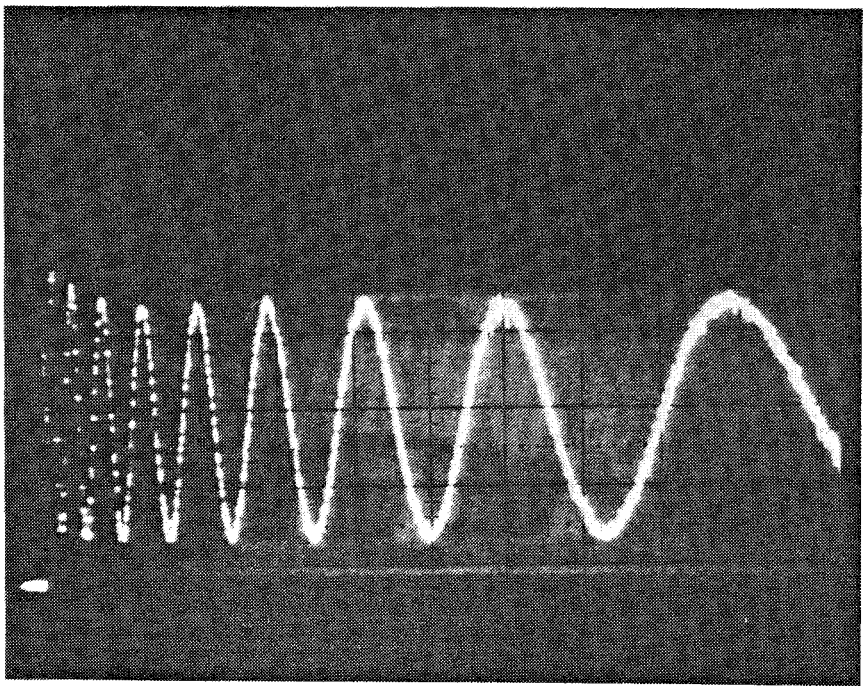

(a)

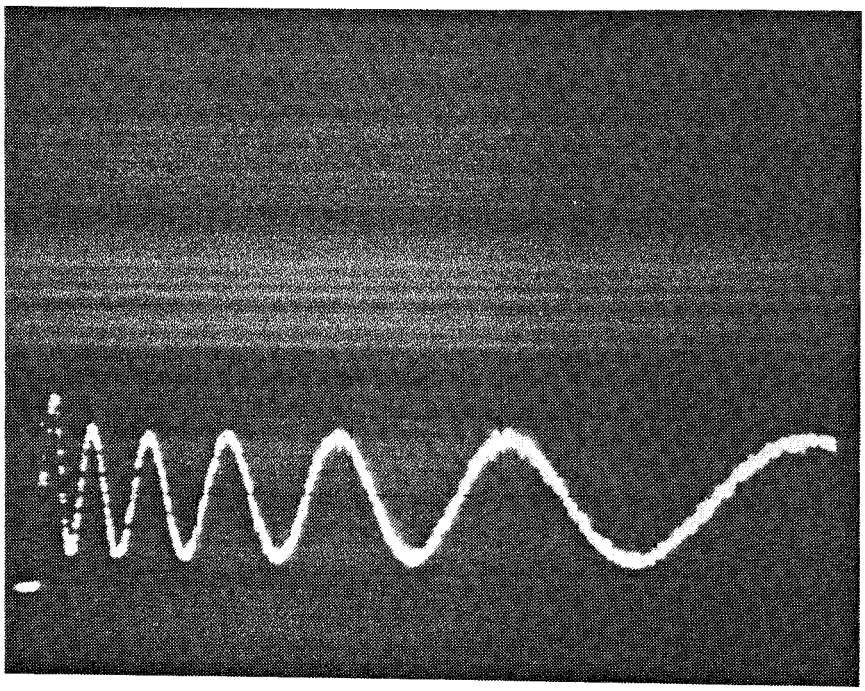

(b)

Figure 4.15. Relative rise in junction temperature for different operating conditions.

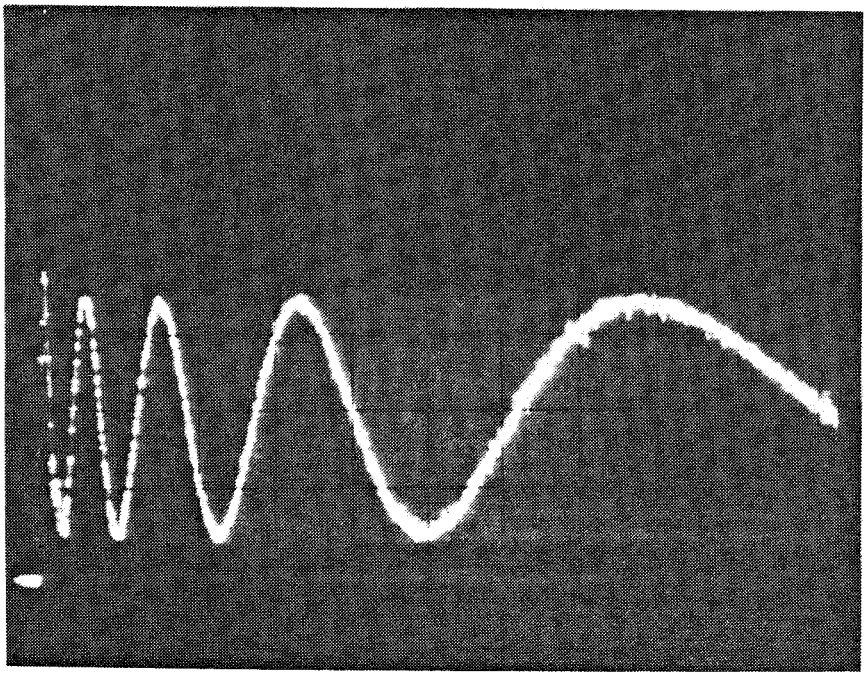

(c)

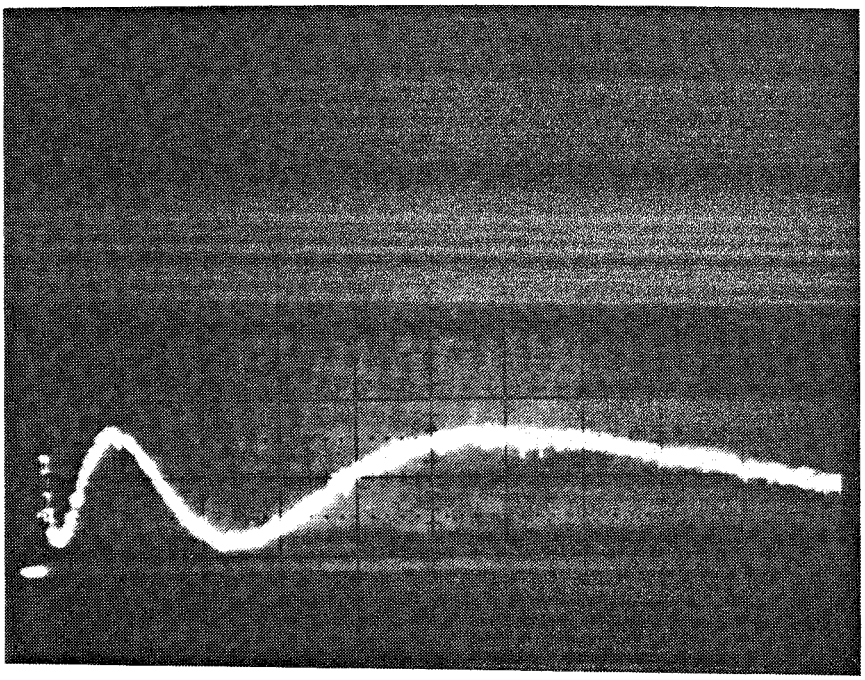

(d)

Figure 4.15. (continued)

where λ is the wavelength, L is the length of the cavity, n_c is the index of refraction and q is an integer. The change in wavelength with temperature is then given by:

$$\lambda' = d\lambda/dT = 2/q(n_c dL/dT + dn_c/dT), \qquad (4.13)$$

For small variations about room temperature, λ' is approximately constant. The HlP-1600 has a measured λ' of 0.06 $nm/^oK$[21].

The detected intensity due to the interference of the two beams is proportional to the cosine of the phase difference, $\Delta\beta$, of the waves:

$$\Delta\beta = 2\pi d/\lambda, \qquad (4.14)$$

where d is the OPD. The change in phase difference with changing λ is then given by:

$$d(\Delta\beta)/d\lambda = -2\pi d/\lambda^2. \qquad (4.15)$$

We multiply Eq. 4.15 by λ' to determine the effect of the temperature change on the phase difference measured with the interferometer:

$$d(\Delta\beta)/dT \simeq -2\pi d\lambda'/\lambda^2. \qquad (4.16)$$

The change in junction temperature during the beginning of laser oscillation has been modeled as follows [17]:

$$\Delta T(t) = T_o(1-e^{-t/\tau}), \qquad (4.17)$$

where T_o is the asymptotic value of the junction temperature change, and τ is the thermal time constant which is determined by the thermal resistance and capacitance of the junction. By integrating Eq. 4.16 and substituting in equation Eq. 4.17 the following expression for the phase difference as a function of time is obtained:

$$\Delta\beta(t) = 2\pi d T_o \lambda' (1-e^{-t/\tau})/\lambda^2 \qquad (4.18)$$

The effects of operating conditions on the mode stability are evident in Fig. 4.15. Figs. 4.15a and 4.15b show the interferometer output for laser peak output power of 15 and 8 milliwatts, respectively, without DC biasing. The smaller number of cycles in Fig. 4.15b indicates a lower rate of change of temperature. Figs. 4.15c and 4.15d show the effect of pre-biasing the laser at its threshold current level, for 15 and 8 milliwatts peak laser intensity, respectively. The significant reduction in the number of cycles observed, is attributed to the fact that pre-biasing raises the temperature of the laser, and the subsequent change in temperature during the pulse is reduced.

The change in junction temperature is plotted in Fig. 4.16 as a function of time from the data in Fig. 4.15. The phase of the amplitude modulation is used as a measure of the change in junction temperature with time. The data clearly show that the temperature rise is exponential in nature and is a close match to the model of Eq. 4.17 with

time constants that are on the order of several hundred nanoseconds.

The rates of wavelength shift of the RCA and Hitachi LDs were compared at an output power of 20 milliwatts for 100 nanosecound pulse widths. It was found that the wavelength of the RCA LD shifted at approximately one half the rate of the Hitachi LD. This effect is probably due to the larger optical cavity of the RCA device which leads to a longer thermal time constant.

Mode hopping is the second type of intra-pulse mode instability that was observed. This phenomenon manifests itself as a discontinuity in the intensity measured at the output of the interferometer. Fig. 4.17 illustrates the effect of an intrapulse mode hop. The OPD and pulse width were chosen sufficiently large so that the effect of the junction heating is clearly observed as well as the intra-pulse mode hop. The pulse width in Fig. 4.17 is 800 nanoseconds and the OPD is 4 cm. At this particular OPD the sudden change in mode, during, the pulse manifests itself as a step change in the phase of the intensity modulation of approximately 180 degrees indicating that the OPD is close to a value which is an integral number of $\lambda^2/2(\delta\lambda)$, where $\delta\lambda$ is the intermode spacing of the laser.

In general, the probability of occurrence of an intra-pulse mode hop increases at higher pulse amplitude and longer pulse widths. For the Hitachi LD it was found that

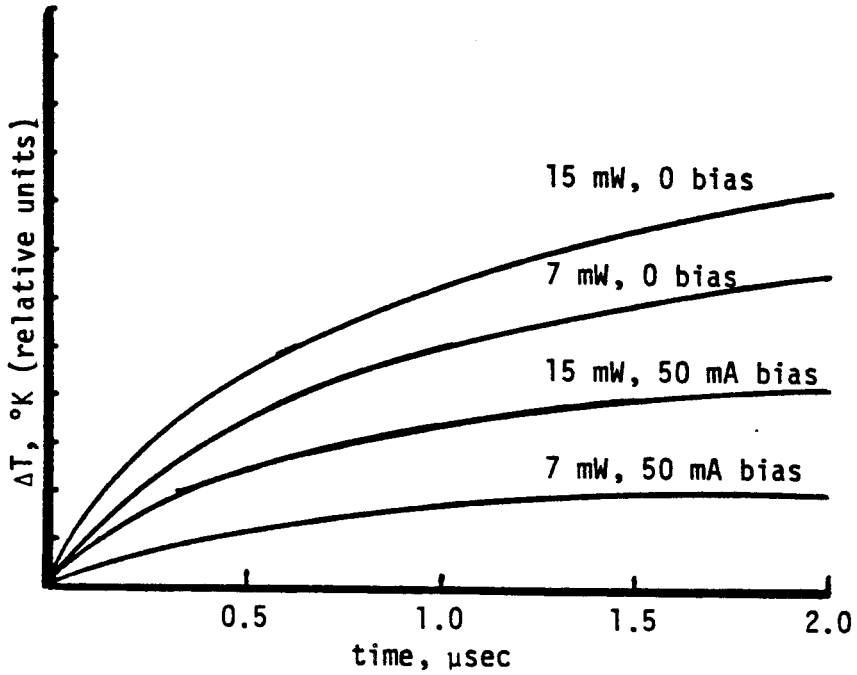

Figure 4.16. Measured change in junction temperature.

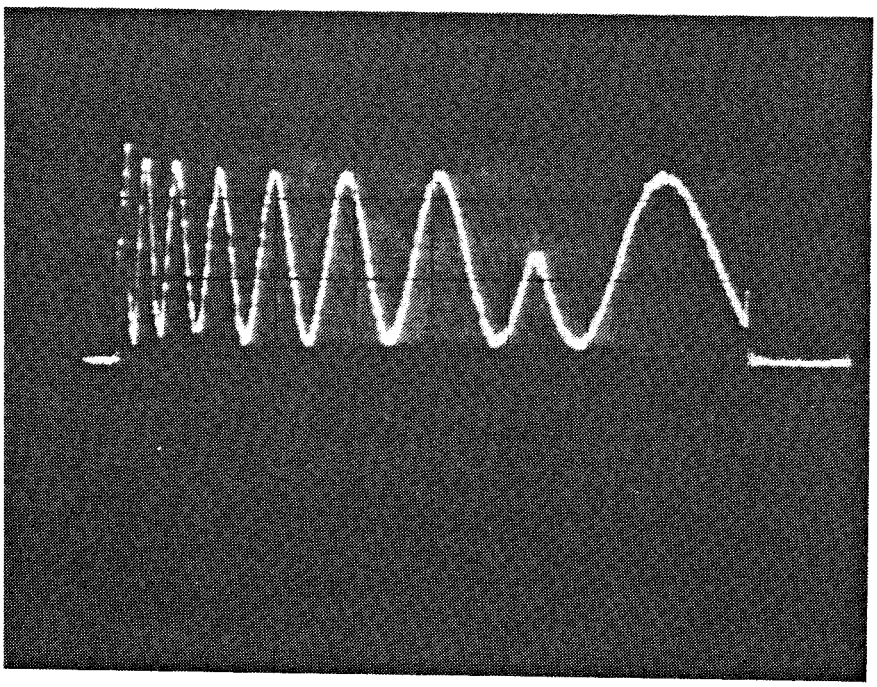

Figure 4.17. Intra-pulse mode hop.

for a pulse width of 50 nanoseconds, the frequency of intra-pulse mode hops is less than 1/40 for a peak power level of 12 milliwatts or less. The RCA LD, at 12 milliwatts, was found to have about twice the rate of mode hopping of the Hitachi LD.

The rates of mode hopping given above are averaged. The actual mode hopping rates varied significantly from measurement to measurement. Intra-pulse mode hopping occurs because the positions of the modes shift in relation to the gain curve of the laser as the temperature of the junction region rises during the pulse. If the shift is large enough, an adjacent mode will move closer to the center of the gain curve than the current lasing mode and will take over. Slight changes in the ambient temperature of the laser's heat sink will also manifest themselves as shifts in the modes' position relative to the laser's gain curve thereby changing the mode hopping rate and/or the position within the pulse at which the mode hop occurs.

Inter-pulse instabilities occur when, over a long sequence of pulses, the laser does not always choose the same mode in which to oscillate. This effect was also characterized in the experimental set-up of Fig. 4.12. The pulse repetition frequency was set at 20 Khz and the pulse width at 50 nanoseconds. The OPD for this data was 1mm and the peak power of the LD 10 milliwatts. Under the stated operating conditions intrapulse mode hopping is neglible.

Furthurmore the change in the phase difference between the interfering beams due to junction heating is small enough so that the resulting output can be considered a sampled version of the cw case. The OPD was modulated by $\pm\lambda/2$ at a frequency of 1 Khz. Modulating the OPD in this manner reveals the fringe depth of the interfering beams. An interpulse mode hop will manifest itself as a discontinuity in the sampled waveform. The output of the APD was monitored on the oscilloscope, and an oscilloscope trace of this measurement is shown in Fig. 4.18. Under the stated operating conditions the intrapulse instabilities do not significantly affect the coherence of the individual pulses. The oscilloscope trace of Fig. 4.18 shows that one mode is dominant but occasionally an adjacent mode is selected. The different modes will, in general, result in different relative phases between the output beams of the interferometer resulting in different detected intensities as shown in Fig. 4.18. It is clear that for time integrating interferometric systems, in which the light from many laser pulses is detected interferometrically and summed, inter-pulse mode hopping could severely degrade the fringe visibility and thus must be minimized.

As with the intra-pulse mode hopping, the rate of inter-pulse mode hops was found to be determined by the electrical operating conditions of the laser. Generally the laser was more stable (a single mode was more likely to

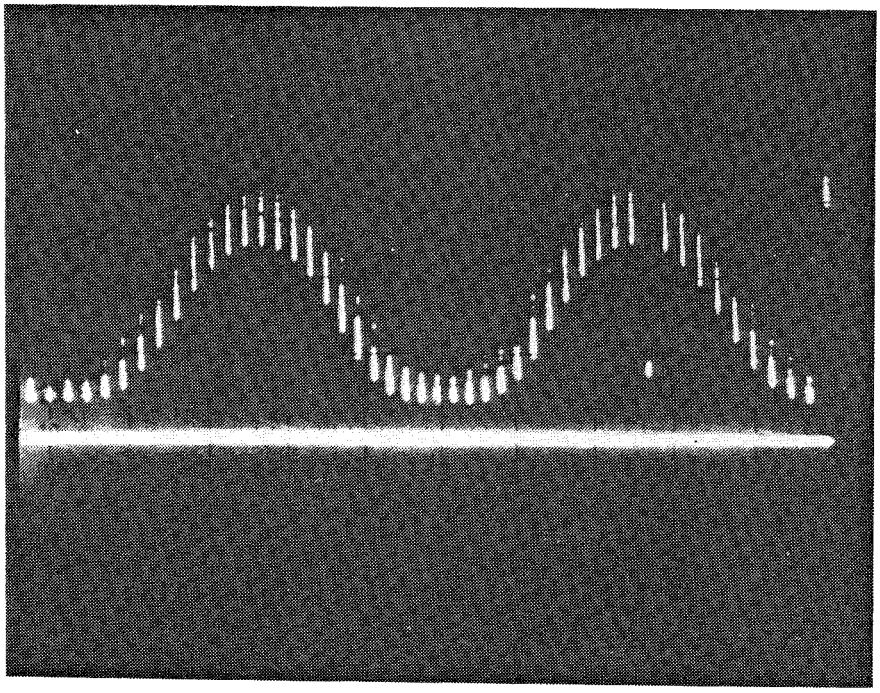

Figure 4.18. Inter-pulse mode hopping.

dominate) at lower peak power levels. This is probably due to the more gradual build up of laser oscillation at the lower drive current levels resulting in more consistent selection of the dominant mode. It was also found that the rate of mode hopping could be significantly reduced by altering the shape of the current drive pulse to have a slower rise time. Measurements of the inter-pulse mode hopping rates were made for different drive pulse shapes and peak power levels. For these measurements the slope of the leading edge of the drive pulses was varied while maintaining the peak level pulse width at approximately 50 nanoseconds. Figs. 4.19a and 4.19b are oscilloscope traces

showing the shapes of typical drive pulses that were compared. For the Hitachi LD it was found that for 10 nanosecond rise times, the inter-pulse mode stability was greater than 95% for peak power levels below 6 milliwatts. However, for drive pulses with rise times of 80 nanoseconds, such as in Fig. 4.19b, the LD exhibited greater than 95% stability for peak power levels up to 12 milliwatts. For rise times greater than 80 nanoseconds no measurable improvement in the inter-pulse mode stability was observed. Furthermore, it was noted that applying a DC bias current to the LD at a level below the threshold current did not significantly affect the inter-pulse stability.

The four types of instability phenomena that were characterized individually in the previous sections (coherence time, junction heating, inter-pulse mode hopping, intra-pulse mode hopping) combine to degrade the fringe visibility in an interferometric system. The relative importance of these instabilities to coherence degradation depends on the operating conditions of the LD and the OPD of the optical system. The effect of the coherence time is minimal if the pulse width of the laser is much greater than the coherence time constant. For the measurements reported here this condition was genereally met and therefore the coherence time was a minor factor. Furthermore, we found that intra-pulse and inter-pulse mode

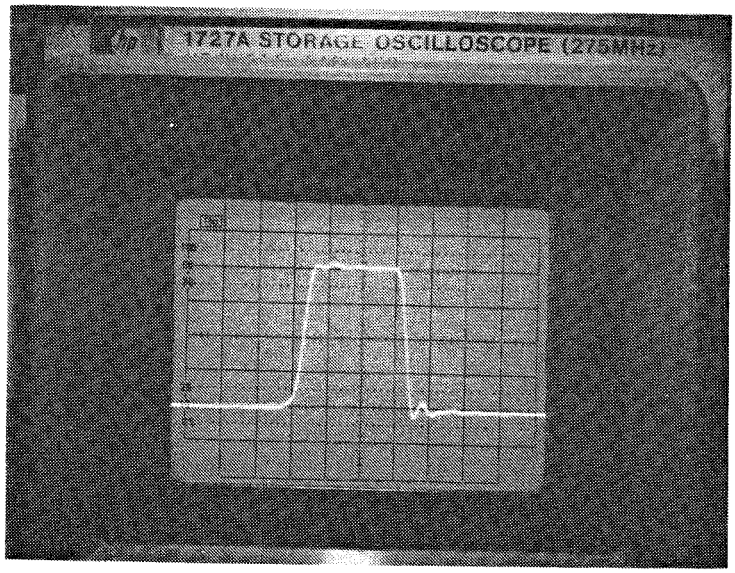

(a) 10 nanosecond rise-time.

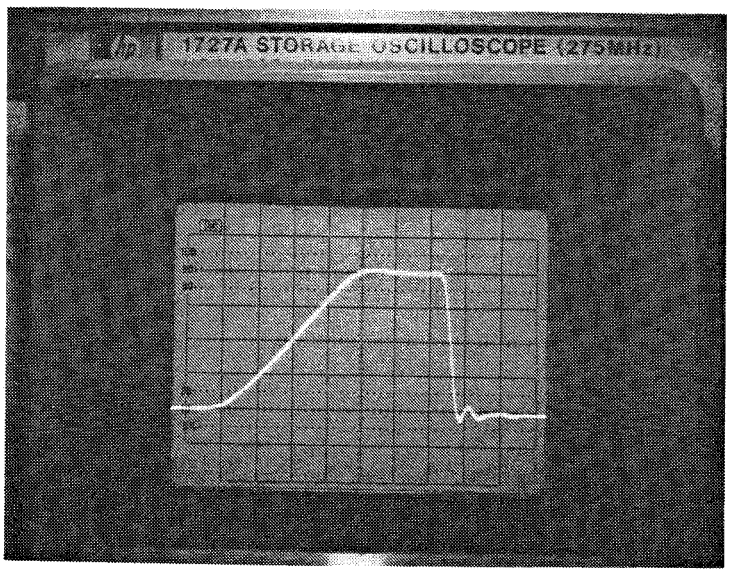

(b) 80 nanosecond rise-time.

Figure 4.19. Laser diode drive pulses.

hopping are minimized by proper choice of operating conditions. For example, with the Hitachi LD at a peak power of 10 milliwatts, the combined intra-pulse and inter-pulse mode hopping occurs at a rate less than 1 mode hop in 20 pulses for a current drive pulse whose shape is similar to that of Fig. 4.19b. The most significant instability is the wavelength shift due to the heating of the junction area during the pulse. To maintain a high degree of coherence for a particular OPD, the pulse width must be such that the intensity measured at the output of the interferometer will fluctuate only a fraction of one of the cycles shown in the examples of Fig. 4.15.

Evaluation of the combined effects of the individual instabilities on the visibility of the interference pattern that results from the integration of many sequential pulses was accomplished by studying the output of the PDA. Fig. 4.20 is an oscilloscope trace of the PDA output. The trace represents the time integrated interferometric response of approximately 10,000 individual laser pulses over a period of 50 milliseconds. The data shown was taken at approximately zero OPD and thus represent the largest attainable fringe depth. In the example of Fig. 4.20 the pulse width is 50 nanoseconds. The actual fringe depth achieved is not 100% because of several non-idealities of the system: the PDA has dark noise which contributes to the bias, the very short multimode portion at the beginning of

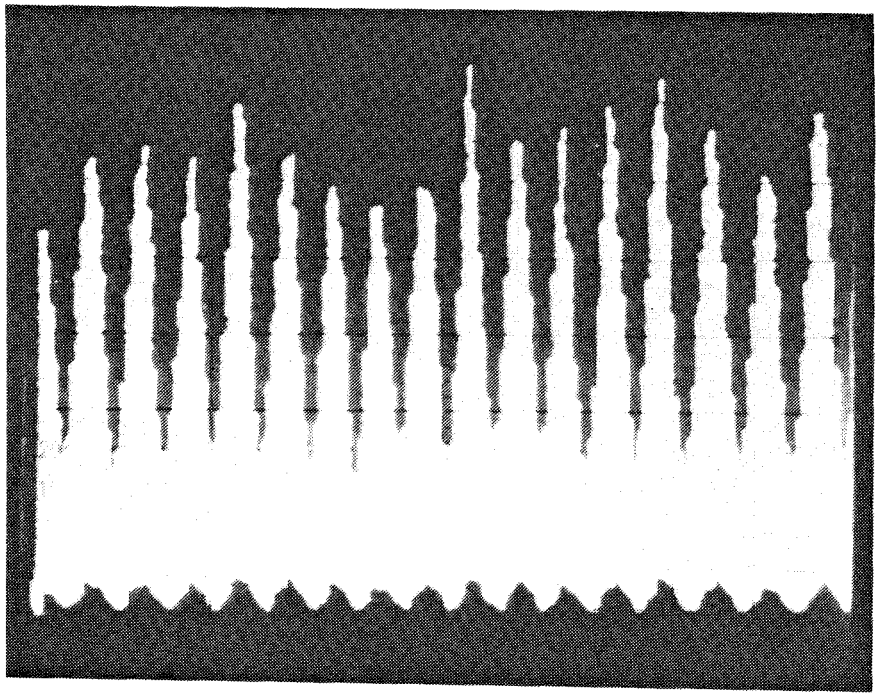

Figure 4.20. Fringe pattern generated by 10,000 interferometrically detected laser pulses.

each pulse adds incoherently to result in a contribution to the bias, and, non-idealities in the measurement set-up, such as misalignment of the integrating lens and signal spreading on the array lead to bias contributions.

A measurement of the fringe visibility, normalized to the maximum fringe visibility obtained at OPD=0, as in Fig. 4.20, provides a direct measurement of the coherence function under different operating conditions. The measured fringe visibility as a function of OPD for different pulse widths is plotted in Fig. 4.21. In this data the effects of mode hopping have been minimized, leaving junction

heating as the primary factor that is responsible for reduced fringe visibility.

4.2.4 Derivation of the Coherence Function of Pulsed Laser Diodes

In this section we derive the coherence function for pulsed laser diodes based on a simple model of the thermodynamic properties of the laser junction. The

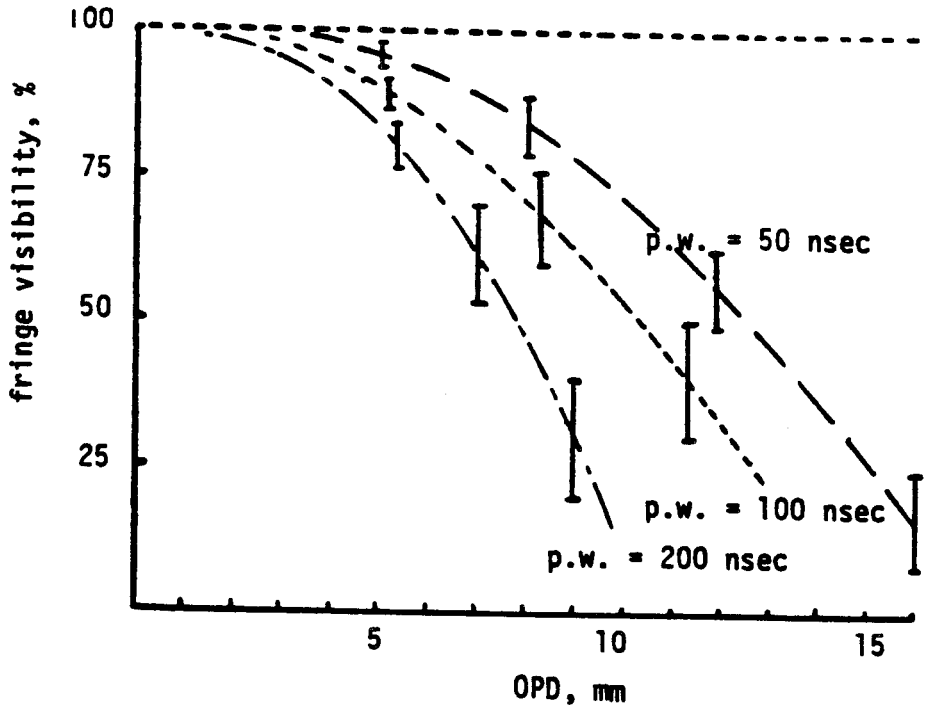

Figure 4.21. Measurements of the modulus of the coherence function.

coherence function analysis is then extended to time integrating systems by including the effect of inter-pulse mode hopping.

The coherence time of a single mode LD has been treated theoretically in the literature [22]. It was predicted that, at moderate to high peak power levels, one longitudinal mode dominates very rapidly (~1 nsec) after the onset of laser oscillation. This is in good agreement with our measurements. The coherence time phenomenon made a neglible contribution to the coherence degradation when the pulse width is very long compared to the coherence time constant. We assume this to be the case and neglect this effect in our analysis. We also ignore intra-pulse mode hopping because it was also neglible under the operating conditions used. Therefore, the dominant phenomena degrading the coherence of the LD are the intra-pulse modal instability due to junction heating and inter-pulse mode hopping.

For a single pulse, the coherence function of the single mode LD is assumed to be determined solely by the junction heating as modeled by Eq. 4.17. This effect is deterministic and therefore, in this case, the coherence function does not involve ensemble averages. The coherence function for multiple pulses, on the other hand, with interpulse modehopping, is stochastic in nature. We will first derive an expression for the effects of junction heating and then add the effects of random inter-pulse mode

hopping.

The optical field at the output of the interferometer is given by:

$$E = e^{j\omega(t)t} + e^{j\omega(t-d/c)(t-d/c)}, \qquad (4.19)$$

where d is the OPD of the interferometer and $\omega(t)$ is the laser's oscillating frequency which changes with time due to the junction heating effect. From Eq. 4.17 the wavelength as a function of time is given by:

$$\lambda(t) = \lambda_i + T_o\lambda'(1-e^{-t/\tau}), \qquad (4.20)$$

where λ_i is the lasing wavelength at the start of the pulse. Since the change in wavelength due to the junction heating is small compared to λ_i we have:

$$\omega(t) = 2\pi c/\lambda(t) \simeq [2\pi c/\lambda_i]\ [1-\lambda' T_o(1-e^{-t/\tau})/\lambda_i]. \qquad (4.21)$$

We now write an expression for the normalized coherence function as a function of the OPD:

$$G(d) = \langle\ e^{j\omega(t)t}\ e^{-j(\omega(t-d/c)(t-d/c))}\ \rangle, \qquad (4.19)$$

where $\langle\ \rangle$ indicates time average over the pulse duration, P. In Eq. 4.22 $\omega(t-d/c)$ is approximated by $\omega(t)$ because -d/c is negligible with respect to τ. We have:

$$G(d) = 1/P \int_0^P e^{j[\omega(t)d/c]}\ dt. \qquad (4.23)$$

Substituting in Eq. 4.21 and using the assumption that $P<<\tau$,

so that $e^{-t/\tau} \sim 1-t/\tau$ on the interval P, then the integration in Eq. 4.23 can be performed in closed form:

$$G(d) \sim \text{sinc}(dc_1P)\ e^{j2\pi[d/\lambda_i - dc_1P/2]} \qquad (4.24)$$

where: $c_1 = \lambda' T_o/\lambda_i^2\tau$ and $\text{sinc}(x)=\sin(\pi x)/\pi x$.

The fringe visibility, V, is defined as the magnitude of the coherence function; hence, for pulse widths much less than the thermal time constant, we have:

$$V = |\text{sinc}(dc_1P)| \qquad (4.25)$$

Eq. 4.25 is plotted in Fig. 4.22 for pulse widths of 50 and 100 nanoseconds. A thermal time constant of 350 nanoseconds is assumed. The measured data (Fig. 4.21) is in good agreement with Fig. 4.22. Note that the effect of a large pulse amplitude on the coherence function would be to increase T_o and hence c_1 in Eq. 4.24, thus leading to lower coherence.

We now analyze the fringe visibility for the case of two competing adjacent longitudinal modes. The two modes have frequency $\omega_1(t)$ and $\omega_2(t) = \omega_1(t)+\delta\omega$ where $\delta\omega$ is the Fabry-Perot mode spacing of the LD's cavity. The time dependence is assumed to be due solely to the junction heating effect. We assign the probabilities of occurrence p and 1-p to the two modes respectively. For any one pulse only one of the two modes exists, and thus the coherence

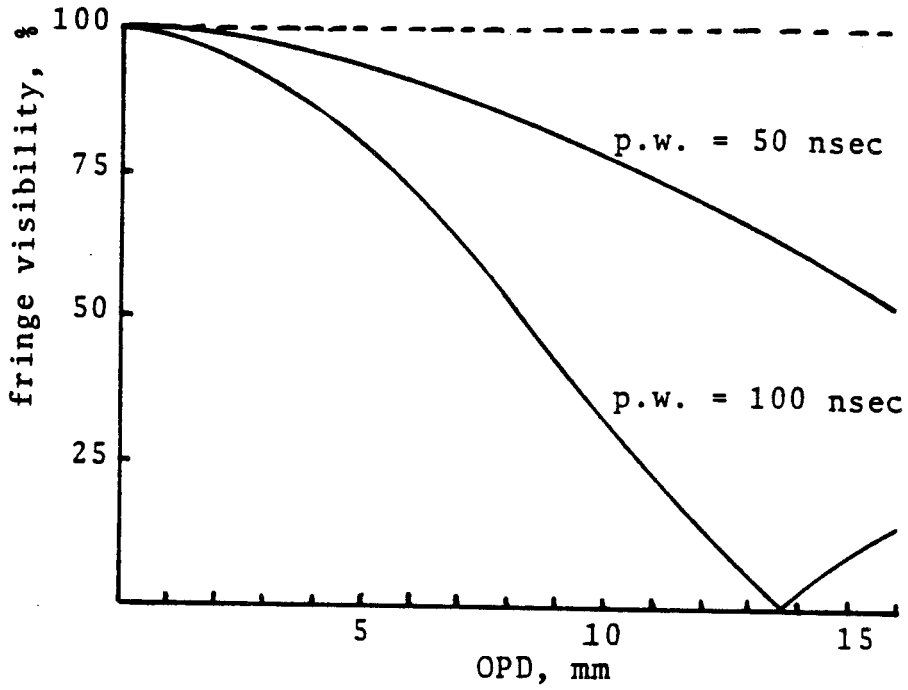

Figure 4.22. Theoretical modulus of the coherence function.

function for multiple time integrated pulses is:

$$G_2(d) = E[\langle e^{j\omega(t)t} e^{-j(\omega(t)(t-d/c))} \rangle]. \qquad (4.26)$$

Using Eq. 4.24 we find:

$$G_2(d) = e^{j[\omega_{1,i} d/c - \pi d c_1 P]} \mathrm{sinc}(dc_1P)[p+(1-p)e^{j(\delta\omega)d/c}], \qquad (4.27)$$

where we have ignored the insignificant differences in the phase term and in the argument of the sinc function for the two modes. $\omega_{1,i}$ and $\omega_{2,i}=\omega_{1,i}+\delta\omega$ are the initial lasing frequencies for the two modes. Hence the fringe visibility

is given by:

$$V_2 = |\mathrm{sinc}(dc_1P)|(2p^2-2p+1+2p(1-p)\cos((\delta\omega)d/c))^{1/2}. \quad (4.28)$$

This function is plotted in Fig. 4.23 for p=0, .1, and .5, for a pulse width of 50 nanoseconds. Fig. 4.23 depicts the degradation in coherence due to the inter-pulse mode hopping instability.

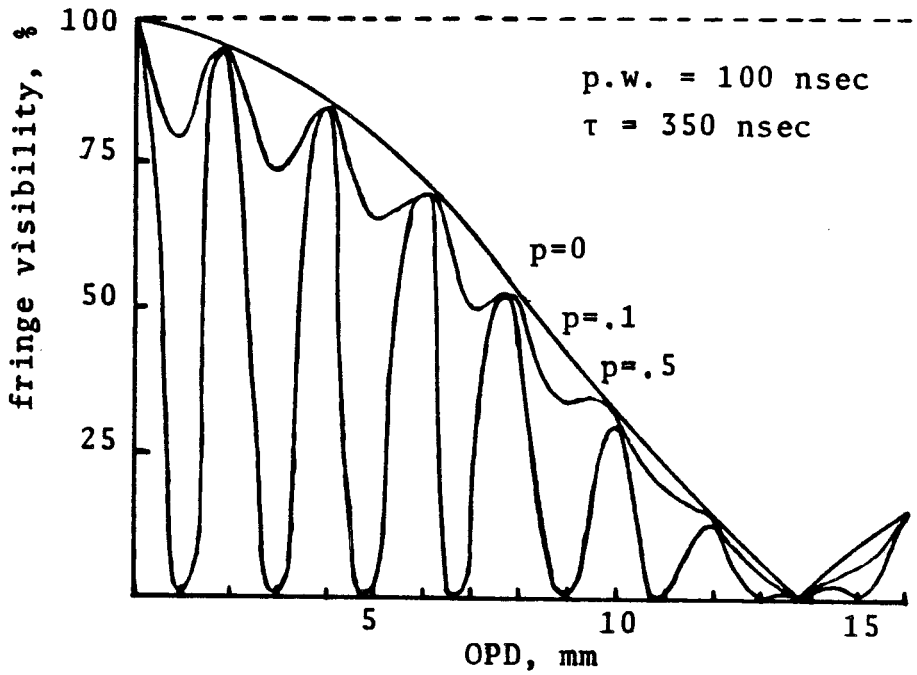

Figure 4.23. Calculated effect of inter-pulse mode hopping on the modulus of the coherence function.

4.3.6 System Coherence Function

The common path interferometric technique, used to detect the azimuth phase history in the processor, is insensitive to mechanical instabilities that would destroy the fringe depth in a multiple path interferometer. However, despite the fact that they pass through common optics and have the same basic path length, the interfering beams are still affected by optical path differences induced by the Bragg diffraction in the AOD. The resulting fringe visibility of the interfering signal and reference light beams is determined by the temporal fringe visibility function of the pulsed laser diode and the combined effect of optical path differences between the interfering light beams.

For this analysis we assume a single mode laser diode source is used, with mode hopping between 2 competing modes with equal probability of occurence, i.e., p = .5 in Eq. 4.28. The fringe visibility function of the pulsed laser diode is therefore given by:

$$V_2 = |\mathrm{sinc}(dc_1P)|(.5 + .5\cos((\delta\omega)d/c))^{1/2}, \qquad (4.29)$$

We wish to determine the fringe visibility at the point of focus on the CCD due to the diffracted, focusing rays of the range chirp in the AOD, interfering with the ray diffracted by the reference sinusoid in the AOD. With the assumption that the reference frequency is selected to be the same as

the center frequency of the radar chirp signal (this is the case in our processor), then the optical path difference, as a function of x (where x is measured along the AOD from the center of the chirped radar return), is given by (see Fig. 4.24):

$$d(x) \simeq 2xz_c + x^2/2f_{ch}, \qquad (4.30)$$

where:

z_c = Bragg angle at the reference frequency

f_{ch} = focal length of the radar chirp in the AOD

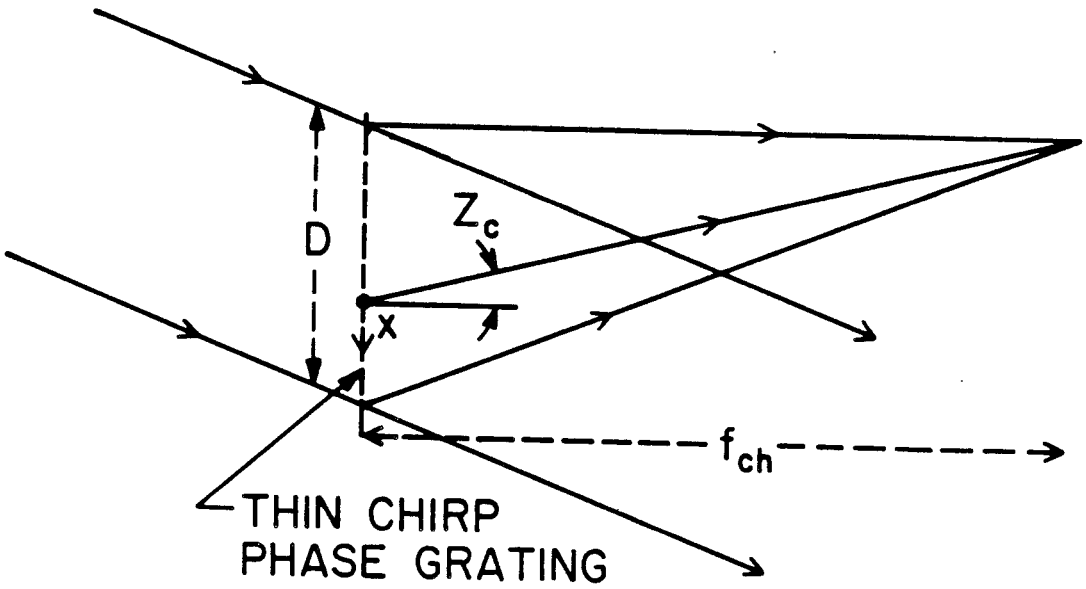

Figure 4.24. Geometrical model for determining OPDs in the SAR Processor.

Eq. 4.30 is based on a geometrical analysis of the rays diffracted by the AOD and the paraxial approximation. For the AO cells used in our experiments the effects of the bulk acousto-optical interaction within the crystal are negligible when compared to the geometrical effects and thus we can treat the AO cell as a thin grating in deriving Eq. 4.30.

By substituting Eq. 4.30 into Eq. 4.29 we obtain the fringe visibility as a function of x. The overall fringe visibility is then given by:

$$\mathbf{V} = 1/D \int V(d(x))dx, \qquad (4.31)$$

where the integration is taken over the width, D, of the range chirp in the AOD. For the single mode laser diode and TeO_2 AOD used in the experimental SAR processor, V(d(x)) is a monotonically decreasing function on either side of x=0, over the integration window, D. We can therefore determine a lower bound on $\mathbf{V}$ without having to evaluate Eq. 4.31 explicitly. The following list of parameters are typical values for the laser diode, AOD, and LFM signal used in the SAR Processor.

λ' = .03 nm/^{o}K
T_o = 5 ^{o}K
P = 50 nsec
λ = .83 nm
τ_o = 350 nsec
$\delta\omega$ = 2π x 130 GHz
D = 3.5 mm
z_c = .041 rad
z_1 = .034 rad
f_{ch} = 11.5 cm

From the above parameters we find that the predicted fringe depth, **V**, is > .98.

4.3.7 MTF Measurements

The MTF of the imager is limited by the CCD detector array. Three phenomena combine to limit the frequency response and hence the overall MTF of the device: integration effects due to the finite pixel size, the spreading of photo-generated charge via diffusion before collection, and the dispersion of charge due to transfer inefficiency. The buried channel structure of the CCD we use provides a transfer efficiency of approximately 0.99999. Thus the transfer efficiency has a negligible effect on the MTF in our case. The MTF due to the pixel geometry is given by the Fourier transform of the responsivity of an individual photo-sensitive site on the array. With the assumptions that the fill factor is 100% and the responsivity is uniform across the pixel, the integration MTF due to the pixel geometry is given by:

$$\text{MTF(integration)} = \frac{\sin \pi f}{\pi f} \qquad (4.32)$$

In Eq. 4.32, f, the spatial frequency, is normalized to the pixel size and has units of cycles/pixel.

If a visible wavelength is used, the MTFs of many commercially available CCDs approach that given by Eq. 4.32. However, for longer wavelengths, the diffusion effect begins

to dominate. This effect is due to the fact that, on average, longer wavelength photons penetrate farther before being absorbed. The resulting photo-generated carriers, are therefore initially located far away from the depletion region of the pixel where they are to be stored. As the charge diffuses toward the depletion region, it spreads, resulting in a decrease in the MTF.

The laser diodes we use have a wavelength of about .84 microns. No data is available of the MTF of the CCD at this wavelength, so we measured the MTF ourselves to ascertain the amount of degradation due to the diffusion of deep carriers. For these measurements we left the CCD in the optical set-up of the SAR processor. This allowed us to get the truest estimate of the actual MTF of the processor. We kept the reference signal but replaced the simulated radar signal with a synchronously generated sinusoid of variable frequency at the input of the AOD. This signal beats with the sinusoidal reference frequency resulting in a 1-D sinusoidal grating pattern on the CCD in the range dimension. The MTF is then determined by varying the difference frequency and measuring the resultant fringe depth on the CCD output. Because the CCD pixels are approximately square, the MTF is assumed to be the same in both dimensions. For these measurements the laser diode was pulsed with a 50 nanosecond pulsewidth at a rate of 20 KHz. The CCD was shifted at a rate of 512 lines per second for a

1 second frame time.

The resulting MTF measurements are shown in Fig. 4.25. Also shown in the figure is the theoretical MTF due to the integration effects of the pixel geometry and the finite laser pulse width. The laser pulse width must be taken into account in the range (horizontal) dimension because the fringe pattern in the AOD is moving. To do this, the line spread function of the CCD (which is the inverse Fourier transform of the MTF) is convolved with a spatial rectangular pulse whose width is given by the product of the laser's pulse width with the acoustic velocity of the AOD. As can be seen in Figure 4.25, the actual MTF is significantly reduced from that predicted by integration effects alone. We believe that the diffusion of deep photo-generated carriers is the dominant phenomenon leading to the data in Figure 4.25. However, other possible contributors to the MTF roll-off include: imperfections in the optics, such as scattering from the AOD crystal, mask, and lenses; imperfect alignment of the CCD and optics; and electronic jitter in the laser diode's trigger pulse.

4.3.8 Side Lobe Effects and Apodization

When two closely spaced point scatterers of different strengths are to be resolved, the dynamic range is limited by the side lobes rather than the noise. We mention it here for completeness. Side-by-side scatterers can be

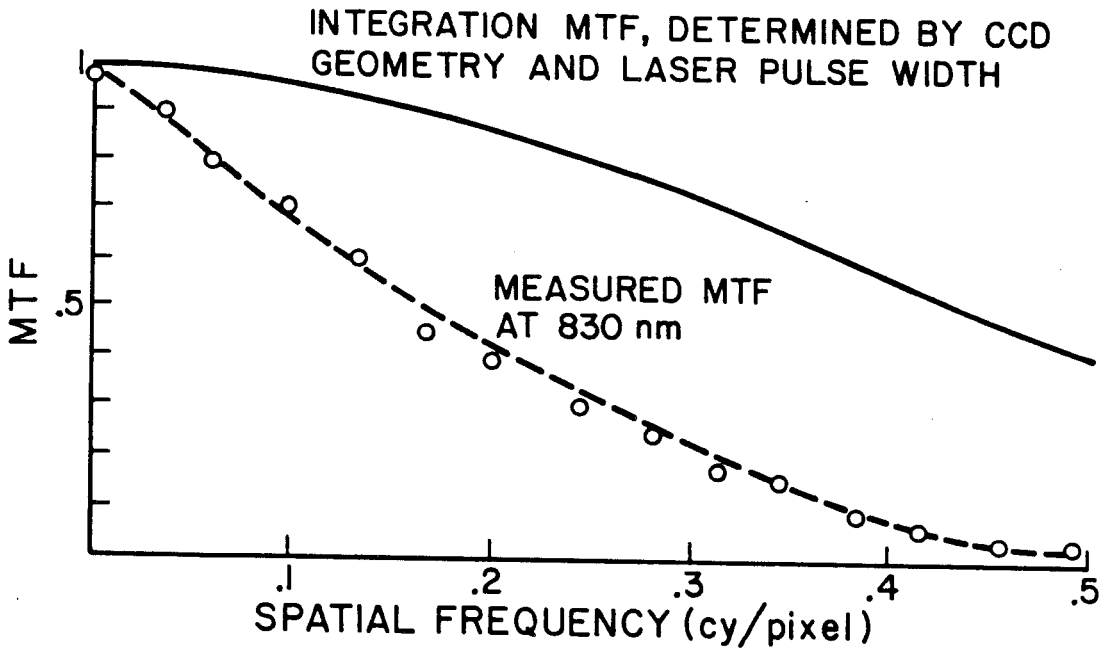

Figure 4.25. MTF Measurements.

differentiated from each other only if the weaker scatterer is higher than the first side lobe of the stronger scatterer. This dynamic range is characteristic of all SAR systems, and if apodization is not used, is limited to approximately 13.5 dB (the peak to side lobe level of a sinc function). In the AO SAR processor the bandpass characteristics of the AOD in the range dimension, and the gaussian beam intensity profile of the laser diode in both the range and azimuth dimensions, have a welcome apodizing effect which reduces the side lobe levels in the focused output (at the expense of some broadening of the central lobe). This effect is evident in the focused data presented

previously, especially in the range focused data.

Fig. 4.26 shows the results of a digital simulation of chirp pulse compression with apodization. The data show the peak and side lobe response of the cross correlation of a symetric baseband LFM signal with three windowed reference functions. The reference functions are symmetric LFM signals with the same chirp rate as the input signal. The first reference function is windowed to have a SBWP of 80. The second reference function is the same as the first, but is multiplied by a gaussian weighting function that falls to e^{-1} at the window's edges. The third reference function tested is weighted with a gaussian function that falls to e^{-2} at the windows edges. The side lobe reduction along with the slight broadening of the central lobe is evident in Fig. 4.26.

4.4 Resolution

4.4.1 Range Resolution

As mentioned in Chapter 2, the theoretical limit to resolution in the range dimension is $\eta_r' = c/2B$, where $B = b\tau$ is the bandwidth of the temporal chirp code. This limit was determined by arbitrarily defining the size of a resolution cell to be 1/2 the width (at the zero crossings) of the compressed range signal. The factor of 2 in η_r' is due to the fact that the scattered radar signal travels a distance equal to twice the actual range difference between 2

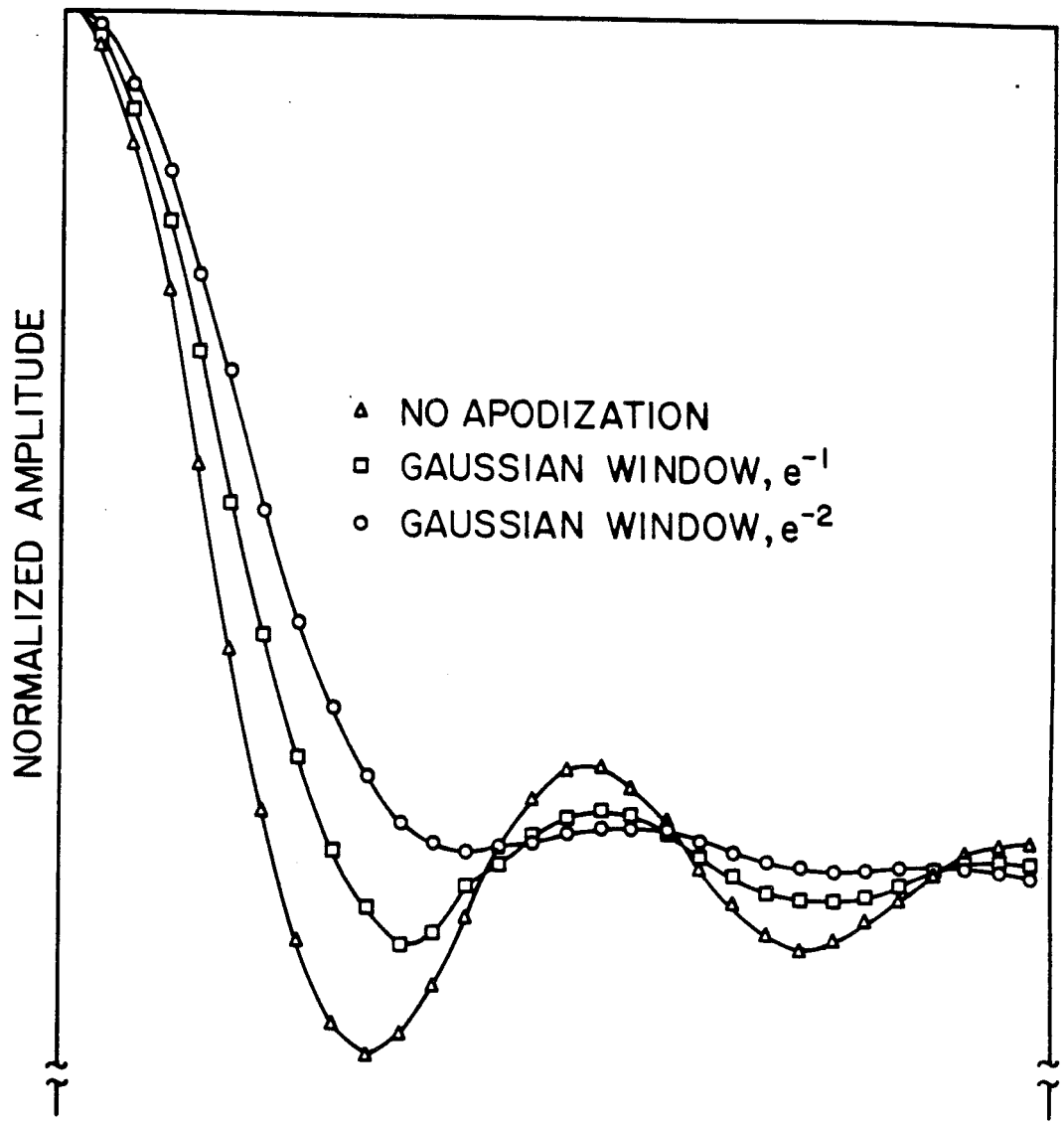

Figure 4.26. Predicted Apodization Effects.

scatterers. Without apodization, the shape of the range compressed signal was shown in Chapter 3 to be a sinc function whose central lobe has a width of $2v_a/B$ (measured at the zero crossings) at the focal plane of the range chirp diffraction grating induced in the AO cell. This optically range compressed signal is identical to the diffraction limited spot that would result from a 1-D lens of aperture $v_a\tau$ and focal length f_{ch}. When translated into the coordinates of the output plane of the SAR processor, the size of a range resolution element is:

$$\eta_r = Mv_a/B_r, \tag{4.33}$$

where M is the magnification of the optical system in the range dimension. We assume that the pixel size in the range dimension, δx, is less than or equal to η_r. To achieve the resolution given by Eq. 4.33 it is obviously necessary for the AO cell to have a time aperture, τ_{ao}, which is greater than or equal to τ. Assuming no apodization, the number of resolvable targets (range bins) that can be fully focused, N_r, is determined by the AO cell's time aperture via: $N_r\eta_r < v_a(\tau_{ao}-\tau)$, or the width of the CCD: $N_r\eta_r < N_x\delta x$, whichever is smallest.

In practice, the width of the range resolution element on the CCD will be wider than that given by Eq. 4.33 due to several phenomena which broaden the compressed signal. The most prominent apodizing features in our processor are the

MTF of the CCD and the movement of the grating in the AO cell during the finite period of the sampling laser pulse. Other effects that will add to the broadening of the range focused signal include: aberration and misalignment in the optics, the finite source size and gaussian beam profile, jitter in the electronic laser diode trigger pulses, and nonuniformities in the bandpass characteristic of the AO cell. The integrated effects of all the phenomena mentioned above are contained in the MTF measurement in Fig. 4.25. The point spread function (PSF) of the system in the range dimension is the Fourier transform of the MTF. The MTF in Fig. 4.25 is well approximated by an exponential function which is readily Fourier transformed into the Lorentzian shaped estimate of the PSF shown in Fig 4.27a. The actual CCD response to the PSF is discretized by integration over the finite pixel widths of the array to yield the predicted PSF response (for the PSF centered on a pixel) shown in Fig. 4.27b. The CCD response to a range focused scatterer is the convolution of the PSF and the diffraction limited range focused signal (sinc function). For our processor, with: $|M|=1$, $f_{ch}=11.5$ cm, $D=.3$ cm, $\lambda = .83$ microns, and $\delta x=30$ microns, the width of the range focused sinc function is approximately 2 pixels. The convolution of this signal with the PSF of Fig. 4.27a yields a result that is essentially identical to the PSF itself. Hence the predicted CCD response for our processor is approximately that shown in

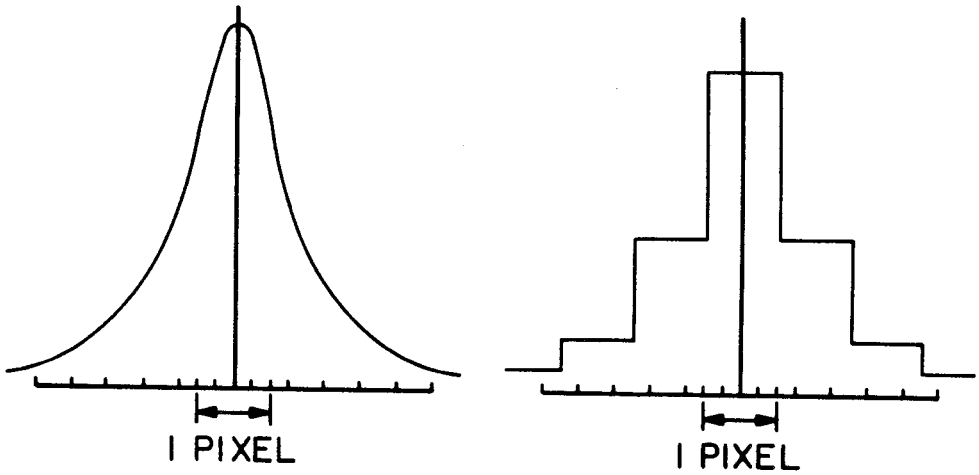

Figure 4.27. Range point spread function predicted from MTF measurements.

Fig. 4.27b. The signal dependent bias ridge consists of the convolution of the PSF and the square of the sinc function described earlier, which is also essentially equal to the PSF. Fig. 4.28 is an example of a portion of the actual CCD output showing the range focused signal. In this data no reference signal was used, yielding only the bias ridge term. The estimated and measured CCD responses, shown in Figs. 4.27b and 4.28 respectively, are in close agreement.

4.4.2 Azimuth resolution

The doppler bandwidth of the signal from a point scatterer in a side-looking SAR geometry (see Fig. 2.1),

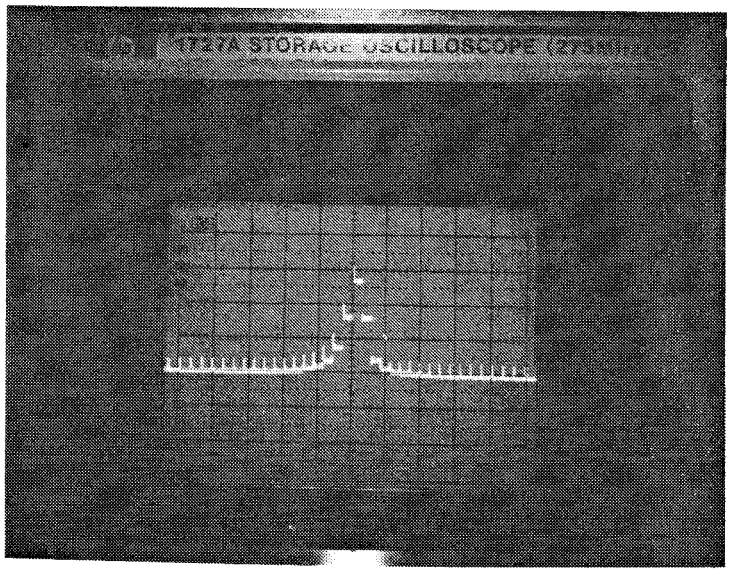

Figure 4.28. CCD response to range focused signal.

with azimuth integration period τ is given by:

$$B_a = \omega_0 v^2 \tau / \pi c R_0, \tag{4.34}$$

where R_0 is the minimum range to the target. The width of an azimuth resolution element, defined similarly to that in the range dimension, is $\eta_a' = v/B_a$. When coordinate transformed into the output plane of the SAR processor, the size of the azimuth resolution element is given by:

$$\eta_a = v_d/B_a, \tag{4.35}$$

where v_d is the apparent velocity of the integrating detector array due to the TDI operation of the CCD in the azimuth directiom. To achieve equal scaling in the x and y coordinates of the image, the parameters of the processor must be chosen such that:

$$\eta_a/\eta_r = \eta_a'/\eta_r'. \qquad (4.36)$$

We assume that the azimuth pixel size, δy, is less than or equal to η_a. To produce the azimuth resolution given by Eq. 4.35 requires that the CCD's integration window in the azimuth dimension be equal to $v_d\tau$. Because the CCD is operated in the TDI mode, at a shift rate equal to the prf, the focused data is continually scrolled out of the processor with no limit on the cross-range (azimuth) extent of the image.

As in the range compression operation, there are several apodizing phenomena in the processor which will broaden the focused azimuth spot. In our experimental implementation the primary apodizing agents are the gaussian beam profile and the MTF of the CCD. (In an actual radar, the shape of the antenna's beam pattern may also play a significant apodizing role.) The half-power beam width of the laser diode we use is approximately 10 degrees. With a 7.5 cm focal length collimating lens and 1.6 cm CCD height, the resulting gaussian intensity profile falls to approximately 1/e of its maximum value at the top and bottom edges of the CCD. In addition, the CCD response to the spatial intensity modulation of the mask, along the azimuth direction, is weighted by the MTF of the CCD at the spatial frequency of the mask at each position. If carrier encoding is used, and the modulating frequency is significantly higher than the bandwidth of the azimuth phase history (as

described in section 4.1), then the MTF is approximately constant over the CCD at the value of the MTF at the carrier frequency. If a bias removal technique is employed which does not use carrier encoding, the apodizing effect of the MTF becomes more significant for signals with higher azimuth bandwidths. At the highest bandwidths the narrowest azimuth spot possible is given by the PSF of the system, in which case the pulse compression ratio becomes constant and independent of the azimuth bandwidth. Fig 4.29 shows the processor response to a simulated scatterer with the relatively low azimuth TBWP of 80. The predicted width of

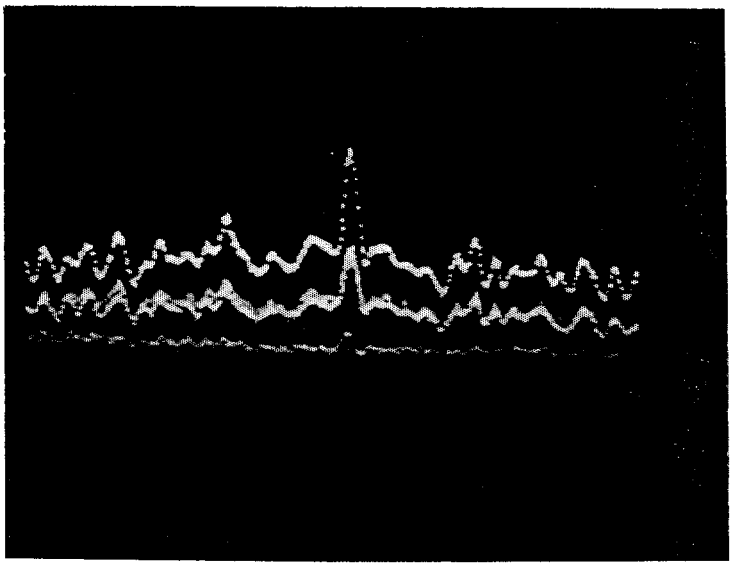

Figure 4.29. Isometric display of azimuth compression, TBWP = 80.

the compressed signal, at the zero crossings, is approximately 13 pixels (512/(80/2)). The pulse width in Fig. 4.29 is approximately 50% greater than this due primarily to the apodization of the gaussiam beam. Fig. 4.30 shows the processor response to a simulated target with an azimuth TBWP of 320. In this case the limiting width of the focused spot is approximately 3 pixels. The data in Fig. 4.30 show that the pulse width is approximately a factor of 2 wider than the limit, and is approaching the narrowest azimuth pulse width achievable with our processor.

Fig. 4.31 shows the highest resolution image of a simulated point scatterer obtained with our experimental processor. In this data the bias has been artificially removed (by adjusting the brightness and contrast controls on the display monitor) and superimposed on a display of the output of the CCD with no illumination. The resulting spot size in Fig. 4.24 is approximately 3 pixels in either direction.

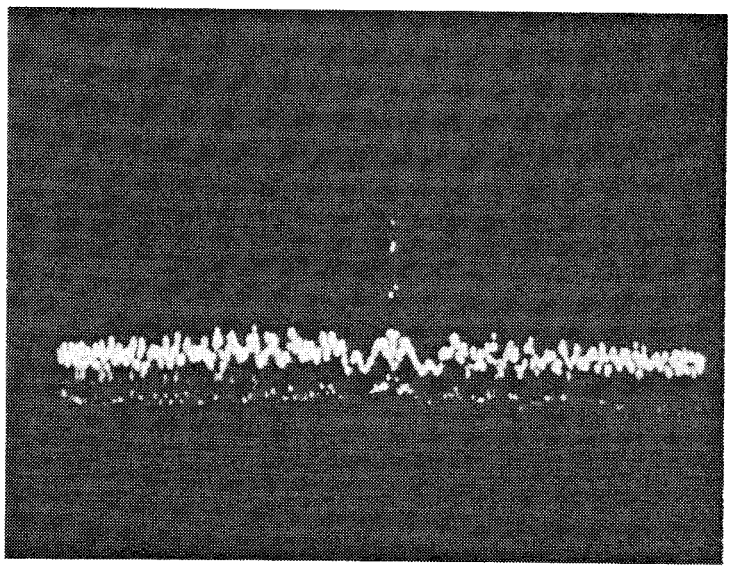

(a) 512 pixels displayed.

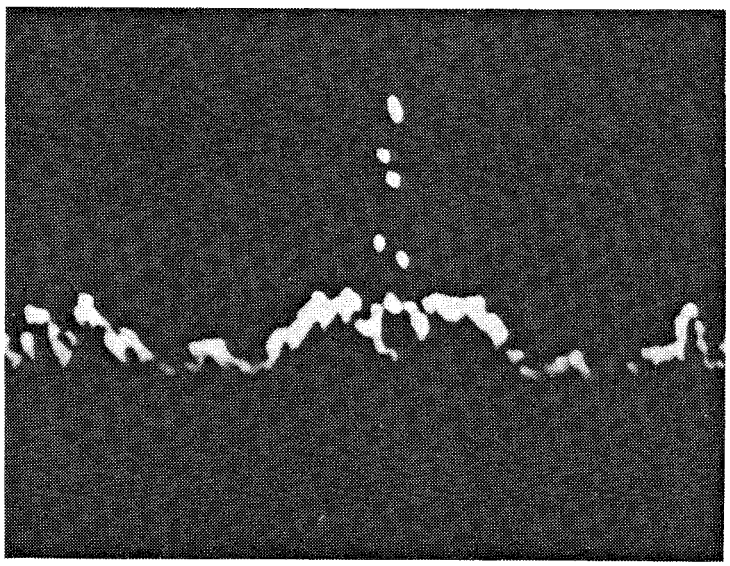

(b) same as (a), magnified.

Figure 4.30. Azimuth compression, TBWP = 320.

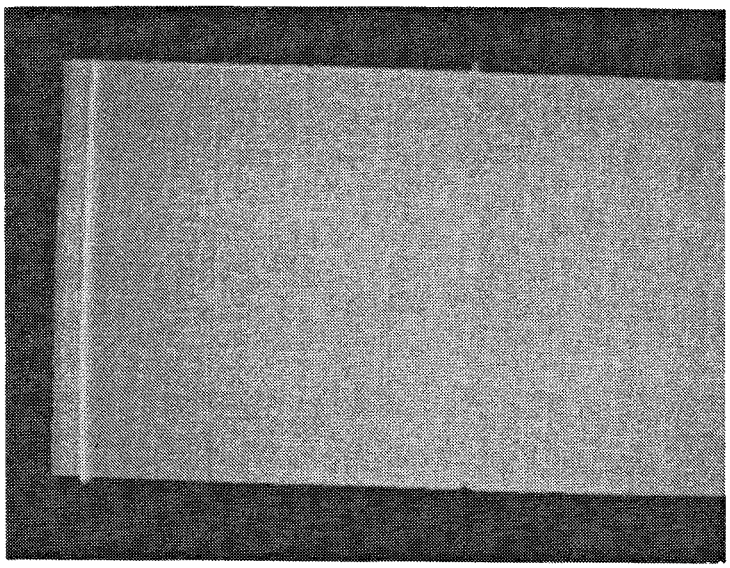

Figure 4.31. Highest resolution image of simulated point scatterer achieved with SAR Processor.

CHAPTER V. COMPENSATION FOR RANGE MIGRATION EFFECTS

5.1 Description of Range Migration

In defining the SAR processing problem in Chapter 2 and describing the SAR processor in Chapter 3 we made simplifying assumptions about the SAR geometry which are not always valid. The most notable of these assumptions was that the ground swath being imaged is located directly to the side of the radar's flight path, i.e., the antenna's pointing vector is normal to the radar's velocity vector. Applications exist, however, in which it is preferable to collect data from a region of the swath located forward of the radar, as depicted in Fig. 5.1. In this chapter we address this and other aspects of the general SAR problem and show how the real-time processor can be adapted to handle them.

Because only 2 parameters (range and azimuth) are measured in SAR, the processing problem can be completely formulated within a 2-D plane geometry without any loss of generality. We use this formulation here to simplify the analysis of range migration. Also, since we are interested in the range and angular positions of the scatterers, a polar coordinate system is more convenient than a rectilinear one. Consider the plane defined by the aircraft's velocity vector and antenna pointing vector in

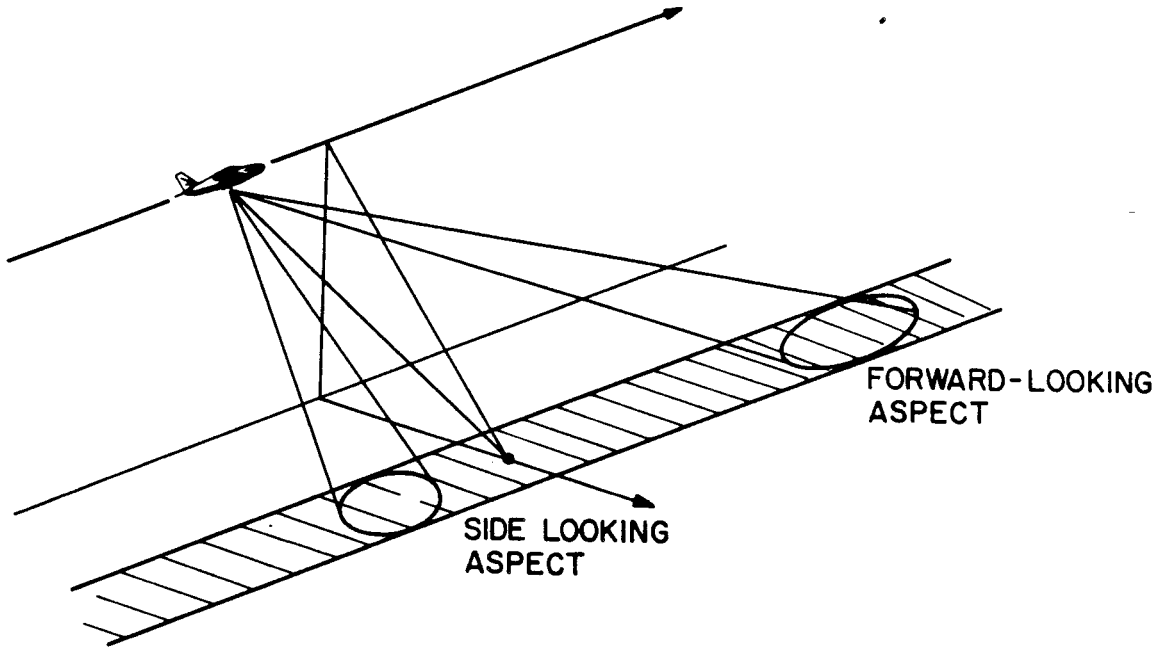

Figure 5.1. SAR Geometries.

Fig. 5.1. In terms of a 2-D geometry, the radar/target geometry is now defined as shown in Fig. 5.2. The coordinates of the point scatterer located at the center of the beam at time (or n) zero are R_o and θ_o. The range to this scatterer, as a function of n, is given by:

$$R(vnT) = (R_o^2 - 2vnTR_o\cos\theta_o + (vnT)^2)^{1/2}. \qquad (5.1)$$

If $vnT \ll R_o$ Eq. 5.1 is approximated well by:

$$R(vnT) \sim R_o - vnT\cos\theta_o + (vnT\sin\theta_o)^2/2R_o. \qquad (5.2)$$

The first assumption that we made earlier was that the radar/target geometry is directly side-looking, i.e., the radial velocity vector between the radar and each scattering

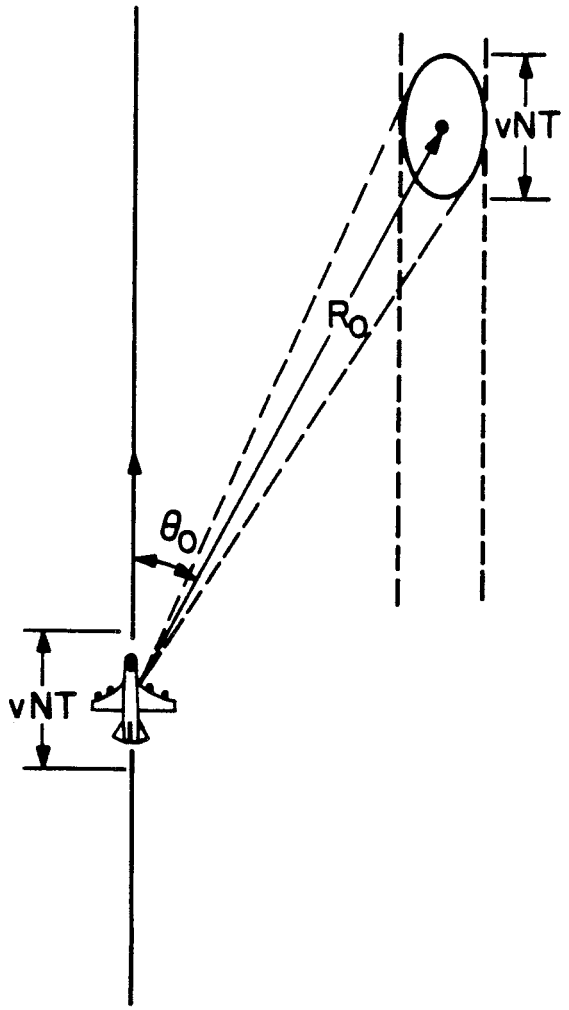

Figure 5.2. 2-D Forward-looking SAR geometry.

site in the target field is zero when averaged over the complete integration period. In this case the squint angle (defined as the angle between the radar velocity vector and the antenna pointing vector) is 90 degrees. In the general SAR problem the radar is centered at a squint angle other than 90 degrees. In this case the average radial velocity, as indicated by the term that is linear in n in Eq. 5.2, is not zero, resulting in movement (in time) of the range focused return signals across range bins in the processor. This phenomenon is known as **range walk** and must be compensated for to achieve a well focused image.

The second assumption made in earlier chapters was that the small pulse-to-pulse range variations, which are responsible for the generation of the azimuth phase history in the side-looking geometry, do not, when added together, produce a range delay variation, over the data collection period, that is large enough to affect the range focusing operation; i.e., the maximum range variation was less than the width of one range resolution element. This is not true in general. The actual range variation has a quadratic component in time (or n) as shown in Eq. 5.2. This effect is known as **range curvature** and must be compensated for if the total azimuth integration period, NT, is long enough to meet the following condition:

$$(NvT\sin\theta_c/2)^2/2R_c > c/2b\tau, \qquad (5.3)$$

This condition is met for those cases where long integration times are used to achieve high azimuth resolution.

Figure 5.3 is a schematic representation of the range/doppler histories of point scatterers in the side- and forward-looking SAR scenarios. In the forward-looking case, both range walk and range curvature are present, while in the side-looking geometry only range curvature occurs. With the prf of the radar equal to 1/T, the figure shows that for azimuth integration periods greater than N'T, Eq. 5.3 is satisfied, and range curvature will blur the range returns across more than one range bin.

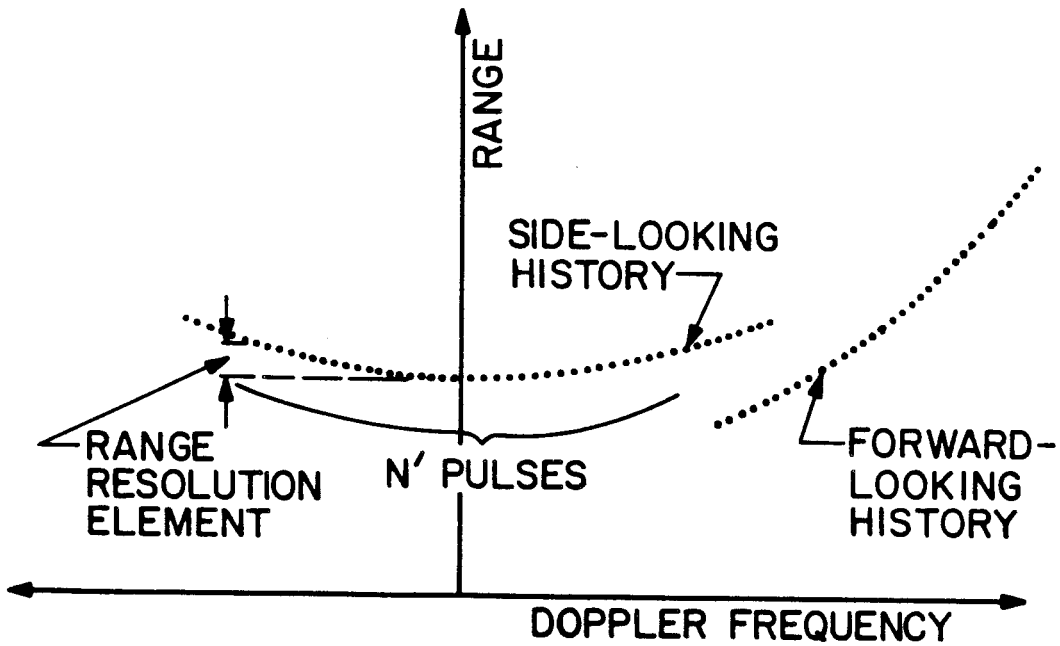

Figure 5.3. Range/Doppler Histories for a point scatterer.

5.2 SAR Signals with Range Migration

Substitution of Eq. 5.2 into Eq. 2.4 results in the general expression for the signal reflected by a point scatterer located at (R_o,θ_o):

$$f(t) \sim \exp(j\omega_o t)$$

$$x \quad \sum_N \text{rect}[(t-2R_o/c+2vnT\cos\theta_o/c-(vnT\sin\theta_o)^2/cR_o-nT)/\tau]$$

$$x \quad \exp(j\pi b(t-2R_o/c+2vnT\cos\theta_o/c-(vnT\sin\theta_o)^2/cR_o-nT)^2$$

$$x \quad \exp(-j(2\omega_o/c)(R_o - vnT\cos\theta_o + (vnT\sin\theta_o)^2/2R_o). \qquad (5.4)$$

We describe the locations of other scatterers in the target field in terms of their range and angular coordinates (ρ,γ), with respect to the point at (R_o,θ_o) at t = 0. The position of an arbitrary scatterer at t = 0 is thus $(R_o+\rho_o,\theta_o+\gamma_o)$. If we assume $\rho_o \ll R_o$ and $\gamma_o \ll \theta_o$, and lump the constant phase terms together, then the return signal from an arbitrary scatterer is given by:

$$f(t) \sim \exp(j\omega_o t) \quad x$$

$$\sum_N \text{rect}[(t-2R_o/c-2\rho_o/c+2vnT\cos\theta_o/c$$
$$-(R_o\gamma_o+vnT\sin\theta_o)^2/R_oc + R_o\gamma_o^2/c-nT)/\tau]$$

$$x \quad \exp[j\pi b(t-2R_o/c-2\rho_o/c+2vnT\cos\theta_o/c$$
$$-(R_o\gamma_o+vnT\sin\theta_o)^2/R_oc + R_o\gamma_o^2/c-nT)^2]$$

$$x \quad \exp[j(2\omega_o/c)\cos\theta_o vnT]$$

$$x \quad \exp[j(\omega_o/cR_o)(1-\rho_o/R_o)(((R_o+\rho_o)\gamma_o) + vnT\sin\theta_o)^2+\mu_o]. \qquad (5.5)$$

Note that if $\theta_o = 90$ degrees, and we neglect range curvature as in Chap. 2, then $\rho_o = x_o$ and $(R_o+\rho_o)\gamma_o \sim y_o$, and Eq. 5.5 reduces to Eq. 2.7 for the case of h = 0 in Fig. 2.1.

In the next section we describe a technique for range curvature correction for the side-looking geometry. A method for range walk correction in the forward-looking geometry is then described along with results of an experimental demonstration of it. Lastly, we describe how both forms of range migration can be compensated simultaneously.

5.3 Range curvature correction

If not compensated for, range curvature leads to a single back-and-forth movement, of the range focused line on the CCD, due to the quadratic term in Eq. 5.5. As a result, the focusing image of a point scatterer, as it is forming on the bias ridge (due to the TDI action), moves in an arch across the CCD, as shown pictorially in Fig. 5.4. Since the pixels on the CCD are arranged in a rectilinear pattern, if the total excursion in range is large enough to involve more than one range bin, then the image will be blurred in both the range and azimuth directions. To compensate for this quadratic range deviation, a barrel distortion of the range focused line on the CCD is induced which cancels the range curvature distortion. This is accomplished by a slight tilt, θ_t, about the y axis, of one of the cylindrical lenses in the system, as shown in Fig. 5.5. If the curvature in

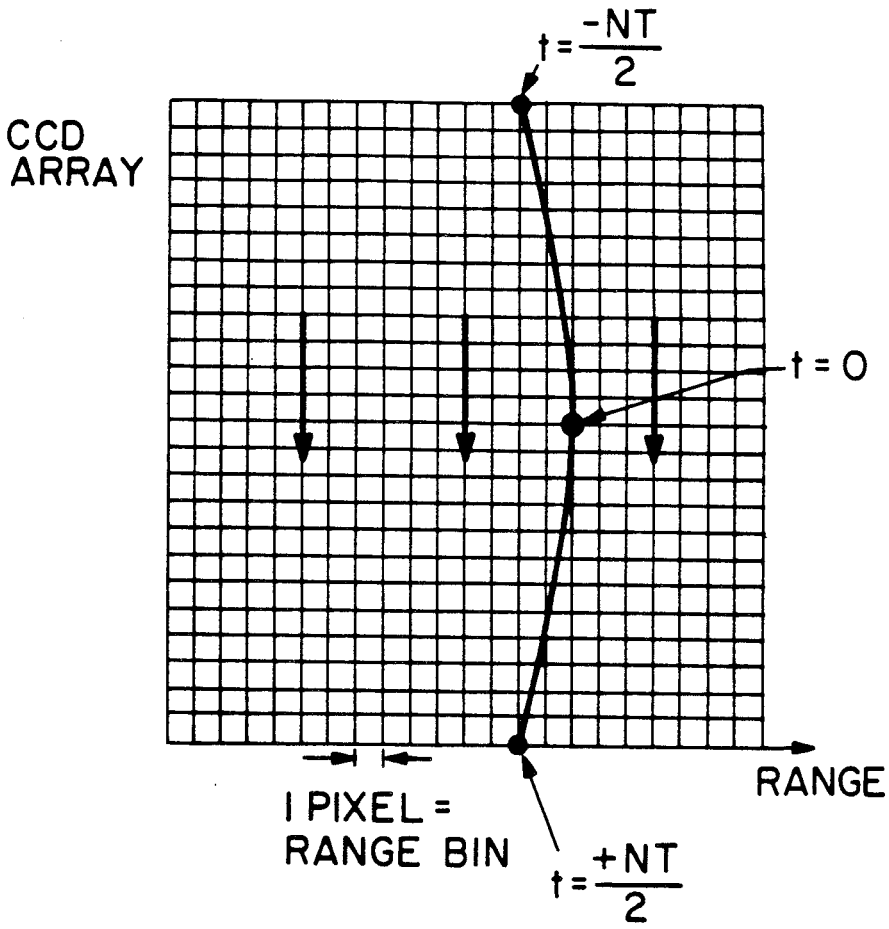

Figure 5.4. Migration of forming image of point scatterer on TDI CCD due to range curvature.

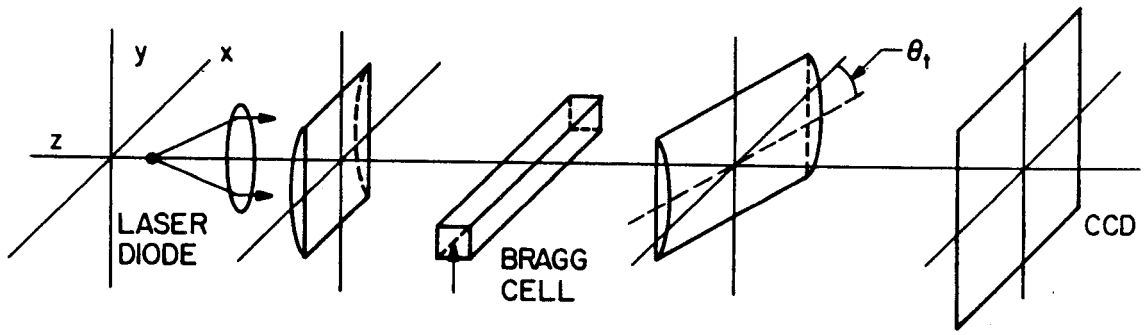

Figure 5.5. Compensation for range curvature.

the distortion is of equal amplitude and opposite in direction to the curvature due to the range curvature then the image of the point scatterer will form in a single range bin as desired. The amount of curvature in the induced barrel distortion is determined by θ_t as follows. We assume that the cylindrical lens is plano-convex with focal length f, index of refraction n, and has a clear aperture larger than the size of the CCD in the azimuth dimension, $N\delta y$. Barrel distortion results due to the lateral shift (in the x direction) in an optical ray as it passes through the finite thickness of the tilted lens. If the ray is passing through a portion of the lens with thickness Δ, then the lateral shift of the ray is:

$$\delta \sim \theta_t \Delta(1-1/n). \tag{5.6}$$

Eq. 5.6 follows from a simple application of Snell's law, with the assumption that θ_t is small. From a straightforward geometrical analysis, with the paraxial approximation, the maximum difference in thickness between the center of the lens and the part of the lens opposite the top (or bottom) of the CCD is found to be:

$$\Delta_{max} \sim N^2(\delta y)^2/8(n-1)f. \tag{5.7}$$

The correct tilt angle is found by equating the maximum lateral shift, δ_{max}, with the maximum range migration in the processor due to the range curvature:

$$\delta_{max} \sim \theta_t \Delta_{max}(1-1/n) \sim Mv_a(NvT/2)^2/2cR_o, \qquad (5.8)$$

where M is the magnification of the optical system in the range direction from the focal plane of the induced 1-D Fresnel zone plate to the CCD plane. By substituting Eq. 5.7 into Eq. 5.8 and rearranging, we find the required tilt angle to correct for range curvature in the processor to be:

$$\theta_t = Mnfv_a(vT/\delta y)^2/R_o c. \qquad (5.9)$$

5.4 Range Walk Compensation

Neglecting range curvature, examination of Eq. 5.5 reveals that, in addition to the constant range delay and quadratic phase history impressed on the return signal from a point scatterer, the forward-looking geometry has produced 2 other modulating terms. The first of these is a linear phase term (in n) that manifests itself as an upshift in frequency at twice the average doppler frequency, $\bar{\omega}_d$, where:

$$\bar{\omega}_d = v\omega_o \cos\theta_o / c. \qquad (5.10)$$

Compensation for this gross doppler term is straightforward. The reference sinusoid in the AO cell is simply up-shifted by $2\bar{\omega}_d$, or, equivalently, the radar return is down-shifted by $2\bar{\omega}_d$, so that the resulting interfering beams beat at base-band as in the side-looking geometry. We note that if carrier encoding, at a spatial carrier frequency ω_m, is used

for bias removal, then the temporal frequency shift used is $2\bar{\omega}_d + \omega_m v_p$. In theory the processor can perform azimuth compression on the forward-looking SAR returns without frequency shifting by simply using an azimuth reference mask that is encoded on a spatial carrier corresponding to the gross doppler frequency. In practice, however, the spatial carrier frequency required is too high to be effectively sampled by the CCD array unless the geometry is nearly side-looking, i.e., $\theta_o \sim 90$ degrees. In most forward-looking SAR geometries the squint angles that are used are not near 90 degrees, and therefore compensation for the gross doppler shift is required.

The second modulating effect of the forward-looking geometry is the cumulative range walk delays in the sequence of azimuth slices. The period between successive return pulses is reduced by a time increment $\tilde{t}$, for each pulse, where $\tilde{t}$ is given by:

$$\tilde{t} = 2vT\cos\theta_o/c. \qquad (5.11)$$

If left uncompensated in the SAR processor, the range walk delays lead to a smearing of the range focused signals across the CCD during the integration period. The total range walk excursion on the CCD is:

$$\delta_{rw} = Mv_a N\tilde{t} = 2NMv_a vT\cos\theta_o/c. \qquad (5.12)$$

Compensation for the range walk delays in the processor is

accomplished by tilting the CCD and mask about the optical axis such that the lateral movement (due to range walk) of the range focused data at the output plane is exactly matched by the lateral movement of the shifting charge on the CCD. The required tilt angle is given by:

$$\theta_d = \sin^{-1}[2MvTv_a\cos\theta_o/c\delta y], \qquad (5.13)$$

where δy is the CCD pixel size in the y dimension. If $M = c\delta y/2vTv_a$ then the scale of the orthogonal spatial coordinates on the CCD matches the scale of the actual ground coordinates. In this case θ_d is equal to the angle of deviation from side-looking, i.e., the compliment of the squint angle $(90^\circ - \theta_o)$.

In order to generate a strip-map of the swath, in which the output is scrolled continuously as long as the radar's velocity vector remains unchanged, the x' and y' coordinates of the CCD must correspond to the x and y coordinates of the target as in Fig. 2.1. To achieve proper registration of the point scatterers which make up the target scene, the reference mask must account for the linear variation in doppler shift (as a function of y) across the target swath for scatterers with the same x coordinate. A geometrical analysis of the forward-looking geometry and tilted CCD yields the following expression for the transmittance of the reference mask:

$$T(x',y') \sim (1 + \cos[\bar{b}_i'(1-\bar{\alpha}'x')(y')^2 + \tan\theta_m x'], \quad (5.14)$$

where: $\bar{b}_i' = b_i'\sin^2\theta_o$, $\bar{\alpha}' = c/Mv_aR_o\sin\theta_o$, and:

$$\tan\theta_m = \delta y c\cos\theta_d/2MvTv_a\sin\theta_o\tan\theta_o. \quad (5.15)$$

The x' and y' coordinates in Eq. 5.14 are in the (rotated) frame of the CCD. If $\theta_o = 90^\circ$, then Eq. 5.14 reduces to the side-looking reference function given by Eq. 3.15. If the CCD coordinate scaling matches that of the ground, i.e., $M = c\delta y/2vTv_a$, then $\theta_m = 90^\circ - \theta_o$.

We have demonstrated experimentally the ability of the SAR processor to correct for range walk in a forward-looking geometry. For this demonstration the SAR impulse response simulator (described in Chap.3) was modified to add a small, programmed fixed delay to the period between successive pulses, thereby simulating the range walk effect. For the experiments reported here a range delay of 1.8 microseconds per integration period was selected as representative of an airborne forward-looking geometry. This range walk corresponds to a radar flying at 300 meters/second with a squint angle of approximately 25°. The integration time is 1 second and N = 512.

If the processor did not compensate for the range walk given by the above parameters, the range focused data would suffer a spread of approximately 37 pixels on the CCD (as given by Eq. 5.12), thus drastically degrading the quality of the image. Fig. 5.6a is a perspective view of the

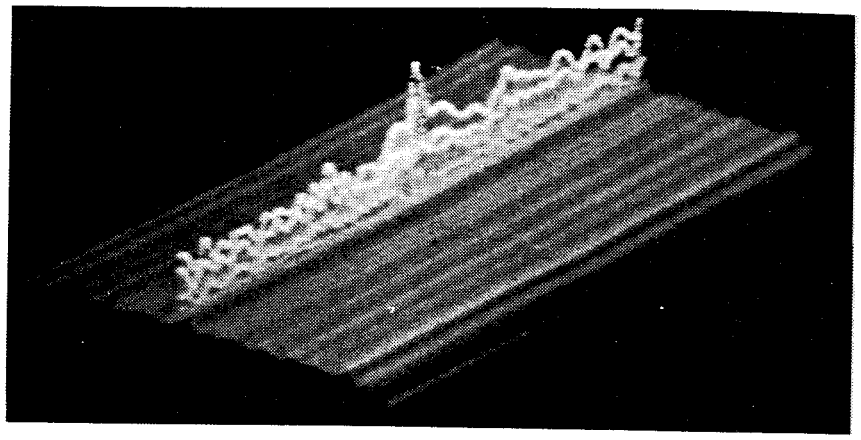

(a) Side-looking

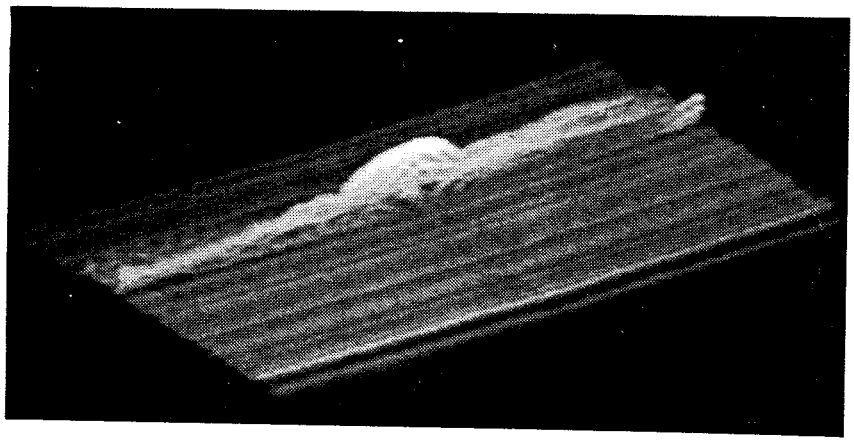

(b) Forward-looking, without range walk compensation.

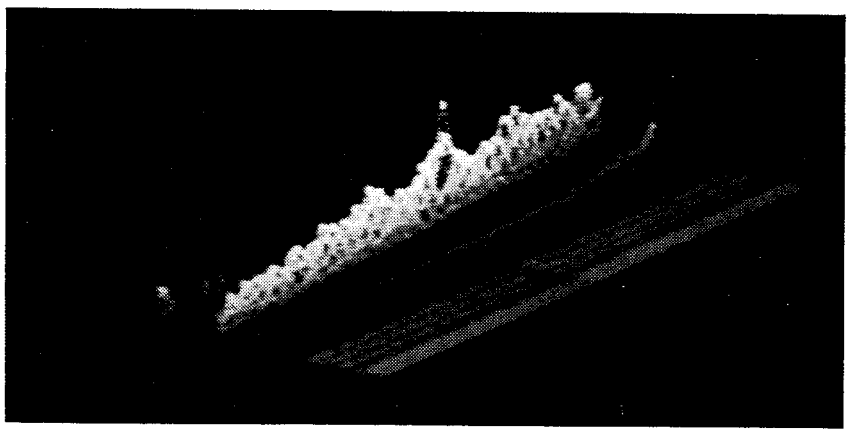

(c) Forward-looking, with range walk compensation.

Figure 5.6 Processor output without bias removal.

undemodulated output of the SAR processor for the side-looking (no range walk) case for a simulated radar scatterer that has a TBWP of 80. The bias ridge that is later removed by the demodulator is visible along the azimuth coordinate. Fig. 5.6b shows the impact of uncompensated range walk on the output of the processor. The data is smeared in both range and azimuth and the narrow focused peak is lost. Fig. 5.6c is the output of the processor when range walk compensation is introduced. The narrow focused peak returns and the only noticeable difference between the side-looking and forward-looking cases is the tilt in the bias ridge. The range walk compensation was accomplished by rotating the CCD by an angle of approximately 4.2 degrees as prescribed by Eq. 5.13. Shown in Fig. 5.7 are the demodulated outputs corresponding to the three cases of Fig. 5.6. The corresponding 2-D images are shown in Fig. 5.8. The data show that, when range walk is compensated, the resolution achieved in the forward-looking case is comparable to that of the side-looking geometry.

Electronic compensation for the accumulating delay terms can be used as an alternative to the mechanical range walk correction technique described above. To implement electronic compensation the period between successive laser diode trigger signals in the processor is programmed to be shortened by E. As a result the range focused signals from a point scatterer will all fall within the same range bin at

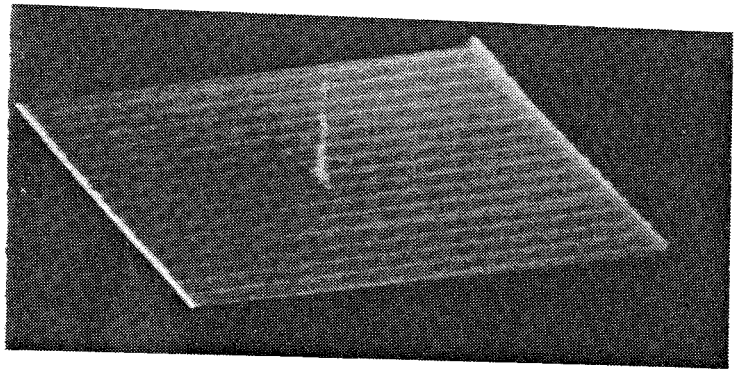

(a) Side-looking.

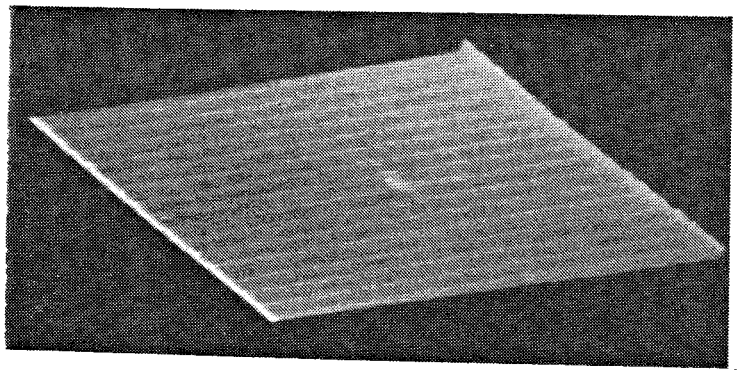

(b) Forward-looking without range walk compensation.

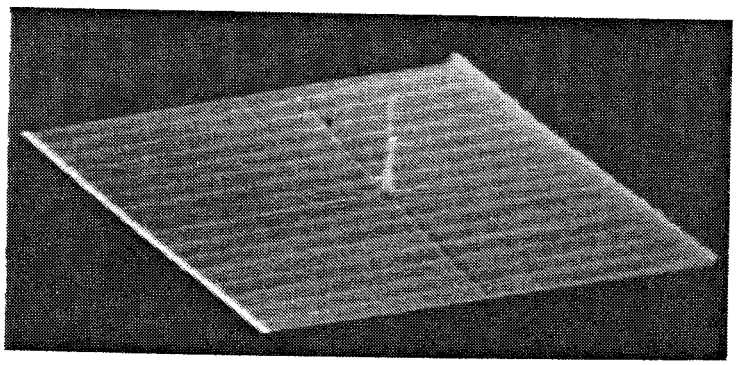

(c) Forward-looking with range-walk compensation.

Figure 5.7. Processor output with bias removal.

(a)

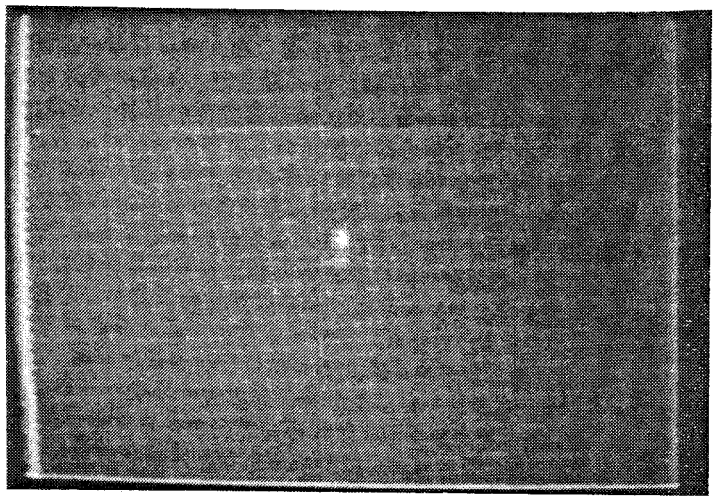

(b)

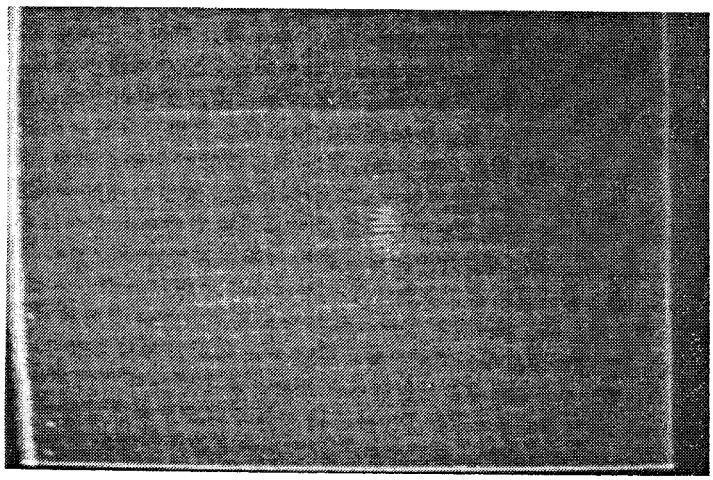

(c)

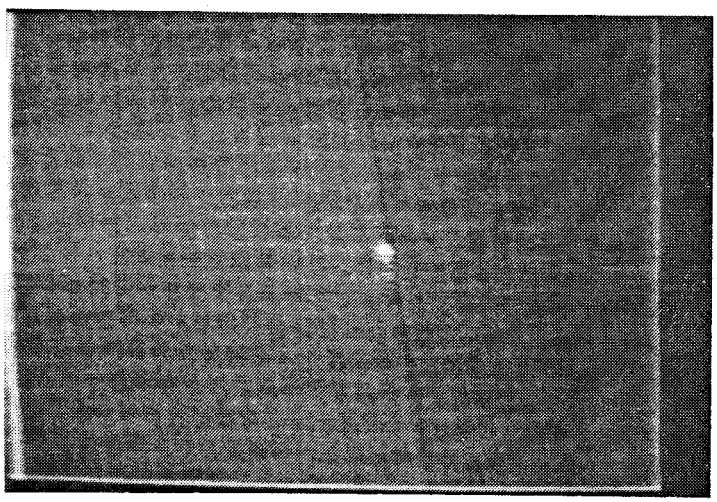

Figure 5.8. Processor output with bias removed.

the output (CCD) plane in a manner similar to the side-looking processor so that there is no need for rotation of the CCD. With this form of range walk compensation the x and y coordinates of the CCD correspond to ρ and γR_θ in the target field, whereas the image generated with the rotated CCD technique is oriented along the x and y coordinates of the ground. For this reason the required azimuth reference mask is somewhat simpler than that given by Eq. 5.14 and resembles the mask prescribed for the side-looking geometry with the only difference being that the overall chirp rate is reduced by a factor of $\sin^2\theta_\theta$. The azimuth reference mask function, when temporal compensation is used, is thus given by:

$$T(x',y') \sim 1 + \cos[\bar{b}_1'(1-\alpha' x'/M)(y')^2]. \qquad (5.16)$$

A continuously scrolled strip-map cannot be formed using electronic range walk compensation because the image that forms on the CCD is rotated with respect to the x and y axes on the ground. The image can be formed only in a framed format as in spot-light mode SAR applications. Successive frames of focused data are achieved by resetting the period between returns to 1/prf at the beginning of each frame. One advantage of using electronic compensation for the range walk delays is that it permits the range curvature technique, that was described previously, to be used if needed. Both forms of range migration can be compensated

simultaneously because the CCD is not rotated with respect to the AOD (as in Fig. 5.5). The required tilt angle for range curvature correction with this approach is $\theta_t \sin^2\theta_o$, where θ_t is given by Eq. 5.9.

CHAPTER VI. PROGRAMMABLE ARCHITECTURE

6.1 Interferometrically Generated Reference Function

In some applications, the parameters of the radar/target geometry, such as the velocity and altitude of the aircraft, and direction in which the antenna is pointed, may change dynamically. The real-time SAR imager must have the ability to adapt rapidly to such changes in order to continuously produce a well focused image. To accomplish this with the system of Fig. 3.10, the mask could be replaced by a real-time 2-D SLM on which the proper reference function is written. Ideally this SLM would be electronically addressable so that the reference function could be calculated, stored in electronic memory, and conveniently down-loaded to the SLM. This technique, however, has significant drawbacks. The characteristics of the 2-D SLM would limit the dynamic range, speed, and resolution of the processor. Furthermore, a very fast, large capacity electronic buffer memory would be needed to update the filter at real-time rates.

To avoid the problems associated with using a 2-D SLM in the processor we have developed an alternate and preferable technique for incorporating the programmable azimuth filter. Examination of the required 2-D reference function (see Eq. 3.15 and Fig. 3.12) reveals that it is

approximated well by a 1-D baseband LFM signal in the azimuth direction, whose scale varies linearly in the range direction to account for the range/azimuth coupling of the geometry. We recall that this approximation is valid because we assume that the overall range to the target is large when compared to the swath width. This fact suggests that a 1-D SLM can be used to enter the reference function into the processor and the range/azimuth coupling can be introduced electronically or by an appropriate anamorphic lens arrangement to provide the scaling in the orthogonal direction.

We have implemented this approach using an AO cell as the 1-D SLM. Fig. 6.1 is a schematic representation of the experiment we performed to verify this technique. An electronic chirp signal is applied to an AOD along with a sinusoidal reference signal. After the acoustic signals have propagated to the center of the AOD, the laser diode is pulsed to freeze the moving diffraction gratings in the same manner as the radar signal is sampled in the AOD of the SAR processor described previously. An anamorphic lens arrangement is used to spread the diffracted light uniformly in the x direction at the detector plane. The undiffracted light (not shown in Fig. 6.1) is blocked and not used. In the y direction the diffracted light from the sinusoidal reference signal in the AOD is a plane wave that is transformed into a cylindrical wave at the detector plane.

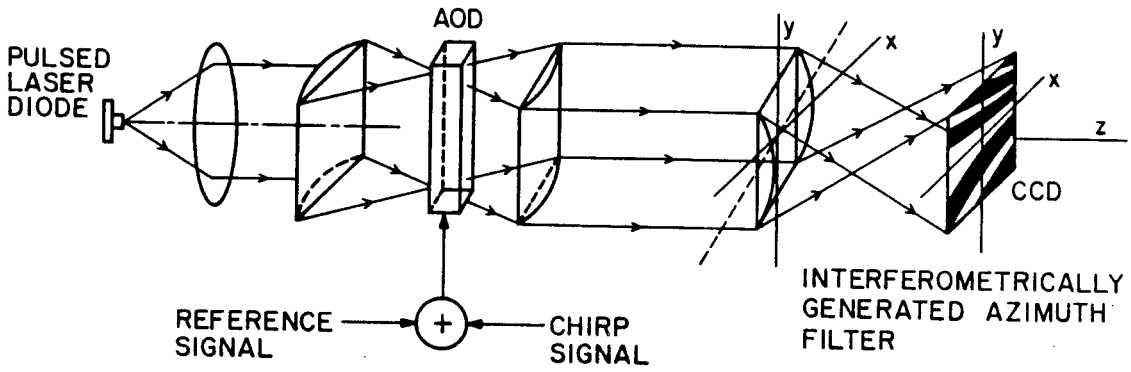

Figure 6.1. Optical set-up for the interferometric generation of the SAR azimuth filter.

The light diffracted by the chirp signal is a cylindrical wave that is transformed into a cylindrical wave of different curvature at the detector plane. The waves from the chirp and reference signals have different radii of curvature and therefore, under the paraxial approximation, the resulting interference pattern on the detector will be equal to a LFM signal in the y direction. The scaling that is required in the x direction to account for the range/azimuth coupling is accomplished by tilting a cylindrical lens about the y axis, as shown in Fig. 6.1.

Various tilted anamorphic lens arrangments can be used to compensate for the range/azimuth coupling. In the following we derive an expression for the tilt angle needed

for a single cylindrical lens that is initially positioned to schlieren image the AO cell onto the CCD in the y direction with a magnifcation of 1. In this case the distance, in Fig. 6.1, between the AO cell or the CCD, and the center of the tilted lens is equal to 2f. If the lens is tilted about the y axis by an angle θ_α, then the object and image distances, as a function of x, are given by:

$$d_o = 2f + x(\tan\theta_\alpha),$$
$$d_i = 2f - x(\tan\theta_\alpha). \qquad (6.1)$$

In the general case we assume that the optical system scales the interferometrically generated azimuth filter, along the x dimension, to match the width of the CCD. The scale factor is m_α. If $x(\tan\theta_\alpha) \ll f$, then the imaging condition along the y direction, between the AOD and CCD, is maintained and the magnification of the azimuth filter is given by:

$$M_\alpha(x) \sim 1 - m_\alpha x(\tan\theta_\alpha)/f. \qquad (6.2)$$

We assume the laser diode's pulsewidth is short enough to effectively sample the moving diffraction grating. The diffraction pattern can therefore be considered stationary. The sinusoidal reference and chirp signals have equal amplitudes. The chirp rate and starting frequency of the azimuth filter function are selected such that the intensity distribution of the diffracted beam is given by:

$$I_{az}(y) \sim 1 + \cos(Б_i y^2). \tag{6.3}$$

The resulting intensity pattern at the CCD plane is given by:

$$I_{az}(x,y) = I_{az}(M_\alpha(x)y) \sim 1 + \cos(Б_i(1 - m_\alpha x(\tan\theta_\alpha)/f)y^2). \tag{6.4}$$

A comparison of Eqs. 6.4 and 5.16 reveals that the 2-D interferometric pattern on the CCD will match the desired function if:

$$2m_\alpha \tan\theta_\alpha/f = \alpha'/M = 2v_a/McR_o. \tag{6.5}$$

Rearranging, we find that the required tilt angle is:

$$\theta_\alpha = \tan^{-1}(fv_a/m_\alpha McR_o). \tag{6.6}$$

Fig. 6.2 are examples of interferometrically generated azimuth filters with characteristics similar to those of the fixed reference mask in Fig. 3.12. In Fig 6.2a there is no range/azimuth coupling. In Fig. 6.2b a lens was tilted as described above to match the range/azimuth coupling of the mask in Fig 3.12. A comparison of Figs. 6.2b and 3.12 shows that, aside from differences in levels of exposure, the interferometrically generated function has nearly the same azimuth bandwidth and range/azimuth coupling parameter as the fixed mask. To obtain the data in Fig. 6.2 the 2-D CCD camera was operated in the standard video mode and its

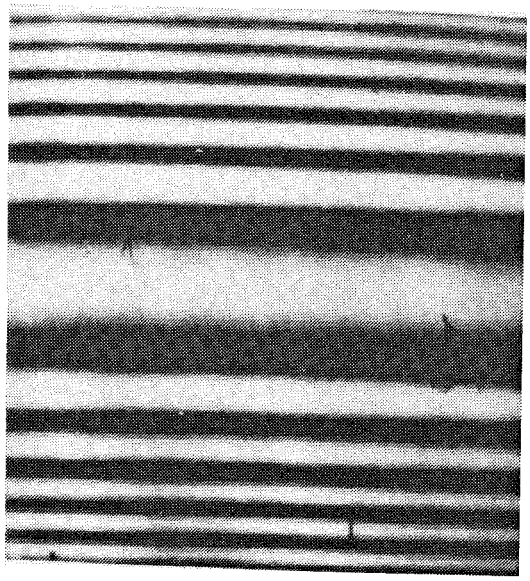

(a) No range/azimuth coupling.

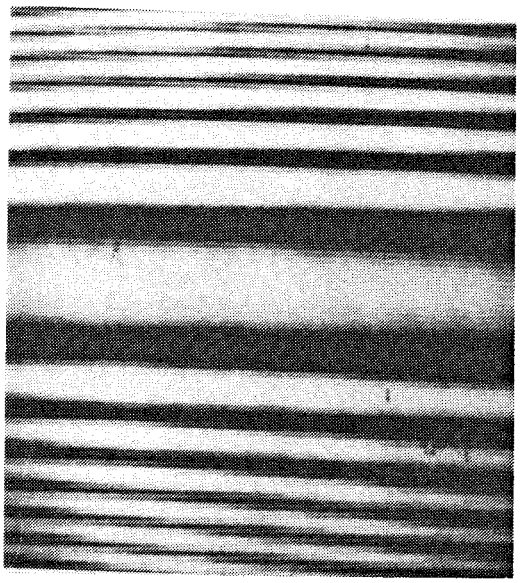

(b) with range/azimuth coupling.

Figure 6.2. Interferometrically generated reference functions

output displayed on a monitor. During the integration period of each video frame the AO cell was loaded and illuminated several hundred times to produce a high contrast ratio in the displayed reference function. The portion of the chirp signal used was approximately 3 microseconds long and had a bandwidth of 10 MHz (We used the same SAW chirp generator for this experiment that was used in the simulator.). The AO cell used was a slow shear wave TeO_2 device similiar to the one in the non-programmable processor used to enter the SAR data. The laser diode in this experiment was operated at pulsewidth of 50 nanoseconds.

An architecture using the interferometrically generated reference filter has the flexibility to adapt to changes in the radar/target geometry by changing the characteristics of the electronically generated chirp. The parameters that may be changed include the starting frequency, the starting time, and the chirp rate of the azimuth reference signal.

When integrated into the imager, the interferometric azimuth filter technique provides two possible modes of operation. Operation of the CCD in the shift-and-add mode, while repeating the same azimuth filter signal for each radar return, will complete the necessary azimuth correlation as in the original processor. This mode is used for strip-map SAR in which the output image is scrolled. Alternativly, the azimuth correlation may be performed by electronically shifting the reference function

incrementally in the AOD and using a non-shifting integrating CCD detector array. In this mode the image is generated in a framed format that is more useful for spotlight mode SAR. This capability is also useful for performing multiple looks, i.e., forming several images of the same scene independently and adding them incoherently to reduce speckle.

6.2 Crossed Bragg Cell Architecture

A programmable real-time SAR processing architecture is synthesized by integrating the interferometric technique for SAR azimuth filtering with the range processing technique of Fig. 3.7. One possible approach is an additive interferometric architecture in which the AOD containing the radar waveform is placed in one arm of a Mach-Zehnder interferometer and the AOD containing the azimuth reference is placed in the second arm and oriented orthogonally to the first AOD. This architecture is shown schematically in Fig. 6.3. For clarity the lenses are not shown. We assume that the undiffracted light from the 2 AO cells is blocked through Fourier plane filtering. This also is not shown. Since the diffracted beams from the 2 AO cells interfere at the CCD plane, there is no need for reference signals in either of the cells. For a single point scatterer, the resultant optical field at the CCD plane due to AOD1, for the nth return, is $f_1'(x,vnT)$, as given by Eq. 3.10. We

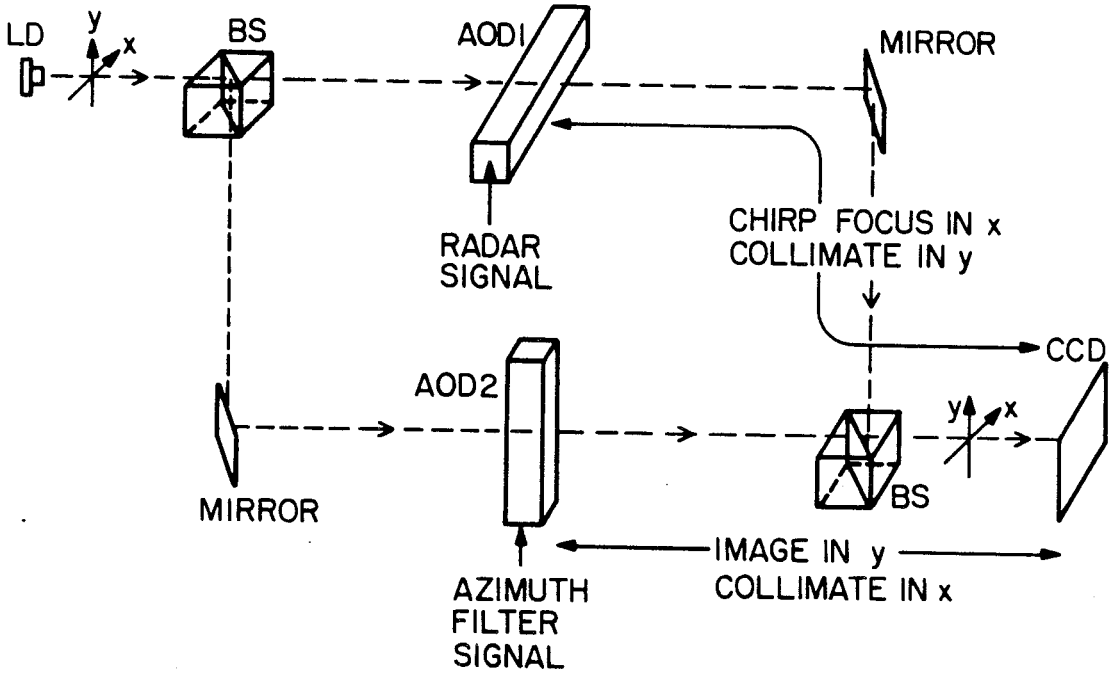

Figure 6.3. Additive interferometric architecture.

assume that the range/azimuth coupling is compensated as described above. Consequently, the field at the CCD plane due to the azimuth filter signal diffracted by AOD2 is:

$$E_{az}(x,y) = A\exp(jb_i'(1-\alpha'x')y^2). \qquad (6.7)$$

Operation of the CCD in the TDI mode, as described previously, results in the following interference pattern at the output plane:

$$I_a(x,y,n) = | f_i'(x,vnT) + E_{az}(x,y-n\delta y) |^2. \qquad (6.8)$$

After N return pulses have been received the resultant charge pattern on the CCD is:

$$Q(x',y') \sim \sum_{N} I_a(x,y,n)$$

$$= NA^2 + N\sigma_0^2 \mathrm{sinc}^2[(x'-x_0')\bar{X}'b_i'] +$$

$$2NA\sigma_0 \mathrm{sinc}[(x'-x_0')\bar{X}'b_i']\mathrm{sinc}[b_i'N\delta y(1-\alpha' x_0')(y'-y_0')]\cos\mu_0 . \qquad (6.9)$$

This result is identical to that of the non-programmable architecture (see Eq. 3.16) with the exception that the signal term is twice as large. The dynamic range of the additive interferometric architecture will therefore approach twice that of the non-programmable architecture as given by Eq. 4.12 for large M. Despite this advantage, this approach is subject to the same sensitivity to mechanical vibration that plagues all multiple path interferometers.

An alternate and preferable approach is a multiplicative interferometric architecture in which the radar and azimuth filter systems are cascaded. In this implementation the interfering beams pass through the same optics and thus the stability problems are minimized. The cascaded system is shown schematically in Fig. 6.4. Unlike the additive interferometric architecture, a fixed reference beam is required from each of the AODs. As in the original processor, the radar signal is range focused and its phase is detected interferometrically at the detector by a

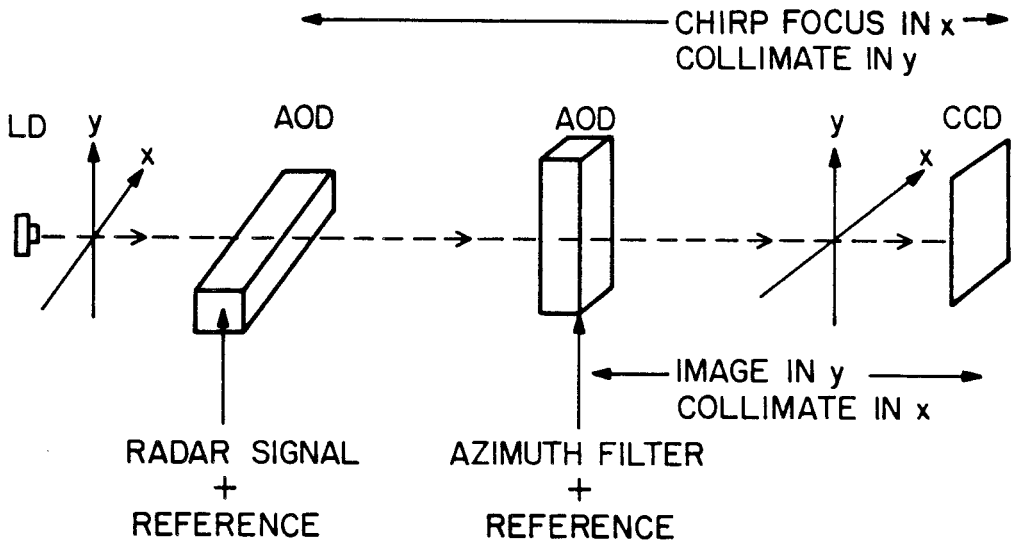

Figure 6.4. Multiplicative interferometric architecture.

reference beam that is generated by the same AOD. However, since the diffracted light from the first AOD is also diffracted by the second AOD, which contains the azimuth reference signal plus a sinusoidal signal, it is multiplied by the interferometrically generated reference function. This implementation thus achieves the same multiplication needed to perform the azimuth compression as in the original non-programmable architecture.

The optical field at the CCD plane, due to the doubly

diffracted light is given by:

$$E_m(x,y,n) \sim [f_i'(x,vnT) + A][1 + \exp(jb_i'(1-\alpha'x')(y-\delta yn)^2], \tag{6.10}$$

where the first term in brackets represents the field due to the AOD containing the radar returns and the second term is due to AOD containing the azimuth reference filter. The intensity detected by the CCD is given by:

$$I_m(x,y,n) = |E_m(x,y,n)|^2 \sim$$

$$|(f_i'(x,vnT) + A)|^2(1 + \cos(b_i'(1-\alpha'x')(y-\delta yn)^2). \tag{6.11}$$

The charge that accumulates on the CCD is:

$$Q(x,y) \sim \sum_N I_m(x,y,n). \tag{6.12}$$

After substitution of Eq. 6.11 Eq. 6.12 is identical in form to Eq. 3.16. The programmable multiplicative architecture therefore yields the same result as the original non-programmable processor.

A more detailed schematic diagram of an implementation of the multiplicative interferometric architecture is shown in Fig. 6.5. The top view shows the path of the light beams in the range dimension when the radar returns of a single point scatterer are processed. The light diffracted by the induced Fresnel zone plate focuses on the CCD to perform the range compensation. As in the original architecture, this wave interferes with a collimated (in the x direction) beam

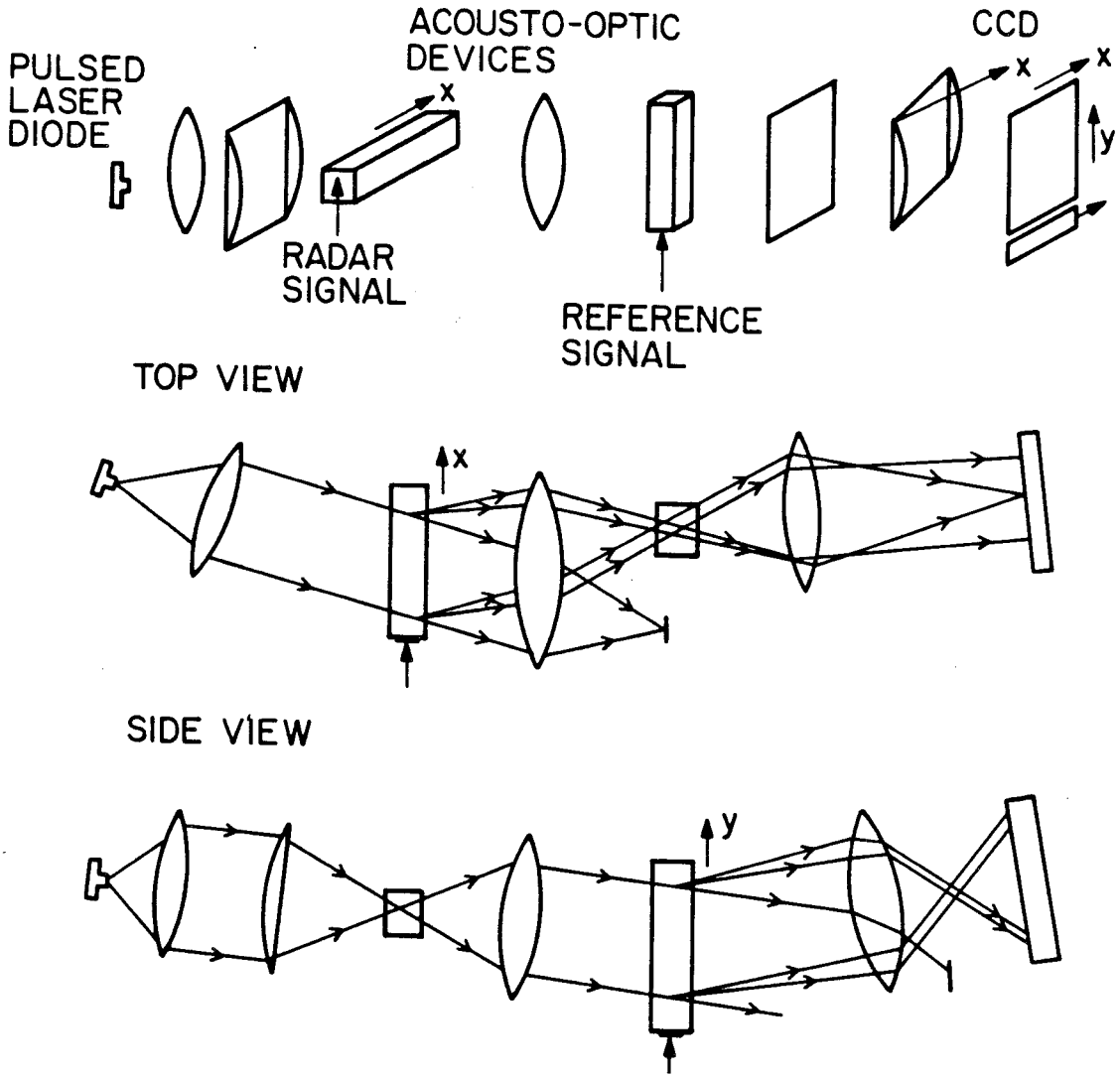

Figure 6.5. Optical architecture for SAR imaging with the azimuth reference introduced through a second AO cell.

that arises from the sinusoidal reference signal. Both beams pass through the second AOD containing the azimuth filter signal and a sinusoidal reference. The light diffracted by this AOD in the y direction consists of a converging (or diverging) beam and a collimated beam (shown in the side view) which pass through the tilted cylindrical lens (which compensates for range/azimuth coupling) and ultimately interfere at the detector plane to produce the azimuth filter.

To validate the multiplicative approach we have implemented two processors which use crossed AODs in a manner similar to the one shown in Fig. 6.5. One processor was designed to operate in the scrolling mode, while the other was set up to operate in the framing mode. We characterized the impulse response of both processors. The details of this characterization are contained in the next 2 sections. A photograph of one of the experimental set-ups is shown in Fig. 6.6.

The pulsed laser diode source used in these processors (the leftmost component in Fig. 6.6) was an AlGaAs device capable of several watts peak output power. The higher power source was necessary because the processed light was diffracted by two AODs, each usually operated at less than 5% diffraction efficiency to minimize nonlinearities. Although this source did not operate in a single longitudinal mode, as did the low power laser in the

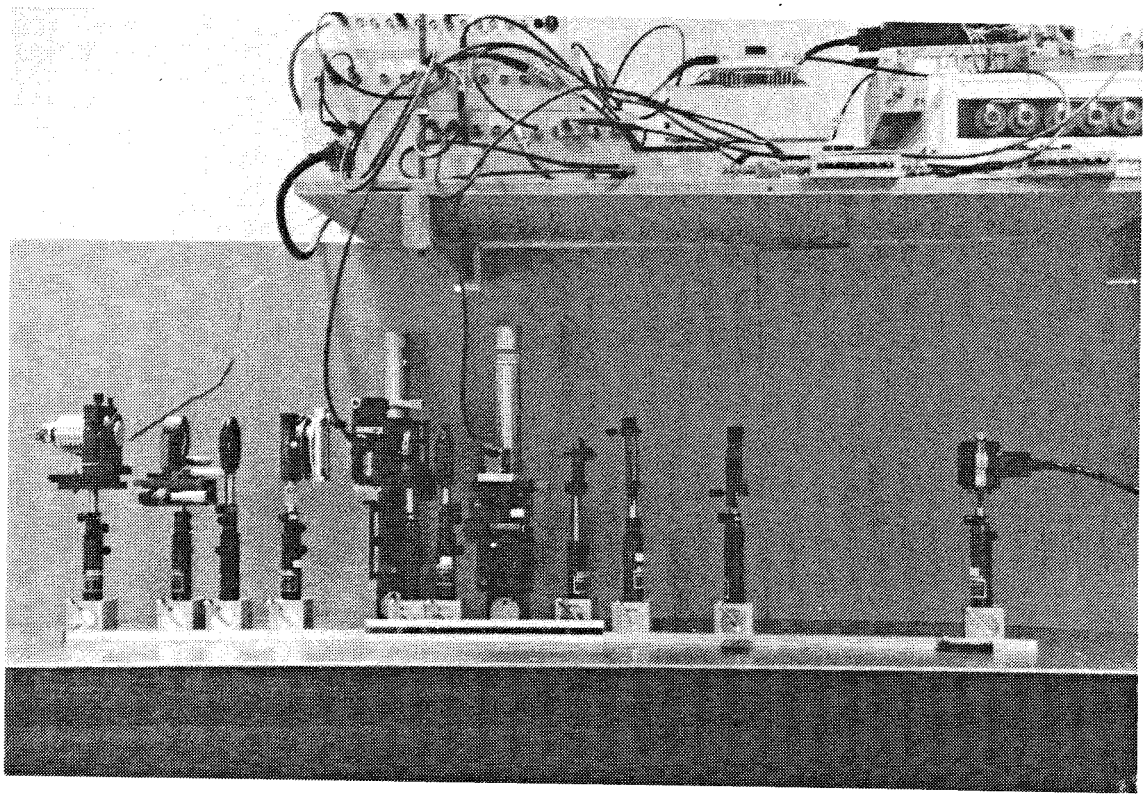

Figure 6.6. Experimental set-up used to demonstrate the programmable architecture.

nonprogrammable architecture, it still possessed sufficient temporal coherence (with a line width of about 3 nanometers) to achieve good fringe depth in the range focused beams.

6.3 Application to Strip-map SAR

6.3.1 Experiment

The most direct application of the multiplicative interferometric architecture is to side-looking strip-map SAR. In this case the operation of the processor is

essentially identical to that of the non-programmable architecture in that the interferometrically generated azimuth function remains fixed throughout the integration period (as does the mask in the nonprogrammable approach), the azimuth correlation results from the integration of shifting charge on the CCD, and the image is scrolled out of the processor at the prf of the radar. To duplicate the modulating effects of the mask, the electronic azimuth signal is loaded into the AOD in synchronism with the radar returns. The timing is such that the sampling laser diode freezes the azimuth signal at the same location in the AOD for every pulse in the integration period.

The architecture used in the demonstration was essentially equivalent to the one shown in Fig. 6.5 with the exception that the two components were cascaded in reverse order. By placing the azimuth filter ahead of the range compression section, any unwanted barrel distortion arising from the tilted cylindrical lens is avoided.

An azimuth TBWP product of 80 was selected for the simulated target. This allowed us to make a direct comparison with the nonprogrammable architecture which used the same target TBWP for much of the data (see Chap. 4). An oscilloscope trace of the signal applied to the azimuth AOD is shown in Fig. 6.7. This signal consists of the sum of a 60 MHz sinusoid and a LFM of equal amplitude, centered at 60 MHz, with a chirp rate of about 4×10^{12} Hz/sec. The

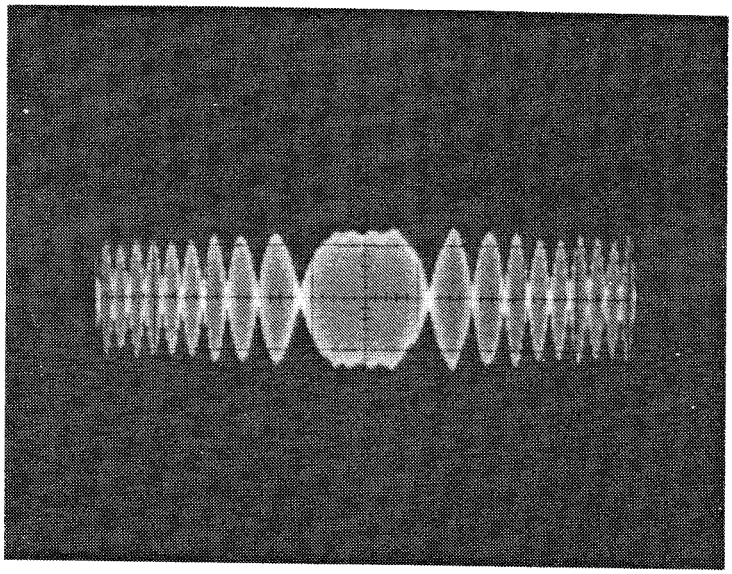

Figure 6.7. Azimuth filter signal, .5μsec/div.

beating of the two signals in the scope trace reveals the chirped nature of the azimuth filter signal. The intensity of the optical wave due to this signal is proportional to the envelope of the square of the waveform in Fig. 6.7. The optical magnification along the y direction was adjusted such that the resultant interferometric azimuth filter at the output plane had a SBWP product of 80 over the aperture of the CCD. The interference pattern was therefore similar to those shown in Fig. 6.2, but with slightly higher bandwidth, so that there were approximately 10 fringes on either side of the central lobe.

The simulated target signals were generated by the radar

simulator as described in Chap. 3. An integration period of 1 second was used. The bottom trace of Fig. 6.8a shows the principal value of the quadratic phase history of the simulated target. For display purposes, the sum of a 60 MHz signal, phase modulated with the quadratic function of Fig. 6.8a, and an unmodulated 60 MHz reference of equal amplitude is shown in the top trace of Fig. 6.8a. A time expanded view of these signals is shown in Fig 6.8b revealing the discrete nature of the simulated phase history. The stored phase function consists of 512 samples. The intensity of the range focused light wave is modulated by the envelope of the square of the signal in the top trace of Fig. 6.8.

The azimuth compression in the processor is therefore achieved by a temporal correlation of the envelope of the square of the signal in Fig. 6.8a with the envelope of the square of the signal in Fig. 6.7. Ideally, this correlation is an autocorrelation. Fig. 6.9 consists of isometric images of a simulated point scatterer focused with the scrolling mode of operation. A comparison of Figs. 6.9b and 4.29 shows that the operation of the multiplicative architecture is nearly identical to that of the nonprogrammable processor.

Bias subtraction with the scrolling mode programmable architecture is implemented in an analogous manner to that described in section 4.1 for the fixed mask approach. To employ the carrier encoding/demodulation technique, the

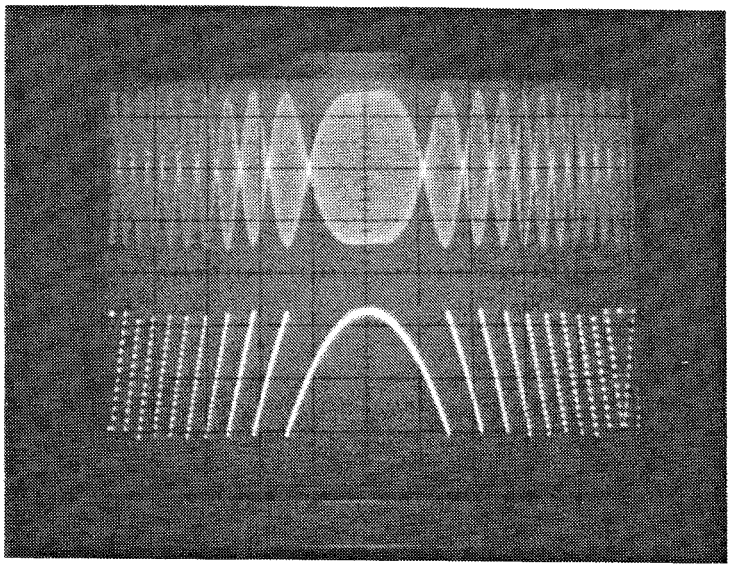

(a) 100 μsec/div.

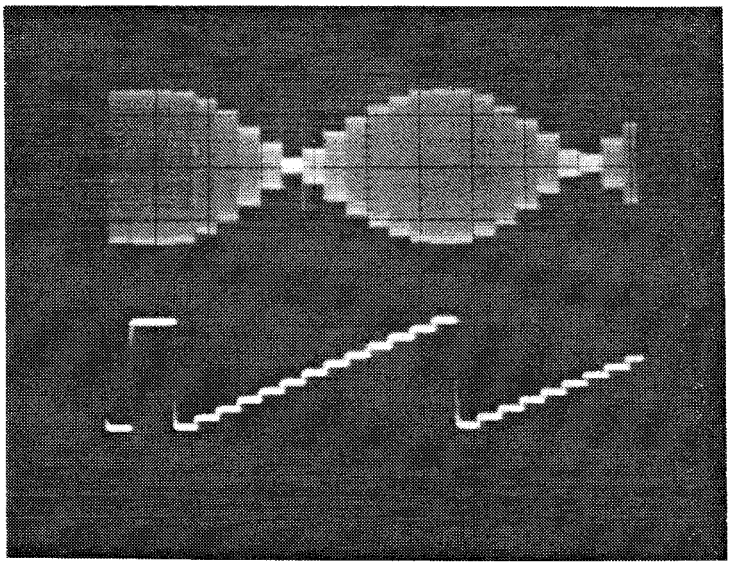

(b) 5 μsec/div.

Figure 6.8. Phase history of simulated point scatterer.

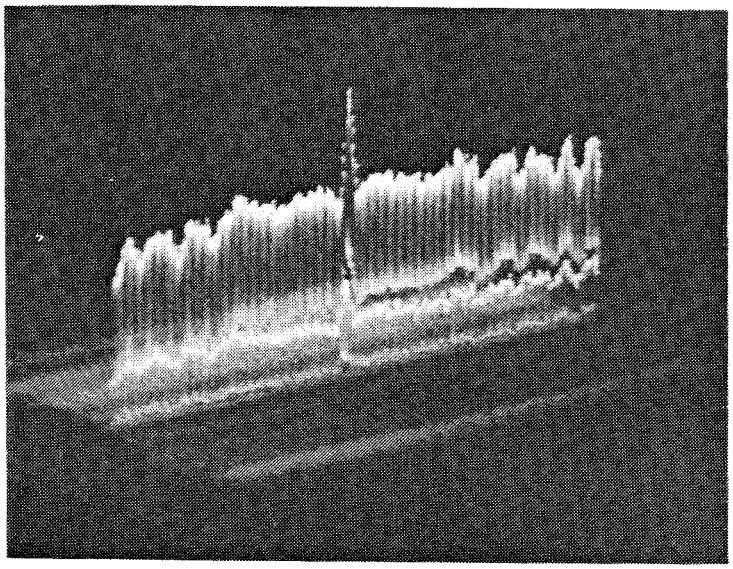

(a)

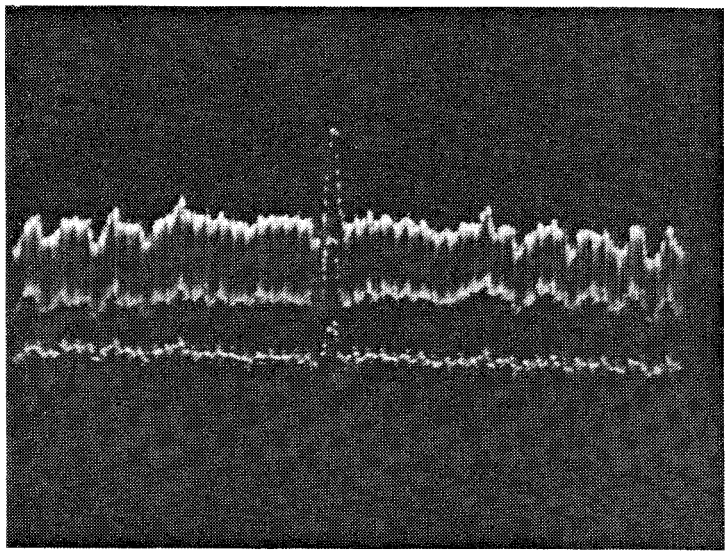

(b)

Figure 6.9. Isometrically displayed images of simulated point scatterers without bias removal, TBWP = 80.

desired spatial carrier for the azimuth filter is generated by an appropriate temporal frequency shift of the azimuth signal. This carrier manifests itself as a spatial carrier in the diffracted beam. If f_m is the desired spatial carrier frequency in the azimuth filter at the output plane, then the temporal frequency shift required in the azimuth signal is:

$$\bar{f}_m = \bar{m} f_m v_a, \tag{6.13}$$

where $\bar{m}$ is the optical magnification of the azimuth filter in the y direction. The phase history of the simulated target is shifted by $\omega_m v_p$, as for the nonprogrammable architecture (see section 4.2). Fig. 6.10 shows the results of the experimental demonstration of bias removal with the interferometric architecture. The spatial carrier frequency used matched that used for the nonprogrammable architecture (1/6 cycles/pixel), and the results of bias removal are similiar.

6.3.2 Electronic Range/Azimuth Coupling Compensation

In general it is desirable to have full electronic programmability of the azimuth reference function. To accomplish this with the architecture in Fig. 6.5 requires the tilted lens to be mounted on a motorized rotational positioner that automatically would adjust the tilt angle, according to Eq. 6.6, for changes in the radar/target geometry parameter R_o. Here we propose an alternate

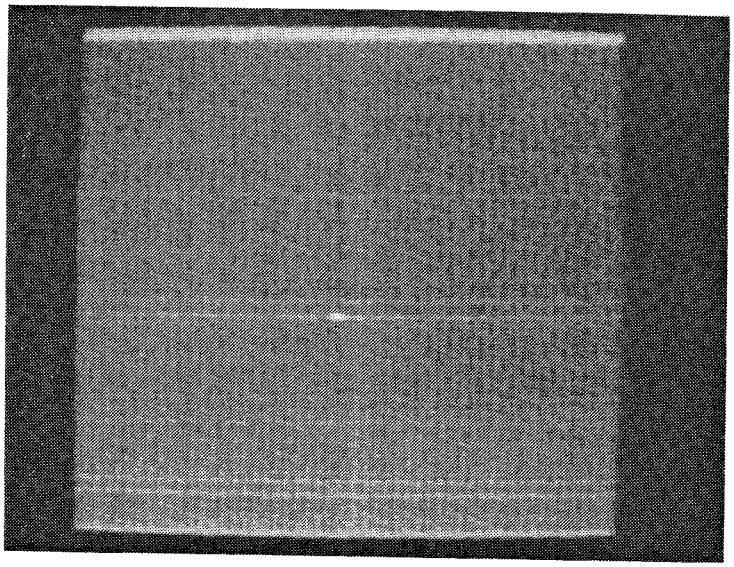

Figure 6.10 Image of simulated point scatterer formed with programmable architecture with bias removed.

technique in which the range/azimuth coupling effect is compensated via an appropriate electronic modulation of the reference signal in the AOD containing the radar returns, and requires no mechanical movement of the optical elements. The basic idea is to correct for the variation in chirp rate as a function of range by cancelling the range dependent phase component electronically. To do this we modulate the sinusoidal reference signal by the following function:

$$\phi_r(n) = \exp(-jb_2\alpha' x_0'(vnT)^2). \qquad (6.14)$$

The optical intensity at the CCD plane due to the range focused beam interfering with the phase demodulated

reference is thus:

$$I'(x,n) \sim |f_i'(x,vnT) + A\emptyset_r(n)|^2. \qquad (6.15)$$

This expression can be expanded and expressed in a manner similar to Eq. 3.13. After lumping constant phase terms together we find:

$$I(x',n) \sim A^2 + \sigma_o^2 \, \mathrm{sinc}^2[(x'-x_o')\bar{X}'b_i'] + 2A\sigma_o \mathrm{sinc}[(x'-x_o')\bar{X}'b_i']\cos(b_i'(n\delta y - y_o(1-\alpha' x_o'))^2 + \mu_o). \qquad (6.16)$$

We see that, in this case, the chirp rate of the intensity modulation is the same for scatterers at all ranges, but that the azimuthal position of each scatterer is scaled by $(1-\alpha' x_o')$. Therefore, the interferometrically generated reference function, which is correlated with Eq. (6.16) to form the image, should be the same for all range bins. The resulting image, however, will be scaled by the range/azimuth coupling coefficient along the azimuth axis in a manner analogous to the apparent scaling of objects that are extended in range, when observed visually, such as the parallel boarders of a long straight road viewed from a position on the road. If the ratio of the swath width to R_o is $<< 1$, then this effect is negligible. The effects of scaling can be further minimized by employing a combination of electronic and mechanical compensation. For example, the lens could be tilted at an angle corresponding to some nominal value of R_o, and the electronic phase modulation

would be used to compensate for variations from that nominal value.

6.3.3 Multiple Looks

A well known technique for reducing the effects of coherent radar speckle and thereby improving the quality of SAR images is the incoherent averaging of several images of the same scene that have been taken from different aspects. The azimuth resolution cell size of the multiple-look image is increased by a factor of $\bar{n}$ over that possible for a single look, where $\bar{n}$ is the number of looks. In many situations, this reduced azimuth resolution performance is acceptable.

Here we outline a straightforward technique for producing multiple-look images with the real-time strip-map processor. This technique applies to both the non-programmable and programmable versions that have been presented. One CCD for each look is required to implement this approach. Fig. 6.11 is a schematic diagram of the output plane and post-processor required to achieve a 2-look real-time image. The CCDs are stacked together as shown so that each CCD processes separate portions of the scene's azimuthal phase history. The CCDs are operated in the shift-and-add mode, as described earlier. The bias components from each CCD's image are removed as previously described and the result is squared. The image from the first CCD is stored temporarily in a buffer memory and

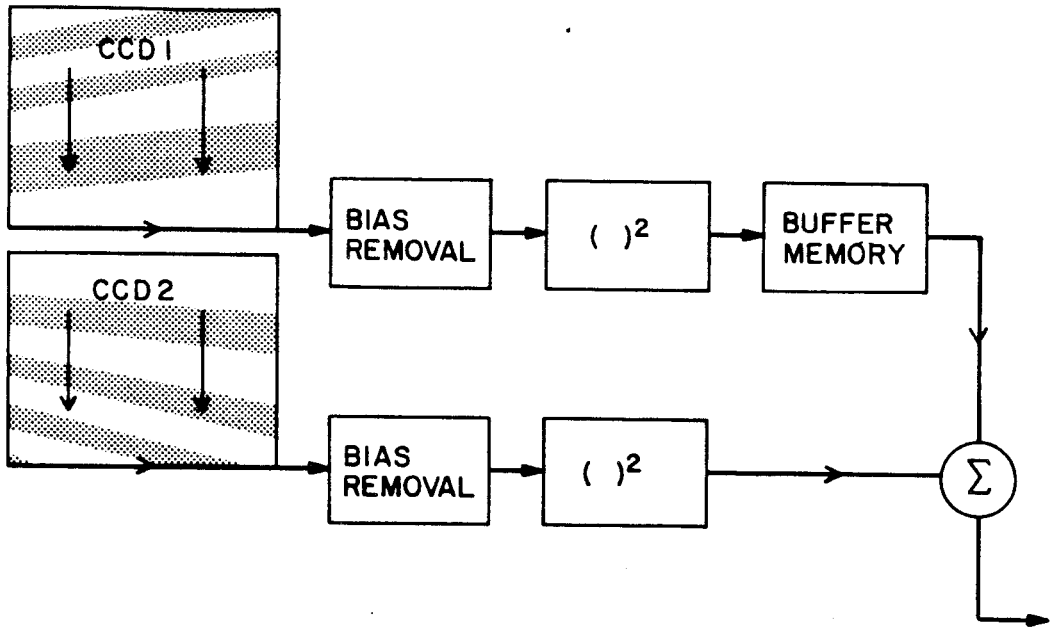

Figure 6.11. Schematic diagram of output plane and post-processing in a 2-look imager.

output synchronously with the output of the second CCD. The delay due to the buffer memory is programmed such that the summed images have the correct registration. If the buffer memory is a circulating or scrolling memory, then the 2-look image can be continuously scrolled out to form a strip-map as in the basic processor.

6.4 Application to Spot-light mode SAR

6.4.1 Description of Architecture

In spot-light mode SAR the antenna beam pattern is typically steered to illuminate the same ground patch throughout the data collection period. The maximum azimuthal extent of the image is determined, therefore, by

the width of the beam. The goal is to form a high resolution image of a specific region of the scene rather than a long strip-map. Since the antenna beam is steered, the azimuth integration time is not limited to the width of the footprint divided by the radar's velocity, as in strip-map SAR. Since the radar can be made to illuminate the scene for an arbitrary time period, azimuth resolutions better than that given by Eq. 2.2 are theoretically achievable.

The implementation of the programmable multiplicative architecture for spot-light mode SAR is as follows. Since the images are generated in a framed format, a staring mode CCD is employed. In this mode the CCD integrates during imaging without shifting the accumulating charge. The azimuth correlation is achieved by shifting the azimuth filter incrementally in the AOD during the integration period. The azimuth integration window is therefore not limited by the aperture of the CCD. Instead, the integration period is determined by the total length of the azimuth reference function as it shifts through the AOD. This length is not limited by the size of any of the optical elements.

Performing the azimuth compression in this manner offers several advantages not available in the strip-map processor. Since the azimuth processing window is not limited by the size of the transducers, higher resolution is

achievable. Secondly, operating the CCD in the staring mode permits the image to be periodically read-out to remove the bias, and then coherently summed off of the CCD in electronic memory. With this technique, higher dynamic range than that afforded by the CCD is possible. Lastly, incoherent summation of images in electronic memory can be implemented in a manner similar to the coherent summation to achieve multiple looks.

In general, the spotlight mode SAR will operate at average squint angles other than 90°; so that compensation for the gross doppler frequency is necessary as described in Chap. 5. The range walk delays are compensated by electronically delaying the successive laser diode trigger pulses by $\bar{t}$, as described in Section 5.4. The required interferometrically generated azimuth function is then of the same form as Eq. 5.16, and the axes of the focused image on the CCD are aligned with the range and azimuth axes of the radar geometry at $t = 0$.

If range curvature can be neglected, then the operation of the spot-light mode processor is functionally identical to that of the framed mode forward-looking processor described in Section 5.4. This is true because shifting the azimuth filter with respect to fixed charge pattern on the CCD is mathematically equivalent to shifting the charge with respect to the fixed azimuth filter. The actual implementation of the azimuth compression, however, requires

more sophistication. When compensating for the range/azimuth coupling there are two effects to be considered in the spot-light mode version of the processor. The first is scaling of the azimuth coordinate by the range/azimuth coupling parameter, as characterized in Section 6.3.2. This can be corrected, if needed, by tilting a lens as described in Section 6.1. The second effect to be considered is the scaling of the chirp rate of the azimuth phase history of scatterers by the range/azimuth coupling parameter. In the strip-map processor, the tilted lens corrected for this because the shift rate on the CCD was the same at all range bins. In the spot-light mode processor, however, the tilted lens magnifies the shift rate of the azimuth filter by the range/azimuth coupling parameter for each range bin so that the filter chirp rate, as seen by any point on the CCD, is identical. To correct for this we must employ the electronic range/azimuth coupling compensation technique described in Section 6.3.2, whether or not the tilted lens is used.

If the azimuth integration period is long enough, then range curvature becomes non-negligible and must be counteracted to produce a high quality image. Here we propose a technique to do this in which the CCD is rotated through a small angle, at a constant rate, during the integration period.

We parameterize the radar geometry as in Chap. 5. The

position of an arbitrary point scatterer is specified by its range and azimuth coordinates (ρ,γ) with respect to the center of the field located at (R_o,θ_o) at t = 0. The chirp rate b (cm^{-2}) is defined to describe the azimuth filter at the CCD plane in this processor, for the range bin corresponding to $\rho = 0$. The center of the CCD corresponds to the center of the ground patch being imaged. We assume that the tilted lens technique for range/azimuth scaling compensation is used. The azimuthal location, y, of a focused point scatterer on the CCD is found by equating the phase of the scatterer with respect to the center of the ground patch with its phase with respect to the center of the CCD. It follows that:

$$y = \gamma(\omega_o R_o/\pi cb)^{1/2}. \tag{6.17}$$

The corresponding range coordinate of an arbitrary scatterer on the CCD is:

$$x = \rho(2Mv_a/c). \tag{6.18}$$

Neglecting the constant delay term, the time delay of the echo from a scatterer at (ρ,γ), for the nth return is, (see Eq. 5.4):

$$\Delta t(\rho,\gamma,n) = 2\rho/c - 2vnT\cos(\theta_o + \gamma)/c - (vnT\sin(\theta_o + \gamma))^2/R_o c$$

$$\sim 2\rho/c - 2vnT\cos(\theta_o)/c + (vnT\sin\theta_o)^2/2R_o c + 2vnT\sin(\theta_o)\gamma/c. \tag{6.19}$$

The first term is the normal fixed delay corresponding to the range bin of the scatterer. The second term is the range walk delay that is compensated electronically. The third term corresponds to the portion of the range curvature component that is common to all scatterers in the field. This term can also be compensated electronically and we assume that this is so in this technique. The resulting net delay in the processed received signal is:

$$\Delta t' = 2\rho/c + 2vnT\gamma\sin\theta_o/c. \qquad (6.20)$$

Since the linear component (in n) of the range curvature delay is proportional to the angular position, then the actual position of the range focused signals at the CCD plane, given by $\Delta t' M v_a$, is modified by the range curvature from that given by Eq. 6.18 to:

$$x = \rho(2Mv_a/c) + \gamma(2Mv_a vnT\sin\theta_o/c). \qquad (6.21)$$

Since it is proportional to γ, the second term in Eq. 6.21 can be cancelled by rotating the CCD at a constant rate. The rotation rate of the CCD must be such that the incremental movement for one pulse period, Δx, is compensated. From Eq. 6.21, Δx is given by:

$$\Delta x = \gamma(2Mv_a vT\sin\theta_o/c). \qquad (6.22)$$

The required CCD rotation rate is thus:

$$\omega \sim \Delta x/yT = 2Mv_a v(\pi b/c\omega_o R_o)^{1/2}\sin\theta_o. \qquad (6.23)$$

As a consequence of this range curvature correction technique, the apparent shift rate of the azimuth filter varies as a function of the range coordinate on the CCD. The change in the shift rate of the azimuth filter in the AOD is:

$$\Delta\dot{y} = \omega x = \rho((2Mv_a)^2 v/c)(\pi b/c\omega_o R_o)^{1/2}\sin\theta_o. \qquad (6.24)$$

This shift rate difference is compensated by choosing the appropriate chirp rate in the electronic range/azimuth coupling signal $\phi_r(n)$. Assuming the azimuth reference function is imaged 1:1 on the CCD at the range bin x =0, then the shift rate of the azimuth filter in the AOD is:

$$\dot{y} = v(\omega_o/cR_o\pi b)^{1/2}\ \sin(\theta_o). \qquad (6.25)$$

If:

$$\Delta\dot{y}/\dot{y} = \rho/R_o, \qquad (6.26)$$

then the induced shift rate difference matches that due to the range/azimuth coupling. In this case no electronic range/azimuth coupling compensation is required. For Eq. 6.26 to be satisfied the following relationship beyween the parameters b and M in the processor is required:

$$b = M^{-2}c\omega_o/4\pi v_a^2 R_o. \qquad (6.27)$$

If this condition is satisfied, then the scaling of the axes

on the CCD matches that of the ground coordinates, i.e.,:

$$x/y = \rho/\gamma R_o. \tag{6.28}$$

Furthermore, in this case, the rotation rate of the CCD reduces to:

$$\omega = v\sin\theta_o/R_o, \tag{6.29}$$

which is equal to the rate at which the angle of the radar is changed to keep the beam centered on the scene being imaged.

6.4.2 Experiment

The application of the crossed AOD architecture to spot-light mode SAR was validated in an experimental demonstration of the azimuth compression technique in which the reference is shifted in the AOD. The CCD detector was operated in the standard video mode at a frame rate of 30 Hz. The azimuth integration period was also set at 1/30 second to match the CCD frame rate. A simulated target with a TBWP of 80 was used, as in the previously described architectures. Consequently, the phase history of the simulated radar returns was identical to that shown in Fig. 6.8, with the time scale compressed by a factor of 30.

The LFM filter signal was shifted incrementally in the AOD, during the integration period, by means of a programmable delay generator. To observe the shifting of the azimuth filter the sinusoidal reference signal in the

AOD containing the simulated radar signal was removed. This corresponds to setting A = 0 in Eq. 6.11. In this mode the simulated range focused signal is an image of the azimuth filter along the y direction. Fig. 6.12 shows the output of the CCD (as displayed on a video monitor), for various values of n, as the reference function is shifted in the AOD. The shift rate was programmed such that a LFM signal with a TBWP of 80 passed any portion of the CCD during the 1/30 second integration period. Fig. 6.12c depicts the reference function's position at the midway point of the integration period; and shows that the SBWP of the displayed azimuth reference function is approximately 25.

Azimuth compression of the simulated radar signal is achieved by reinstating the sinusoidal reference signal that had been removed to show the reference function. The result is shown in Fig. 6.13. The bias ridge is seen and the high resolution image of the point scatterer appears as a narrow slit in the middle of the ridge. Since bias removal was not utilized in this demonstration, the phase of the simulated echoes was adjusted to maximize the negative peak of the focused spot for display purposes. This corresponds to setting $\mu_o = \pi$ in Eq. 5.5. The narrowness of the peak proves that the SBWP of the CCD did not limit the azimuth resolution.

To display these signals in perspective, the CCD was rotated 90° so that the range focused line fell on a row of

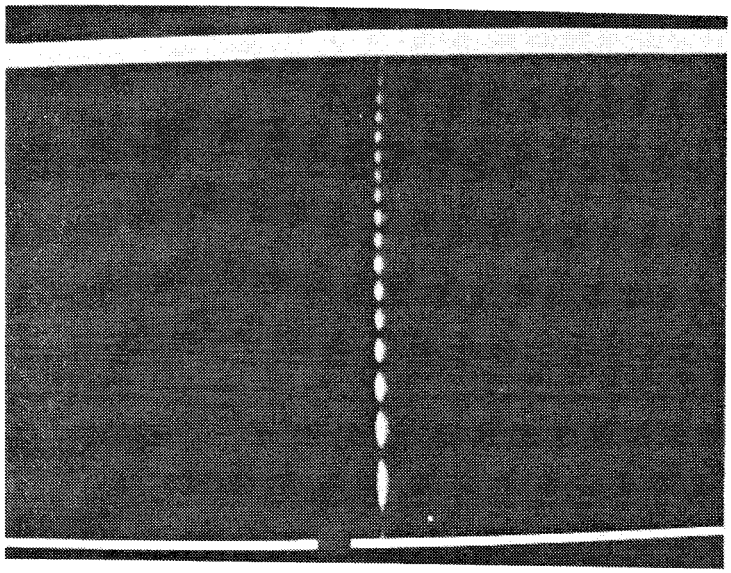

(a)

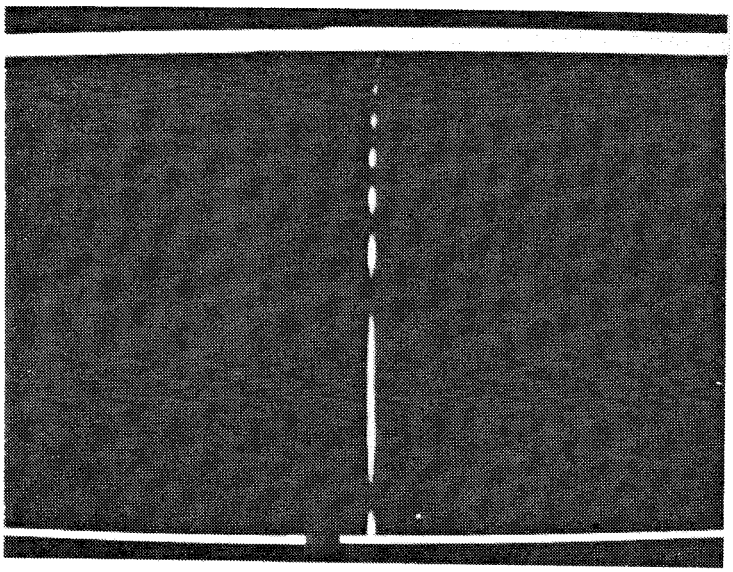

(b)

Figure 6.12. Image of azimuth filter shifting in the AOD.

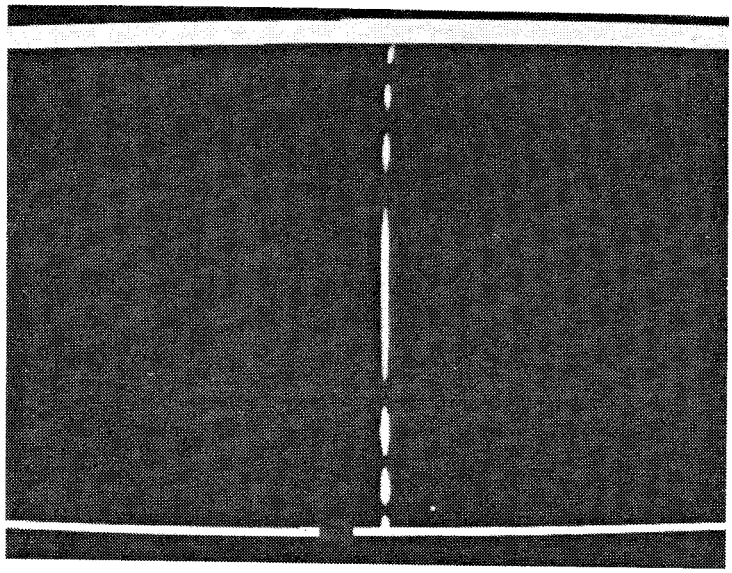

(c)

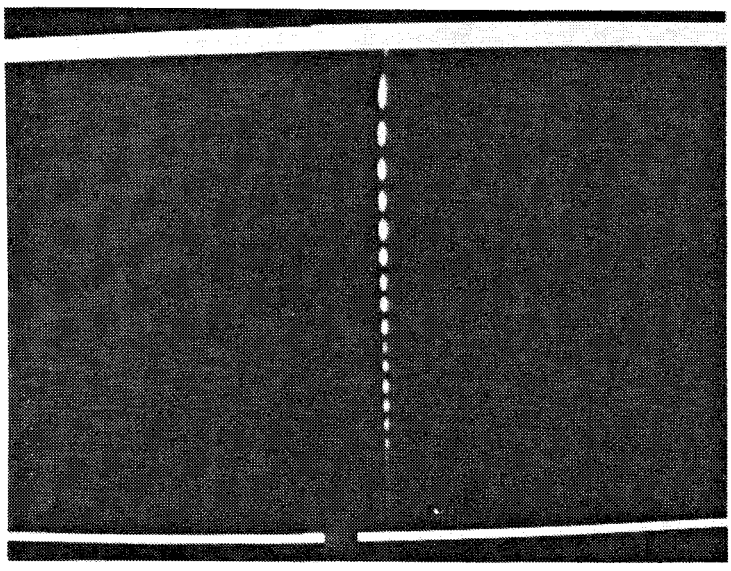

(d)

Figure 6.12. (continued).

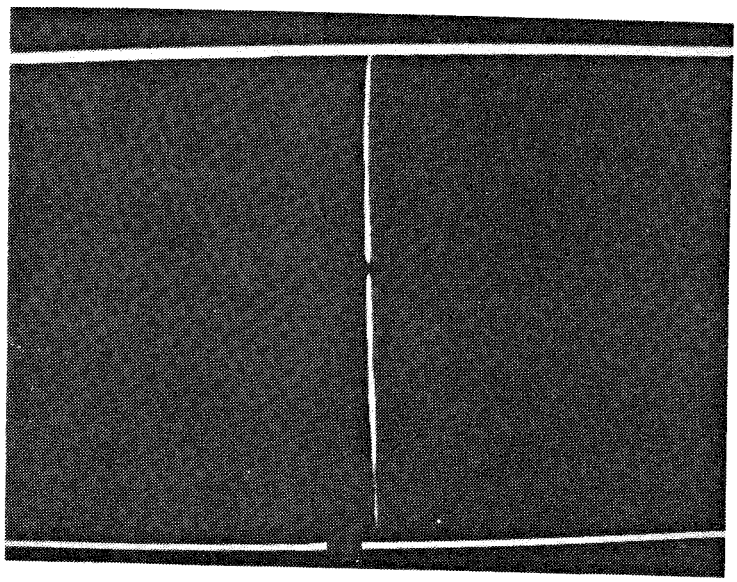

Figure 6.13. Azimuth pulse compression in spot-light mode implementation.

pixels sensed in the same video line. Fig. 6.14 shows two oscilloscope traces of single lines of the CCD video output for the shifted azimuth filter. These data correspond to images shown in Figs. 612b and 6.12c respectively. More lobes of the reference signal are displayed because the CCD, which is rectangular in shape, is longer along this dimension. These traces show the integrated apodizing effects of the processor. When the reference signal was reintroduced, the azimuth compression shown in Fig. 6.15 resulted. Both negative and positive peaks are shown, coresponding to setting the relative phase of the radar signals (with respect to the azimuth filter) to π and 0

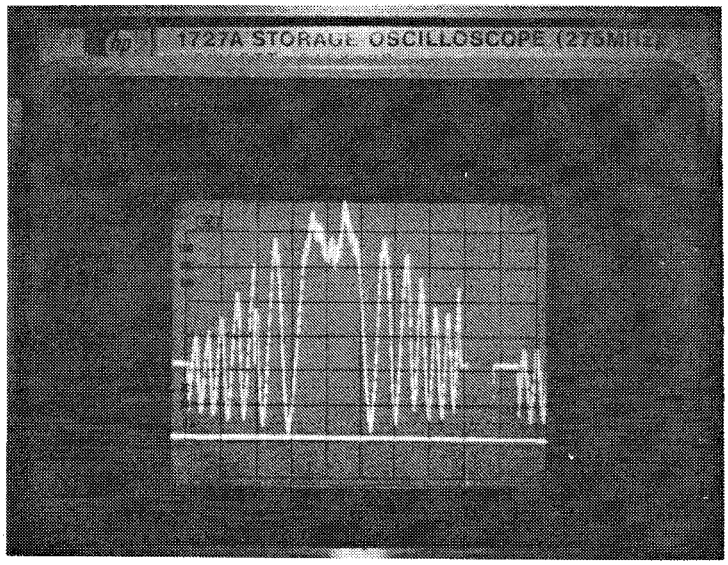

(a)

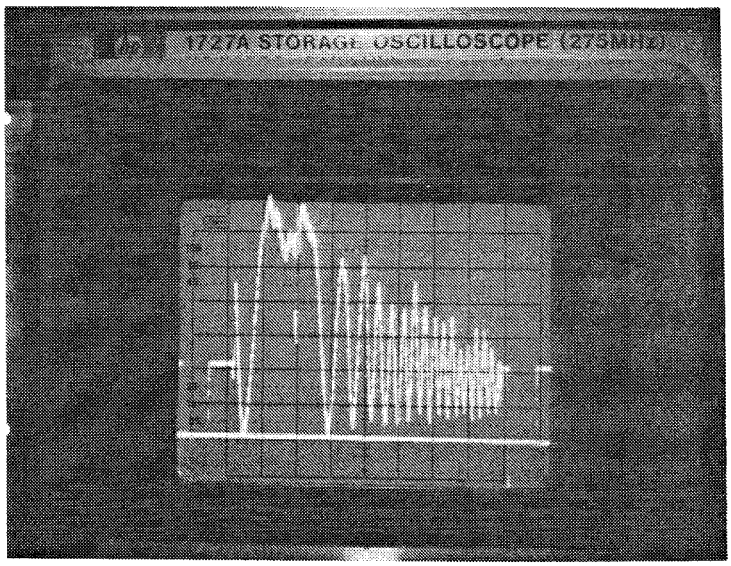

(b)

Figure 6.14. Video signals showing response of CCD to image of azimuth reference filter.

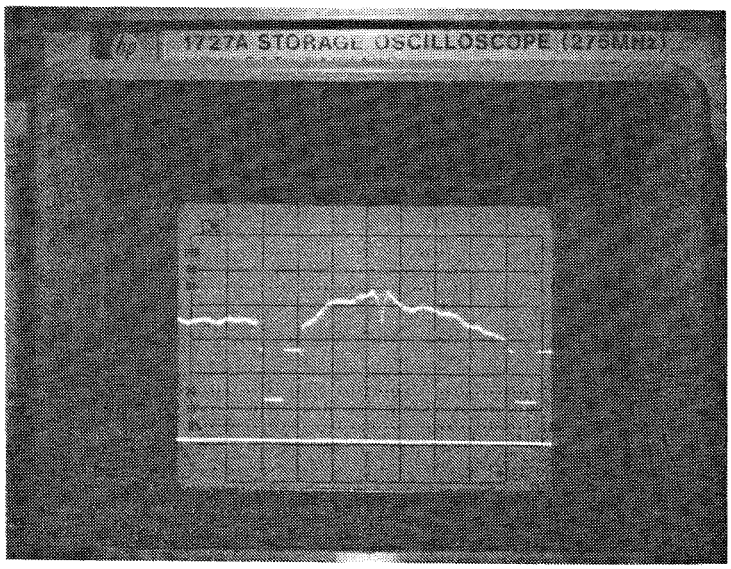

(a) $\mu_0 = \pi$.

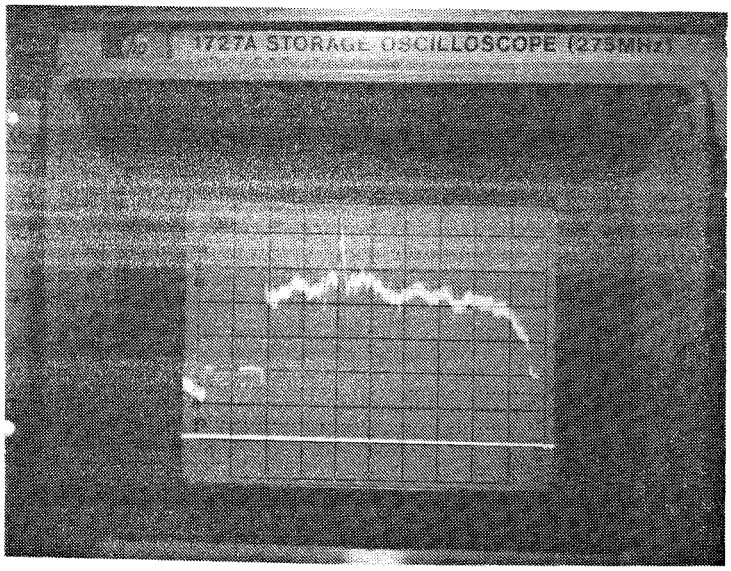

(b) $\mu_0 = 0$.

Figure 6.15. Video signals showing azimuth compression of simulated spot-light mode SAR signals.

respectively. The pulse widths achieved are consistent with those of the strip-map versions of the processor for the same azimuth TBWPs.

CHAPTER VII. CONCLUSIONS

7.1 Summary

In this thesis we have presented a new and radically different approach to optical SAR processing in which real-time operation is accomplished by using dynamic transducers instead of photographic film. The TSI architecture was defined in terms of a decomposition of the 2-D SAR problem into a cascade of 2 1-D integrations, thereby making possible the use of a 1-D SLM as the input electronic-to-light transducer. The successful application of the TSI approach to SAR was shown to be due to the complementary nature of the spatial and temporal integrations, and their respective match to the range and azimuth data rates.

The key result in the experimental verification of the TSI architecture was the successful coupling of the range and azimuth integrations with a common path interferometric technique. Pulsed laser diodes were shown to have sufficient coherence length to achieve good fringe depth in the processor. The impulse response of the processor was measured with electronic signals that simulated the echoes from a point scatterer in the target field.

An important performance issue concerned the removal of the interferometric bias artifacts which corrupt the image. An optical carrier encoding/demodulation scheme was

demonstrated that efficiently removed the fixed pattern noise as well as the bias components. The dynamic range of the processor was derived in terms of the intrinsic dynamic range and MTF of the CCD, fringe visibility of the processor, and statistical parameters of the point scatterers that make up the imaged scene. It was shown that, although the dynamic range is reduced as the number of scatterers within a range bin increases, the degradation increases only as the square root of the number of scatterers.

The processor was generalized to compensate for range migration effects in the SAR geometry. Range walk, associated with squint-mode SARs, was added to the simulated radar signals and compensated by the processor. The processing architecture was further generalized by making it programmable. This was accomplished by replacing the fixed azimuth reference mask with an AOD in which the appropriate reference function is loaded electronically. The application of the programmable architecture to both strip-map and spotlight mode SAR was experimentally verified. Some of the capabilities and limitations of the TSI architecture, for various SAR applications, are summarized in Table 7.1.

7.2 Future Directions

Our research has established the validity of the TSI approach for SAR imaging. Therefore, when the TSI

Table 7.1. Applicability of the AO/CCD architecture

Type of SAR	Programmable Azimuth Filter	Range Curvature Correction	Range Walk Compensation
Side-looking Strip-Map	yes	yes	n/a
Squint-mode Strip-Map	no	no	yes
Side-looking Spot-light	yes	yes	n/a
Squint-mode Spot-light	yes	yes	yes

architecture is applied to specific SAR problems, the work will consist mainly of engineering to determine the best practical configuration of the architecture. The processor design work will necessarily include optical, mechanical, and electronic trade-offs. The choice of components will be driven by the details of the SAR scenario. For example, a spaceborne SAR may require a relatively longer total range delay window and lower resolution, indicating that a long time aperture AOD should be used, whereas an airborne SAR may require a shorter range delay window and higher resolution, indicating that a high bandwidth AOD should be used.

The compactness and low power requirements of the

AO/CCD processor create new possible applications for real-time SAR that may have been previously impractical. One possible new application is for a mapper on board a Venus orbiter. The imager would comprise only a small portion of the instrumentation. Furthermore, the bandwidth compression achieved by onboard processing of the SAR images would reduce the size and sophistication of the telemetry.

The application of the AO/CCD architecture to Inverse SAR (ISAR) is one area of possible future research. In ISAR the radar is typically stationary, while the imaged object is moving. Fundamentally, the ISAR problem is identical to that of SAR: the azimuthal velocity component between the radar and object creates a synthetic aperture that is used to achieve high angular resolution. ISARs have been used to image Venus, from its rotation, flying aircraft, from their motion relative to a fixed radar, and ships, from their pitch and roll motions. In general, the ISAR problem is more difficult than the SAR problem because the relative velocity vector is not always known a priori. Furthermore, the relative velocity component may change dynamically during the integration period. The radar processor must therefore estimate the gross relative motion and compensate for it. A version of the programmable TSI architecture may have application here.

Variations of the AO/CCD processor may have application to inverse scattering problems other than radar imaging.

Possible areas of future research for a real-time TSI architecture include: the generation of images from tomographically collected data in medicine, the processing of sonar data, and the investigation of subterranean features from reflected sound waves.

REFERENCES

1. Cutrona, L., Vivian, W., Leith, E., and Hall, G., "A High Resolution Radar Combat-Surveillance System," IRE Transactions on Military Electronics, Vol. MIL-5, No.2, pp. 127-131, April 1961.

2. Sherwin, C., Ruina, J., and Rawcliffe, D., "Some Early Developments in Synthetic Aperture Radar Systems," IRE Transactions on Military Electronics, Vol. MIL-6, No. 2, pp.111-115, April 1962.

3. Skolnik, M. I., "A Perspective of SAR for Remote Imaging," Naval Research Laboratory Memorandum Report, May 1978, Washington D. C..

4. Dicke, R. H., "Object Detection," U. S. Patent No. 2624876, January 6, 1953.

5. Cutrona, L. and Hall, G., "A Comparison of Techniques for Achieving Fine Azimuth Resolution," IRE Transactions on Military Electronics, Vol. MIL-6, No. 2, pp.119-121, April 1962.

6. Psaltis, D., "Two-Dimensional Optical Processing Using One-Dimensional Input Devices," Proceedings of the IEEE, Vol. 72, No. 7, pp. 962-974, July 1984.

7. Bader, T., "Acousto-optic Spectrum Analysis: A High Performance Hybrid Technique," Appl. Opt., vol 18, p.1668, 1979.

8. Psaltis, D., and Casasent, D., "Time-and-space Integrating Spectrum Analyzer," Appl. Opt., vol 18, p. 3203, 1979.

9. Psaltis, D., and Wagner, K., "Real-time Optical SAR Processor," Opt. Eng., vol. 21, p.822, 1982.

10. Psaltis, D., Haney, M., and Wagner, K., "Real-time Synthetic Aperture Radar Processing," in Proc. NASA Conf. on "Optical Information Processing," (Hampton, VA, 1983).

11. Psaltis, D., "Optical Image Correlation Using Acousto-optic and Charge Coupled Devices," Appl. Opt., vol. 21, p. 491, 1982.

12. Brillouin, L., "Diffusion de la lumière et des rayons X par un corps transparent homogène," Ann. Phys. (Paris), vol. 17, pp. 88-122, 1922.

13. Whitman, R., Korpel, A., and Lotsoff, S., "Application of Acoustic Bragg Diffraction to Optical Processing Techniques," in Proc. Symp. Modern Optics, pp. 243-255, 1967.

14. Chang, I. C., and Hecht, D. L., "Characteristics of Acousto-optic Devices for Signal Processing," Opt. Eng., vol. 21, no. 1., 1982.

15. K. Wagner and D. Psaltis, private correspondence

16. Y. A. Bykovskii, et al., "Method for Investgating Thermal Condition in and Spectral Characteristics of a Semiconductor Laser by means of a Fabry-Perot Resonator," Soviet Physics-Semiconductors, Vol. 5, No. 3, September 1971.

17. J. Butler, "The Effect of Junction Heating on Laser Linearity and Harmonic Distortion," Topics in Applied Physics, Vol. 34, Chap. 8, Springer Verlag, Berlin, 1980.

18. Y. A. Bykovskii, et al., "Coherence of the Radiation of a Pulsed Single Mode Injection Semiconductor Laser," Soviet Physics- Doklady, Vol. 17, No. 4, October 1972, p. 359.

19. P. Melman, W. Calsen, "Interferometric Measurement of Thermal Coherence and Time-varying Longitudinal-Mode Wavelengths in GaAs Diode Lasers," CLEO'81, June 1981, p. 72.

20. M. Haney, D. Psaltis, "Coherence Properties of Pulsed Laser Diodes,"10th International Optical Computing Conference, SPIE Vol. 422, p.197, 1983.

21. Hitachi Laser Diode Application Manual

22. K. Y. Lau, C. Harder, A. Yariv, "Longitudinal Mode Spectrum of Semiconductor Lasers Under High-speed Modulation," IEEE Journal of Quantum Electronics, Vol. QE-20, No. 1, January 1984.